THE UNVERSITY OF HULL

Laboratory Scale Experiments with Water Surface Waves

being a Thesis submitted for the Degree of

Doctor of Philosophy, Department of Engineering

in the University of Hull

by

Robert J A Bedard, BEng (University of Hull)

July 2013

Abstract

The thesis presents the development, implementation and results of two series of experiments, at large and small scale, for the study of surface gravity waves. A number of measurement techniques are developed and implemented to capture space and time evolution of waves on a water surface in gravity, gravity-capillary and capillary ranges with the purpose to study the statistics of wave turbulence in terms of frequency and wave number spectra.

The first series of experiments was conducted in a large wave tank of size 12 m x 6 m x 1.6 m filled with water to a depth of 0.9 m. A wave maker comprised of eight panels is controlled by a computer to generate waves at typically two frequencies; these waves are directed at different angles. Surface elevation of the resulting turbulent wave field is measured via capacitance wire probes and a fluorescent laser technique that is capable of capturing wave profiles at sufficient frame rate to access both wavenumber and frequency statistics. Following the processing of these data a comprehensive set of results describe characteristics of the life cycle of the experiment including the rise of the wave field to its statistically stationary state and the decay of the regime after energy pumped into the system from the wave maker has ceased.

The second series of experiments are conducted with a tank of size 0.42 m x 0.42 m x 0.25 m vibrating vertically on an electromagnetic shaker in order to generate parametric waves on the surface. One of the key observations in these experiments is of a low frequency wave that is generated through high frequency vertical oscillation of the tank, three possible explanations for this phenomenon are considered including; an inverse cascade of waves, jet instability and low frequency spatial resonance. Results of the measurement of surface gradient via a laser refraction technique and of 2-d surface elevation via Fourier transform profilometry are presented to characterise the chaotic wave fields. The presented results are in a qualitative agreement with the spatial resonance theory or could possibly be described by the inverse cascade. A conclusive statement about the mechanism for the generation of a low frequency wave in this kind of system cannot yet be made; a number of questions relating to future investigations are raised.

Across both series of experiments the implementation of data acquisition techniques forms a significant contribution to the work undertaken and a comprehensive set of tools for measurement and analysis of data from surface waves is developed.

Acknowledgements

Thanks to my supervisor Dr. Sergei Lukaschuk for his advice, guidance and knowledge.

Thanks also to the technical staff, Brendon Murphy at the Deep, John Hebden and the staff in the mechanical workshop and Steve Coopland in the electronics workshop. All of whom have provided excellent support and advice.

Contents

1 Introduction

Water waves are among one of the most mesmerising sights to behold, to stand on a beach or pier and stare out to sea has a strange satisfaction, waves can be peaceful and relaxing or fearsome and powerful, by their nature they invoke emotion. This simple attraction holds true in the pursuit of understanding the systems of waves and unsurprisingly on a planet whose surface is covered in the majority by water, the understanding and modelling of waves is of great importance to a vast array of human and natural activity; for example, navigation (Lewis, 1978) for power generation (Yemm, Pizer, Retzler, & Henderson, 2012) and coastal erosion (Lim, Rosser, Petley, & Keen, 2011) among others.

Direct measurement of surface waves on the ocean is possible through a variety of techniques such as; wave buoys, which can be used to monitor surface elevation (Mitsuyasu, et al., 1979) and wave direction (Steele, Teng, & Wang, 1992). Airborne measurements using Lidar can be used to measure spatial data (Hwang & Wang, 2000) and satellites utilising radar are used for wave elevation and directional measurements (Krogstad & Barstow, 1999).

These measurements of the ocean are part of a complex system that contains many uncontrollable parameters. Laboratory based models and simulations address this issue because they offer control over many of these same parameters, the advantage of this is twofold. In the first instance they can be compared with wave turbulence theory more carefully than the 'real' measurements and in the second instance they can be compared with measurements from the ocean. Experiments are a necessary bridge between the real world and theoretical ideas, for example wave breaks can be generated in an experiment but are difficult to describe by theory or model numerically.

The thesis is comprised of two sections, in the front section (chapters 2 and 3) important theoretical concepts are introduced to provide a background to the topic of wave turbulence. This is followed by an introduction to experimental techniques and a discussion on the development of measurement devices and their implementation in various experiments. The experiments are discussed in terms of how they compare with theoretical expectations and the limitations of the techniques.

In section two of the thesis (chapters 4 to 7), the development of purpose built measurement devices for implementation in a series of experiments are introduced these range from point like measurements to 2-d surface reconstruction. The first series of experiments focuses exclusively on gravity wave turbulence and they are rather unique in that very few experiments have been conducted on this scale for turbulent wave regimes. The second series of experiments are conducted in a smaller scale tank and cover a broad range of waves, from gravity through to capillary waves. In the final chapter, the results from all the presented experiments are brought together and suggestions for the future direction of similar experiments are made.

2 Theoretical Approach to Wave Turbulence

In this chapter an introduction to surface waves is established and some of the most notable theories for the description of wave turbulence are presented, including a number of testable predictions that are applicable to the experiments discussed later in the thesis.

2.0 Types of surface waves

Surface waves are generated at the interface between two media, for example water and air, displacement of the water surface is caused by a force such as the wind over the ocean. Surface waves fall into two general categories, gravity waves and capillary waves with a possible third category of gravity-capillary waves. Gravity waves take their name from the restoring force of gravity; after the surface has been displaced gravity attempts to restore the surface back to its equilibrium position resulting in an oscillation.

Shorter waves are less susceptible to the force of gravity and their principal restoring force is that of surface tension, these waves are known as capillary waves. There is of course some cross over where gravity and surface tension are both significant contributors to the surface restoration and hence the third category of gravity-capillary waves. To describe these waves further the linear dispersion relation is considered.

2.0.1 Linear Dispersion Relation

The linear dispersion relation describes the interrelation between frequency and wavenumber, for a given wavelength there is a certain frequency. This relationship is derived from the Navier Stokes equations for fluid motion with certain assumptions, idealisations and the application of boundary conditions. In the first instance the flow is assumed to be incompressible so that density is constant and then flow is assumed to be inviscid leading to Euler equation of motion,

$$\frac{D\boldsymbol{q}}{Dt} = -\frac{1}{\rho}\nabla p + g$$

Where,

q is fluid velocity, t is time, ρ is density,

p is pressure g is the force due to gravity.

Furthermore it is assumed that the flow is also irrotational, this means the fluid particles do not rotate.

Application of boundary conditions is the next step, the interface between water and air represents the surface on which the waves are considered, imagine that for some area on that surface the same particles stay on the surface and do not leave the given area; this describes the first boundary condition and is necessary to preserve continuity. The second boundary condition is that pressure above the surface is a constant, this comes from the assumption that there is no motion in the air above the interface, for practical purposes the pressure can be taken as zero, this means that the only forces in the final equation will be due to gravity and surface tension, both of which are constant for an individual case although the surface tension of a liquid will change with temperature.

The boundary conditions described here are non-linear and so the amplitudes of the waves are considered to be of very small amplitude thereby reducing the problem to a linear one since the non-linear terms also become very small. The derivation of the linear dispersion relation can be found in many textbooks for example see (Crapper, 1984) or (Lighthill, 1978) but it is expressed in its final form here; the full linear dispersion relation for both gravity and capillary waves is given as,

$$\omega^2 = \left(gk + \frac{\sigma}{\rho}k^3\right)\tanh(kh) \qquad \textbf{2.1}$$

where,

ω is wave angular frequency, g is acceleration due to gravity,
k is $^{2\pi}/_{\lambda}$, where λ is wavelength, σ is surface tension,
ρ is density, h is the liquid depth.

This notation will be used throughout this thesis. The dispersion relation can be split into three key parts, 1) gk takes into account the restoring force of gravity, 2) $^{\sigma}/_{\rho}k^3$ takes

into account the effect of surface tension and 3) tanh(kh) accounts for the depth of fluid and the effect of friction from the bottom of the container: Waves can be considered to exist on deep water when tanh(kh) is close to 1. If $kh = pi$ then tanh(kh) = 0.996 and so when $h > 0.5\lambda$ the effect of fluid depth is negligible.

The dispersion relation is shown for surface waves on deep water in Figure 2.1, the axes are converted from wavenumber and angular frequency to wavelength (m) and frequency (Hz) the gravity and capillary ranges can be clearly seen and are labelled as such. The cross over between the two occurs when the effect of gravity as a restoring force is the same as the surface tension effect. The crossover can be found approximately by taking $gk = \frac{\sigma}{\rho}k^3$, this yields a wavelength of approximately 15 mm or frequency 10 Hz for surface waves on deep water.

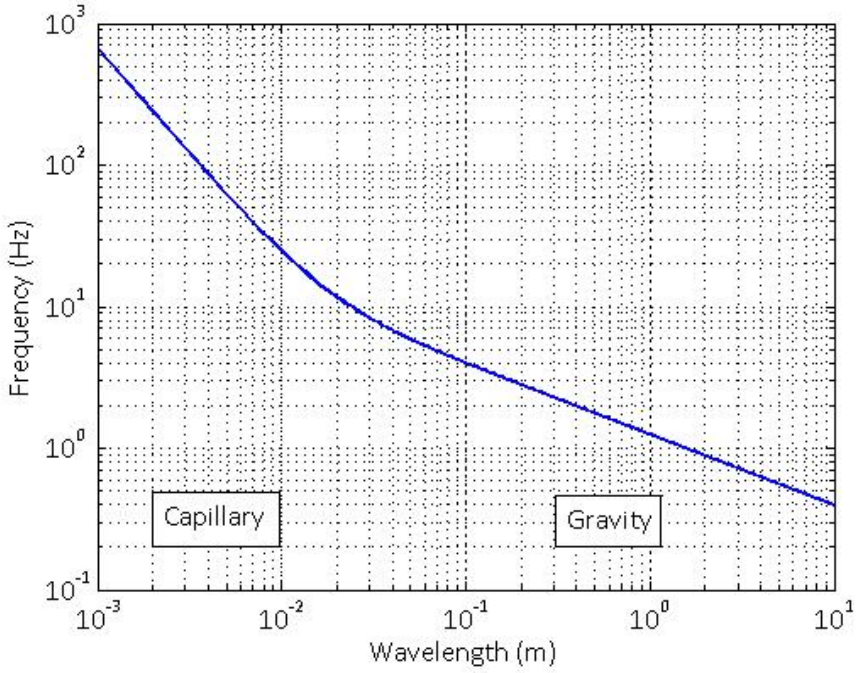

Figure 2.1 – Dispersion relation for surface waves on deep water from Equation 2.1

2.1 Wave Interactions

In order to characterise wave interactions a Hamiltonian expansion of the equation of motion is written (Zakharov, L'vov, & Falkovich, Kolmogorov Spectra of Turbulence, 1992). Waves on different surfaces are only distinguished by the dispersion relation presented in the previous section. Here the description presented is purely for

understanding of the physical properties rather than presenting numerous equations. Consider,

$$H = H_2 + H_N$$

Where H is the Hamiltonian, the term H_2 is a linear term that describes the energy of all the waves in the system and H_N is a series of non-linear terms where N is the number of waves involved in an interaction.

Since a single wave on its own cannot change and two waves that interact if they are to conserve energy must produce a third then the lowest order for wave interactions is the three wave interaction or resonant triad, H_3 leads to $\mathbf{k_1} + \mathbf{k_2} + \mathbf{k_3} = 0$ and $\omega_1 + \omega_2 + \omega_3 = 0$. These wave interactions will exist when these equations are satisfied by the linear dispersion relation ω(k). If the dispersion relation does not allow for these interactions then the four wave interaction or resonant quartets can still occur, $\mathbf{k_1} + \mathbf{k_2} = \mathbf{k_3} + \mathbf{k_4}$ and $\omega_1 + \omega_2 = \omega_3 + \omega_4$, this equation can always be satisfied but a wave field can be thought of as always defaulting to the lowest order of interactions, this is due to each term in the expansion becoming much smaller as the value of N increases, so for example 5 wave processes are possible but are negligible by comparison to the 4 wave process. In practice this means that the gravity waves are dominated by the four wave process and the capillary range by the three wave process.

2.2 Wave Energy Spectrum

In order to characterise water wave turbulence a quantity needs to be measured for understanding and comparison, naturally for experimentalists measuring the surface elevation is the first priority, although it is not the only quantity that can be measured, but what to do with this data? In wave turbulence, as in other statistical theories, a useful description is the wave power spectrum or power spectrum; this is produced in both the frequency (ω) and the wavenumber (k) domains. These spectra are defined as,

$$E_\omega = \int e^{i\omega t'} < \eta(\boldsymbol{X}, t)\, \eta(\boldsymbol{X}, t + t') > dt' \qquad \textbf{2.2}$$

for the frequency domain and for the wavenumber domain in one-dimensional space as,

$$E_k = \int e^{ikz} < \eta(\boldsymbol{X}, t)\, \eta(\boldsymbol{X} + \boldsymbol{W}z, t) > dz$$

2.3

Where: $\eta(X,t)$ is the surface elevation at a time t and location in space $\boldsymbol{X}(x,y)$ which lies on a horizontal plane. These spectra are a useful tool to compare different turbulent wave fields since the measured quantity from the surface will have a chaotic signal.

The energy spectra in both domains are predicted to exist as power laws when the wave regime is statistically steady and the wave vectors are isotropic E_k and E_ω are independent of t and $\boldsymbol{X}$,

$$E_\omega \propto \omega^{-v}$$

2.4

and

$$E_k \propto k^{-\mu}$$

2.5

The indices are the slope that can be found from spectral plots and can be compared to theories and as such v and μ have different values these will be introduced in the following section 2.3 Power Spectrum Predictions for Gravity Waves.

2.3 Power Spectrum Predictions for Gravity Waves

2.3.1 Hasselmann Equation

The energy cascade of water waves is governed by the kinetic equation for waves, Hasselmann (1962) derived a lengthy but very specific equation often referred to as the Hasselmann equation or simply the energy balance equation. This equation has an exact power law solution known as the Zakharov-Filonenko spectrum.

2.3.2 Zakharov-Filonenko Theory

For waves in a statistically steady state that follow a direct cascade of energy (Zakharov & Filonenko, 1967), Zakharov, L'vov, & Falkovich (1992) produced the prediction;

$$E_\omega \propto \omega^{-4}$$

2.6

the corresponding k spectrum prediction is

$$E_k \propto k^{-\frac{5}{2}}$$

2.7

2.3.3 Phillips Model

Phillips (1958) produced a model based on forcing from a turbulent wind where wave breaks are the main source of dissipation, breaks in this sense describe a break in the surface slope caused by sharp crested waves. In the theory the breaks are considered to be point like, dimensional analysis leads to,

$$E_\omega \propto g^2 \omega^{-5}$$

2.8

And following the linear dispersion relation,

$$E_k \propto k^{-3}$$

2.9

2.3.4 Kuznetsov Model

Rather than the point like breaks in Phillips prediction, Kuznetsov (2004) considered breaks along a line, when the crest of the wave is considered to have its shape preserved leading to $\omega \propto k$. The assumptions yield,

$$E_\omega \propto \omega^{-4}$$

2.10

And since $\omega \propto k$ in this case

$$E_k \propto k^{-4}$$

2.11

It is immediately apparent that this is the same index as the Zakharov-Filonenko prediction but the physics behind this result is very different.

2.3.5 Finite Boundaries Wave Excitation Prediction

Weak wave turbulence relies on having waves interacting in an infinite basin, in general the infinite box limit cannot be met and so research has been conducted to deal with a finite boundary condition. Much of this research has been conducted in the last ten to

fifteen years and is of clear importance because finite boundaries offer more testable predictions particularly for gravity waves.

A general approach to describing weakly nonlinear wave interactions in a finite boundary is presented by Kartashova (1998), the more specific paper by Kartashova, Nazarenko, & Rudenko (2008) is with direct relevance to deep water gravity waves like those studied later in chapter 5. Finite boundaries are of particular importance to low intensity waves since they have 'memory' of the boundary as they reflect off the walls, at higher intensity this memory is lost by an increased number of interactions. A prediction by Nazarenko S. V. (2006) considers a finite rectangular box and finds that,

$$E_\omega \propto \omega^{-6}$$

2.12

2.4 Power Spectrum Predictions for Capillary Waves

As with the gravity wave range there are predictions for the spectra of capillary waves, from WTT (Zakharov, L'vov, & Falkovich, 1992) the spectra for surface elevation are defined as,

$$E_\omega \propto \omega^{-\frac{17}{6}}$$

2.13

And

$$E_k \propto k^{-\frac{15}{4}}$$

2.14

In some experimental techniques rather than measure surface elevation, the surface gradient is measured (Snouck, Westra, & van de Water, 2009) and so these predictions are modified to become,

$$E_\omega \propto \omega^{-\frac{3}{2}}$$

2.15

And

$$E_k \propto k^{-\frac{7}{4}}$$

2.16

It is worthy of note that these indices for surface gradient spectra relate to much shallower spectral slopes, this becomes important when testing WTT theory in the laboratory.

2.5 Direct Cascade

The direct cascade in turbulence describes the transfer of energy from large scales to small scales. The concept was introduced by Richardson (1922) for hydrodynamic turbulence (HDT) in his book on weather forecasting, he put forward the concept that the structure of the ocean is made up of whirls (or eddies) which break up to form smaller whirls, these shapes and structures he suggested were the root of turbulence. The energy from the larger size swirl would pass to a number of small ones until at sufficiently small scales the viscosity of the water would dissipate the turbulence.

The idea was built on by Kolmogorov (1941) and again Kolmogorov (1941a) with a result that has become known as Kolmogorov's cascade. The theory is for very high Reynolds numbers and characterizes two important scales, they are the 'energy containing' scale (large scale) and the dissipation scale (small scale). The energy containing scale is the range at which energy is pumped into the system for example by the wind over the ocean. The dissipation scale is where the energy is dissipated by viscosity. If these scales are close together there will be no turbulence but if they are far from each other then energy needs to transfer from large to small scales and this is described by a cascade.

The intermediate scale doesn't feel the effect of the energy containing scale or the dissipation scale, this is because the energy in the system is being transferred from the energy containing scale to the dissipation scale by non-linear interactions and these interactions are localised so that very little energy is transferred across largely different scales, this allows the cascade theory to exist: This means that only similar sizes can interact for example a 1m vortex cannot interact with a 1mm vortex; from this it follows that there will be a cascade as similar sizes interact and transport energy to smaller and smaller scales.

The important hypothesis is that at any point in this cascade the process can be considered the same; each interaction is self similar regardless of the size. Secondly, it is assumed that every detail of the interactions is not required and the process can be described by the average values for the dissipation rate and the size of the eddies. The

final consideration is that the averaged statistics of the turbulence are stationary; this is a rather useful quasi-reality that allows detailed study of surface waves. The real world is not completely stationary but contains 'intermittency'; these are periods where the self similarity breaks down.

The works of both Richardson (1922) and Kolmogorov (1941) were based on finding a working model of HDT, Kolmogorov managed to produce a relatively simple theory for a very complex problem but it does not capture exactly how the cascade from large scales to small scales happens.

Weak turbulence theory (WTT) does not attempt to be a solution to a system as complex as in HDT where nonlinear interactions are dominant, instead it takes on an intermediate state considering small amplitude waves where linear and nonlinear behaviour coexist, the nonlinear interactions still become dominant in terms of the statistics of the water surface but take longer to do so. These conditions allow the study of the processes via the kinetic wave equation which produces exact solutions, as was stated in 2.3 Power Spectrum Predictions for Gravity Waves which are consistent with Kolmogorov's cascade. The model of WTT has grown from (Zakharov & Filonenko, 1967), (Zakharov, 1968) and predictions from WTT are the current standard for comparisons in numerical and experimental work with turbulent surface waves. The theory is however not a universal model and so further interpretation of most results is required to explain what WTT cannot. WTT also makes an important assumption that the waves exist within an infinite box, the reality of numerical and experimental data is that this assumption cannot be satisfied.

In order to characterise the intensity of waves the nonlinearity parameter can be used, this relates to the wave steepness at the energy containing scale and is defined as,

$$\gamma = k_m A$$

2.17

Where k_m is the wavenumber of waves in the energy containing interval and A is amplitude. For WTT to be valid $\gamma << 1$, this is equivalent to the Reynolds number in HDT when Re >> 1.

2.6 Inverse Cascade

As the name suggests the inverse cascade is the opposite of a direct cascade, the cascade goes towards large scales rather than small scales. For both three wave and four wave interactions energy is conserved, in addition four wave interactions conserve wave action, i.e. the number of waves, (Nazarenko S. , Wave Turbulence, 2011). The energy dissipated by viscosity at small scales has an infinitely small wave action and so the wave action must dissipate at large scales, hence there are two cascades, direct and inverse. At large scales a condensate forms where waves are dissipated by friction from walls in bound conditions or by leaving the system which is analogous to long waves at sea leaving a storm system.

2.6.1 Power Spectrum Predictions for Inverse Cascades

The power spectrum prediction for the inverse cascade of waves is given as (Zaslavski & Zakharov, 1982),

$$E_{\omega} \propto \omega^{-\frac{11}{3}} \tag{2.18}$$

Which is an exact solution to the Hasselmann equation.

2.7 Summary of Theoretical Approaches

In this chapter some basic principles and brief history of the development of wave turbulence theory have been given. Types of surface waves are described in terms of the linear dispersion relation. The characterisation and comparison of chaotic wave fields by the power spectrum is described and special attention should be paid to the spectral predictions for gravity waves since these are compared with experimental data in chapter 5. Large scale experiments on Gravity Waves

3 Experimental Development

In this chapter experimental techniques are introduced in terms of devices used for measurement and methods for generating waves in laboratory experiments and then an examination of a number of experimental results covering large and small scale experiments.

Many techniques are available for measurement of elevation and gradient of a liquid surface, most of these take measurements in a single point however in recent years measurements along a line and 2d reconstructions of the surface have been developed and implemented. Here a number of these techniques are presented but although this is not exhaustive it represents the highlights and currently most utilised approaches.

3.0 Wire Probes

Capacitance and resistance based wire probes are a traditional method for measuring wave elevation and they are one of the most commonly used devices for extracting surface elevation data from a wave field. There are numerous examples of their deployment mainly in large and small scale experiments, much of the development is recorded thirty (Lange, Jahne, Tsschiersch, & Iimberger, 1982), (Liu, Katsaros, & Weissman, 1982) to fifty (Moore J. B., 1964) years ago but they are still used for the relative ease and low cost of their construction and implementation; they offer a robust solution.

A capacitance probe usually consists of a single wire covered with a thin polymer layer partially submerged in the liquid. There is a capacitance between the wire and the liquid that changes with the depth of submergence and hence it can be used to monitor wave elevation. The typical limiting factor in terms of the range of waves the probe can be used to measure is the size of the meniscus formed around wire (Strum & Sorrell, 1973), this means that for water waves they are only suitable for gravity and gravity-capillary range waves, typical frequency ranges reported vary from 15 Hz to 80 Hz dependant on the design and choice of materials. Experiments can of course be conducted on different liquids, Falcon, Fauve, & Laroche (2007) capture data from surface waves on mercury in excess of 100 Hz.

There are commercially available wire probes (HR Wallingford) although these are generally aimed at monitoring the standard deviation of surface elevation or pumping range amplitudes in a wave regime where another variable is being tested rather than for observing the spectra of waves. They are unsuitable for this because they are based on a two wire structure, although wire in this case is a misleading term since the diameter is usually quite large, on the order of 5 mm and are rigid in construction usually stainless steel. The signal is altered by the changing resistance between them as the water elevation changes, this gap between the wires is usually significant and means that only waves with wavelength above ~5 cm are measureable; (Denissenko, Lukaschuk, & Nazarenko (2007) use a similar purpose built capacitance probe device with spacing between the two wires 1 cm to achieve greater resolution than the commercial versions although they later move to a single wire capacitance probe for further increased resolution.

3.1 Optical Techniques

Optical techniques for measurement of the surface waves cover a broad range of approaches from point like measurements to 3d surface reconstruction. The advantage of optical techniques is that they are non-invasive and so there is no meniscus effect and they are non-inertial. Beyond this advantage each system has its own pros and cons and these will be discussed in the subsequent sections.

3.1.1 Position Sensitive Device Based Techniques

A Position Sensitive Detector (PSD) can be used in the study of surface waves by either detecting wave elevation (Lommer & Levinsen, 2002) or more commonly, detecting the gradient of the surface in a given position by measuring the position of a light spot from a refracted beam on a flat semiconductor surface (Snouck, Westra, & van de Water, 2009).

Lommer & Levinsen (2002) used a fluorescent laser technique which implements a PSD to detect surface elevation. A fluorescent dye is used so that a blue laser creates a fluorescent green dot on the liquid surface which is then imaged onto a PSD by a microscope lens, the lens and PSD are under an angle so that the spot on the surface captures the change in elevation. The difference in the colour of the laser and the fluorescent spot is important in this case because a filter in front of the PSD can be used to remove stray reflection from the laser whilst still capturing the fluorescent spot.

Rather than measure surface elevation Snouck, Westra, & van de Water (2009) use a PSD based system to measure surface gradient of waves on silicon oil. Two configurations are utilised so that in the first a point like measurement is obtained and in the second the measurements are taken along a line. For measurements in a point a laser is positioned above and perpendicular to the liquid surface, waves refract the beam and a PSD beneath the container obtains the x and y coordinates where the beam strikes it by a centre-weighted average. This system can be inverted so that the PSD is above the surface and the laser positioned below. The angle measured in the second scenario is slightly larger due to the refractive indices of air and the silicon oil, a simple graphical representation of this type of setup is shown in Figure 3.1.

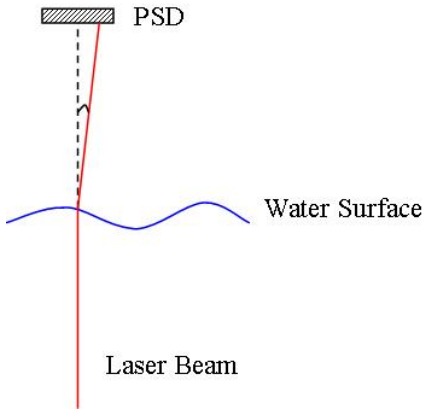

Figure 3.1 – Simple setup to measure the refraction from a water surface of a laser beam on a PSD sensor

Before describing the adaptation to measure along the line, staying with point like measurements, in the case where surface elevation is measured the restriction on this system come from the geometry of the setup, namely the angle under which the microscope lens and PSD are placed. At steep angles close to perpendicular to the surface there will be a significant drop in resolution because the perceived change in height of the spot will be very small. At shallow angles close to parallel there will be a high resolution but risk of interference from other waves crossing the optical axis and so there is a limit on the wave amplitude that can be measured. Clearly some balance has to be found but the geometry of the setup used by Lommer & Levinsen (2002) is not provided.

By measuring the surface gradient of the waves directly the issues faced with the elevation example are in a sense removed, there are however still restrictions on the measurable gradient from the size of the PSD sensor used and its location relative to the surface. If the angle of refraction produced by the surface is too large the sensor can be moved closer to accommodate, equally if the angle is very small the sensor can be placed at a greater distance to ensure the full dynamic range of the sensor is used. This system of measurement is more transparent that the previous example but in the case of waves excited by an electromagnetic shaker as in the case of Snouck, Westra, & van de Water (2009) the distance between the PSD and the liquid surface will have small changes and so the measured angle will consequently vary, this error will decrease as the distance between the undisturbed surface and the PSD increase.

Measurements of the surface gradient along the line are advantageous because they allow access spatial statistics, the adaptation to use the PSD setup in this way is presented by Savelsberg, Holten, & van der Water (2006). The essence of the technique is the same as with point like measurements but this time the laser scans the surface along a line by means of an oscillating mirror, the refracted beam is directed onto a frosted glass plate and then imaged onto the PSD by a lens. The glass plate and lens are additional requirements due to the length of the line; the refracted beam cannot be directed straight onto the PSD. Measurements are recorded twice for a given point on the line in a full period of the oscillation of the mirror. Triggers for the mirror and the measurements are synchronised so that the position of each measurement on the surface is known. The drawback of measurements along the line is a decrease in the maximum sampling rate from that which is achievable in point like measurements, theoretically in this case limited at 1000 Hz by the oscillations of the mirror although in practise it was found that beyond 100 Hz the signal reached the level of noise. Nevertheless the system presented by Savelsberg, Holten, & van der Water (2006) is a marked improvement of previous incarnations where the maximum frequency of wave that could be observed was 35 Hz (Bock & Hara, 1995).

3.1.2 Imaging of Wave Profiles

Profile imaging is an experimental technique based on taking a cross section of the liquid and air interface in order to capture an instantaneous wave profile. The technique has been around in many guises for a number of years, Bonmarin & Ramanonjiarisoa (1985) use a series of three focused lambs to illuminate a cross-section 1 m long and

light sheet width ~ 10 mm, the width is variable since the illumination is not parallel. The water contains Fluoresceine so that the resulting illuminated profile can be captured via film camera with a high frame rate of 500 fps. The study is concentrated on breaking gravity waves and so the high frame rate captures the rapidly changing profile well but the thick light sheet means that small scale features cannot be resolved. An improved version of the same technique is presented by Bonmarin, Rochefort, & Bourguel (1989), the illumination is improved but the key development was a more automated handling of the image processing, indicative of improving technology rather than a change in the approach.

In a much more recent study on wave evolution Shemer & Dorfman (2008) simplify the acquisition of a wave profile by using a window in the side of a tank to image waves as they pass. This approach removes the need for additional illumination and deals with the issue of light sheet thickness provided the camera is perpendicular to the captured profile. The issue with this method is that using the contact line with the side of the tank is not always appropriate, in this experiment the issue is minimised because a narrow channel is used to observe short wave groups and good agreement of the measured amplitude is found with wire probes measurements: However in a developed turbulence wave regime measurements are preferable from a more central area of the tank away from the boundary.

The optimised approach to acquiring wave profiles is to use a laser illumination as in (Mukto, Atmame, & Loewen, 2007) and (Lukaschuk, Nazarenko, McLelland, & Denissenko, 2010) which uses a technique based on the former. The laser sheet illumination means a very thin light sheet can be produced and so small scales of the profile are resolvable, the resolution of the technique is now based mainly on the camera and the technique can still be deployed anywhere across the surface. Instead of Fluoresceine mixed in the water, fluoresecent seeding particles and Rhodomine 6G are used respectively. Seeding particles on the surface can have an issue with inhomogeneity in the illuminated profile, the issue is improved using Rhodomine dye instead because it is dispersed throughout the body of water.

3.1.3 Fourier Transform Profilometry

Profilometry is a method for obtaining 2-d surface elevation data, it is analogous to 3-d vision like that used by the film industry which uses a system of two cameras to provide perspective and generate a 3-d image. Profilometry replaces one of those cameras with a

projector, the principal of generating an image based on two different perspectives is the same but the projector displays a pattern of known characteristics which allows a more accurate reconstruction of the surface to be created.

Fourier transform profilometry (FTP) was proposed in the early 1980's by Takeda, Ina, & Kobayashi (1982) and Takeda & Mutoh (1983), it has been considered for many years as an exciting way to access a reconstruction of a 3-d surface but it is only recently that technology has allowed it to be implemented in such a successful way. The technique has enjoyed limited success until the last decade where technology now allows the technique to be implemented more cheaply, accurately and data processed faster, as a result its use is growing into diverse areas for example as a medical device for shape guided radiotherapy (Moore, Burton, Skydan, Sharrock, & Lalor, 2006) and in electronics as a quality control for printed circuit boards (Yen, Tsai, & Yang, 2006) among many others.

Fourier transform profilometry was initially proposed using a Ronchi grating pattern, with modern digital projectors it is possible to illuminate the surface by a sine wave pattern which lends itself to the Fourier transform ideally. The surface profile of objects and surfaces are reconstructed by a process of triangulation based on the geometry of a given system. The equations for this were presented for a system with collimated projection in early papers by Takeda & Mutoh (1983), they relate the geometry of the system to an observed change in phase between the original projected pattern and the same pattern projected onto an object.

The equations presented in early papers were amended by Rajoub, Lalor, Burton, & Karout (2007) to use a non-collimated projection of the pattern, which is the realistic case when implementing the technique, the new equations are simulated to prove their argument but the group stop short of an experimental set of data. The paper is added to by Maurel, Cobelli, Pagneux, & Petitjeans (2009) who provide a practical example of a simple geometric shape to confirm the simulations in the afore mentioned paper. The equation for reconstruction of the surface height when non-collimated projection is used is given as,

$$h(x', y') = \frac{L\Delta\varphi}{\Delta\varphi - \omega_0 D}$$

3.1

where L is the distance between plane of projection and projector, D is the distance between camera and projector, Δφ is the phase difference and where,

$$x' = x - \frac{h}{L}x, \qquad y' = y - \frac{h}{L}y$$

3.2

where, x and y are coordinates of the image plane; a simple schematic of the type of setup used is shown in Figure 3.2.

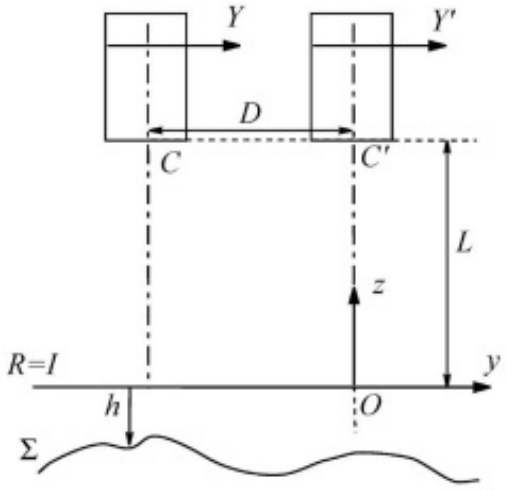

Figure 3.2 – Profilometry; arrangement of projector and camera in parallel axes geometry, C is the projector, C' is the camera, R is the reference plane, I is the image plane. **(Maurel, Cobelli, Pagneux, & Petitjeans, 2009)**

Clearly accurate reconstruction of surface height is of paramount importance for use as a measurement device but it is dependent on more than reconstructing the surface from the geometry. The correct pattern choice is important; if a pattern with a short period is used to measure objects with a large height (relative to the pattern) then there will be phase jumps. It is possible to correct these jumps and it is also possible to choose a pattern of sufficient period to avoid having them at all, this does however limit the height that can be measured. Dealing with the phase jumps can be a difficult issue and various algorithms have been developed eight of the more successful algorithms are

brought together in a comparison by Zappa & Busca (2007). These unwrapping algorithms tend to require significant computer time which means if they can be avoided through the configuration of the setup and experiment design this is preferable; this is the case with the experiments presented in this thesis.

In order to be able to project on to the surface of water a pigment has to be added, this can be as simple as adding paint to the water. However this has drawbacks and support for the use of titanium dioxide as a pigment is presented by Przadka, Cabane, Pagneux, Maurel, & Petitjeans (2011), the issue considered is that many commercial paints that contain titanium dioxide and can be used to colour the water for use with profilometry contain surfactants which when mixed with water are absorbed at the surface. This is undesirable because it changes the conditions of the experiment; it becomes more complicated because there are in effect two layers and the surface tension is also altered. To avoid this effect titanium dioxide can be dispersed in deionised water. Deionised water is used because it makes the suspension of titanium dioxide more stable. In tap water the titanium dioxide will coalesce and as a result sedimentation will occur more rapidly which results in a loss of contrast at the surface and the profilometry technique becomes unusable.

3.2 Wave generation in laboratory experiments

There are a number of options available to experimentalists for the excitation of wave regimes, wind tunnels, paddle and electromagnetic shakers. The choice of excitation depends on the aims of the experiment, wind generated waves like those presented in Longo, Liang, Chiapponi, & Aguilera Jimenez (2012) which is the latest in a series of papers offer a good example of an experimental setup but their measurements are largely concerned with the currents beneath the waves, in general this is the favoured excitation type for this kind of study. Surface waves can also be studied successfully, Zhang (1995) uses a novel optical method similar to the point like measurements of surface gradient but in an array and using a CCD camera rather than a PSD, to produce 2d wavenumber spectra. In some cases like (Longo, Chiapponi, Makela, & Liang, 2012) which study the boundary layers either side of the air-water interface wind generation is a necessary part of the experiment rather than a choice.

The preferred choice of excitation for studying surface waves is the paddle type generator and electromagnetic shakers; they offer more access to the surface with a

variety of techniques without being concerned with interfering with the wind and a very close control over the frequency or frequencies that are selected to be generated. Paddle type generators have a number of different styles but the result is the same, they can be driven by different means but the result is a displacement parallel to the liquid surface. Electromagnetic shakers are used usually with some sort of tank containing the liquid mounted on them and then driven by an amplified signal to create parametric waves on the surface, note that these shakers can also be used to drive the paddle type generators.

For some recent examples, the electromagnetic shaker has been used by Xia, Shats, & Punzmann (2010) and also in number of other studies at the Australian National University and by Snouck, Westra, & van de Water (2009). Shakers are the most successful method for the excitation of parametric waves also referred to as Faraday waves because of the first observation by Faraday (1831), however paddle generators are also able to generate parametric cross-waves: A novel paddle type generation is used by Moisy, Michon, Rabaud, & Sultan (2012) where the paddle is fully submerged beneath the liquid surface, this is done in order to study the parametric cross-waves. The suggested advantage of submerging the paddle is that low amplitude cross-waves can be studied without the movement of a meniscus that would usually occur in other varieties of excitation. Cross-waves can still be generated without submerging the paddle though and this can be an undesirable complication of the system.

In experiments conducted in large wave tanks like the ones described in 3.3 Large Scale Experiments, paddle type generation of waves is the only real option because it is simply not practical to mount tanks bigger than even 0.5 m on a shaker. The drawback of the paddle type generation is that it doesn't simply generate waves on the surface as with parametric excitation from a shaker. It is necessary that at least part of the paddle is under the surface and so a turbulent flow may also be generated beneath the surface which complicates the experiment.

3.3 Large Scale Experiments

Large scale experiments are quite rare, a large part of which is because there are relatively few tanks or flumes available to conduct such experiments. These types of experiment are significant because they allow the study of gravity wave turbulence in a relatively wide inertial range. Lukaschuk, Nazarenko, McLelland, & Denissenko (2010) present results for wavenumber and frequency spectra and compare their observations

with some of the theories and predictions introduced in section 2.3. In Figure 3.3, reproduced from the afore mentioned work, k and w slopes are shown for different amplitudes of forcing. There is some evidence to support the Zakharov-Filonenko prediction, the data points in red represent increasing amplitudes of the wave regime as they approach the point ZF (Zakharov-Filonenko prediction). If greater amplitudes could be achieved it looks likely from this result that the prediction could be achieved. In reality however that amplitude was not achievable due to increased breaks and splashing. While this support of the theoretical prediction is encouraging it should be remembered that the prediction is based on weak non-linearity and where there are breaks and splashing the non-linearity is already quite strong.

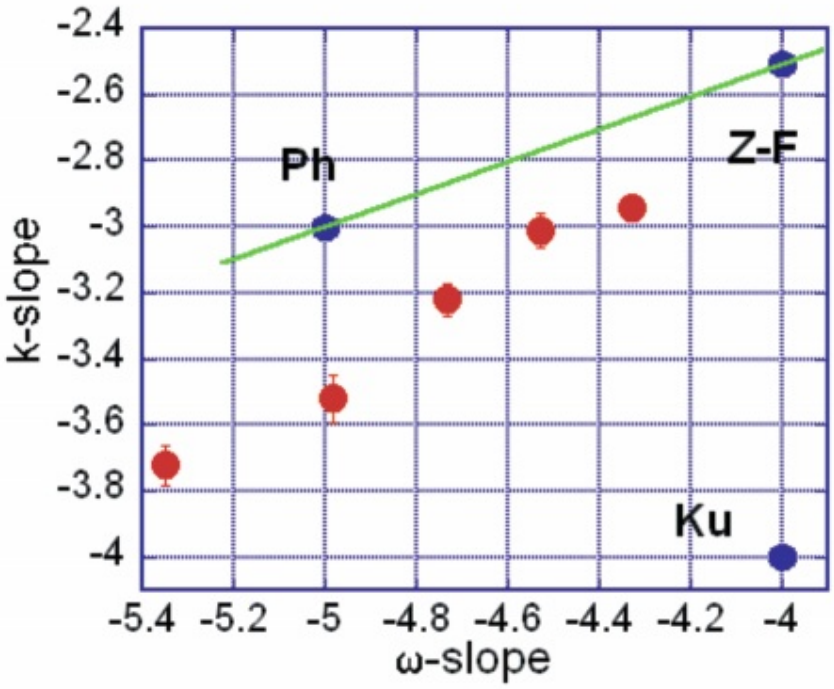

Figure 3.3 – Experimentally obtained ω and k slopes for different amplitude of wave excitation shown with theoretical predictions, Ph – Philips, Z-F - Zakharov-Filonenko and Ku – Kuznetsov **(Lukaschuk, Nazarenko, McLelland, & Denissenko, 2010)**

The slopes measured increase as amplitude decreases, this is explained via finite size effects; at low amplitude the number of non-linear interactions is reduced and at high amplitude there are breaks and splashing.

3.4 Statistics from 2d surface reconstruction

The work described in this section is possible as a direct result of the advances in the profilometry technique outlined in 3.1.3 Profilometry.

Chekroun, et al. (2012) present two results, one regarding the interaction with structures and the second an example of FTP being used for capturing the ω-k spectrum to demonstrate the linear dispersion relation. The result is in agreement with theory and much clearer than a similar attempt to demonstrate the dispersion relation presented by Herbert, Mordant, & Falcon (2010) where the dispersion relation shows several branches. Both of these are reproduced in Figure 3.4

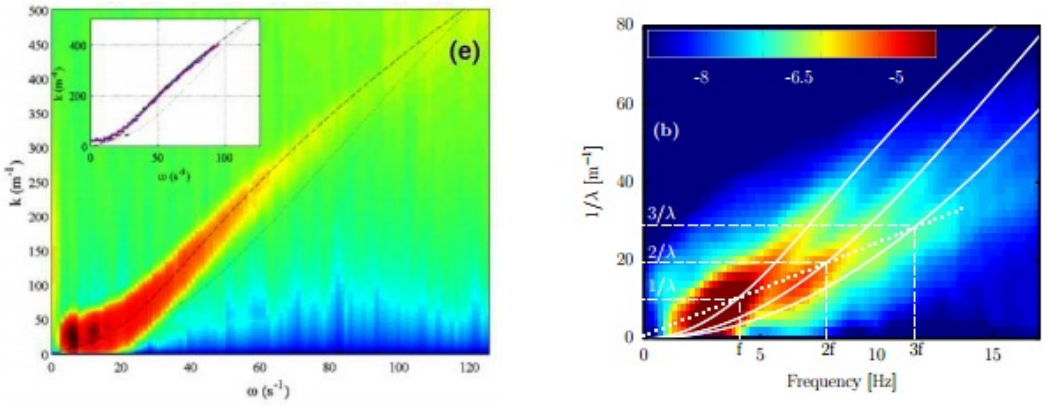

Figure 3.4 – Left: Experimental observation of dispersion relation **(Chekroun, et al., 2012)**. Right: Experimental observation of dispersion relation **(Herbert, Mordant, & Falcon, 2010)** showing several branches.

These several branches are explained as secondary branches of the non-linear dispersion relation, the root cause is harmonics on the low frequency carrier wave described as Nω and Nk. These harmonics travel at the same phase velocity of the carrier wave and should only appear at high excitation of the waves, since for the harmonics to appear the wave should be strong and sharp crested. The two experiments are at similar depths 5 cm and 7 cm respectively and similar wave amplitude range, the excitation frequency is the notable difference with 2 frequencies 2 and 3 Hz used in the first and white noise between 1 and 4 Hz in the second, thus the difference in result is still to be fully explained. The two studies are the first of their kind to produce ω-k spectrum from 2d surface data since both experiments are conducted on similar setups but produce

different results it is evident more work in this direction is required, they are both good examples of how profilometry is moving the study of surface waves forward.

3.5 Evolution and decay of wave regimes

There is relatively little published work in the study of non-stationary wave regimes, Kolmakov, Levchenko, Brazhnikov, Mezhov-Deglin, Silchenko, & McClintock (2004) and Brazhnikov, Kolmakov, Levchenki, Mezhov-Deglin, & McClintock (2005) present results on the development and decay of wave turbulence in the capillary range on the surface of liquid hydrogen. Their experimental results show that during the decay process the spectral peak associated with the excitation frequency in the stationary regime does not shift and merely decreases in amplitude. Meanwhile the high frequency part of the spectrum far from the main peak is lost first and the right hand edge of the spectrum shifts towards the excitation frequency range.

On the surface of mercury and a number of other liquids including water Deike, Berhanu, & Falcon (2012) present observations of capillary wave decay, the same observation as with the surface of helium is seen in the evolution of the spectrum; the high frequency cut off moves toward the energy containing scale.

The decay of the main peak of the spectrum is found to be exponential rather than a power law as predicted by Falkovich, Shapiro, & Shtilman (1995) and indeed in other predictions for the decay of turbulent regimes (Pope, 2000). This is made all the more unusual because the self-similar spectrum is maintained although with the shift of the high frequency cut off the inertial range reduces.

These works are all rather recent and highlight the growing interest and to the best of the author's knowledge there are no experimental observations on the decay of gravity waves. This rather obvious gap in the understanding of surface wave turbulence is one that is addressed within the scope of work presented in chapter 5.

3.6 Studies of the inverse cascade of waves

For those that study surface waves the inverse cascade is one of the most elusive features to observe, numerically it has been confirmed by Annenkov & Shrira (2006) and Korotkevich (2008). Korotkevich (2011) also considers the influence of the inverse cascade and its associated condensate on the dispersion relation for gravity waves and also the influence on the direct cascade (Korotkevich, 2012). The first and currently only experimental observation of a possible inverse cascade was made by Deike,

Laroche, & Falcon (2011), the result of which is reproduced in Figure 3.5. The low frequency condensate to the left of the excitation range is clearly visible at a frequency close to the resonant frequency relating to half the length of the tank, L/2. The experiment is conducted using mercury so the forcing range is on the interval between the gravity capillary range, the gravity wave range is at f < 17 Hz.

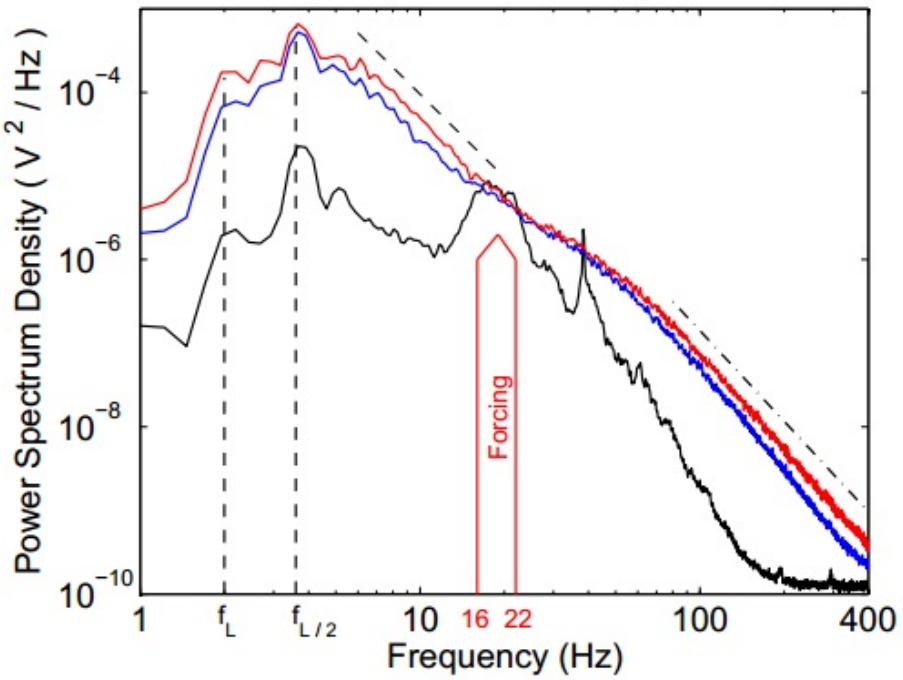

Figure 3.5 – Experimentally obtained inverse cascade for different amplitudes of wave excitation using a paddle type generator **(Deike, Laroche, & Falcon, 2011)**

Other explanations for the low frequency observations are suggested and ruled out, these include; parametric waves from the wave maker and the appearance of a zero frequency sideband. The zero frequency sideband is ruled out quite quickly; this effect is described in Xia, Shats, & Punzmann (2010) as a consequence of the broadening of spectral harmonics and appears as a hump in the frequency spectra at frequencies typically less than 1 Hz; the spectral maximum for the inverse cascade observation was 3.6 Hz and so it seems unlikely that this effect is important here.

Parametric waves from the wave maker would seem the most likely alternative explanation; the pumping range of 16 Hz to 22 Hz could see waves of 8 Hz to 11 Hz generated and these waves could fill the scaling interval of the inverse cascade. There is

however no discernible peak in this area, it begs the further question why are there no parametric waves generated, Garrett (1970) presents the theory that the appearance of cross-waves is dependent on the amount of water displaced by the wave maker. In the inverse cascade experiment the immersed part of the wave maker is less than two thirds of the water depth and this is claimed to ensure that parametric cross-waves are not generated although this is not documented elsewhere.

The low frequency condensate is described rather logically in terms of its placement relative to the resonant frequencies of the tank based on length L = 20 cm, there is another characteristic length in the system which should not be forgotten but is not discussed by Deike, Berhanu, & Falcon (2012), that is the length of the wave generator. In this case it is similar in size to L/2 at L_p = 13 cm. The frequency associated with this length according to the dispersion relation is 2.9 Hz and for $L_p/2$ it is 4.8 Hz. If the minimum amplitude result (the black line in the plot) is considered these two values fall immediately to the left of two humps observed in the spectrum. The paddle length parameter would then appear to be not hugely important although it would be interesting to vary its length and see if this impacts the result, as mentioned in discussing types of wave makes in section 203.2 the paddle will generate a flow beneath the surface and this complicates the experiment because it is dealing with both wave turbulence and hydrodynamic flow.

The study of the inverse cascade, certainly experimentally is still in its infancy and so further characterization of its features will undoubtedly be the topic of many studies within the next few years. The first result shows good agreement with theory but questions still remain over the spectral development of the cascade and how various experimental parameters might change the observation.

3.7 Dragon wash

The Dragon Wash is a remarkable ancient Chinese bowl, typically made of bronze and filled with water. The bowl has two hollow handles which when rubbed with wet hands makes the bowl ‘sing’. Different ways of rubbing the handles produce different sounds but what is relevant to the study of water waves is that while this sound is being produced capillary waves are produced around the edge of the bowl, by increasing the intensity of rubbing droplets appear at the edges and begin jumping, further to this it is

also possible to observe a low frequency wave in the gravity range (Denissenko & Hsieh, 1998).

Over the last twenty years there has been a steady interest in the dragon wash phenomenon it was studied experimentally and theoretically by Wang (1993) and Wang (2005) mainly concentrating on the mechanical properties of the basin. The actual water surface has been studied in numerous ways to attempt to characterise and explain the different aspects of the phenomenon. These experiments are usually carried out in circular vessels to simulate the dragon basin; typically these are made of Perspex or similar plastics and are excited by sidewall forcing to mimic the effect of rubbing the handles.

The surface of the water was photographed by Denissenko & Hsieh (1998), in this study it was noted that the low frequency gravity wave was observed when the excitation frequency was higher than the resonant frequency of the elastic walls of the plastic container used.

Spatial resonance is a model that was developed by Huntley (1972) and Mahony & Smith (1972) as an explanation of low frequency instability in containers with horizontal side wall excitation. The proposed model describes non-linear coupling between the side wall of the vessel and the surface waves through non-linear boundary conditions. In a more detailed study Huntley (1977) shows that a low frequency mode of frequency f can be generated by high frequency F excitation of the side wall through generation of a sideband pair of frequencies at $F \pm f$ as long as one of these side bands falls within the bandwidth of the resonant mode of the side wall. Mahony & Smith (1972) suggests that the low frequency instability will appear most easily when the excitation frequency is greater than the resonance frequency, this is depicted by the stability curves reproduced in Figure 3.6.

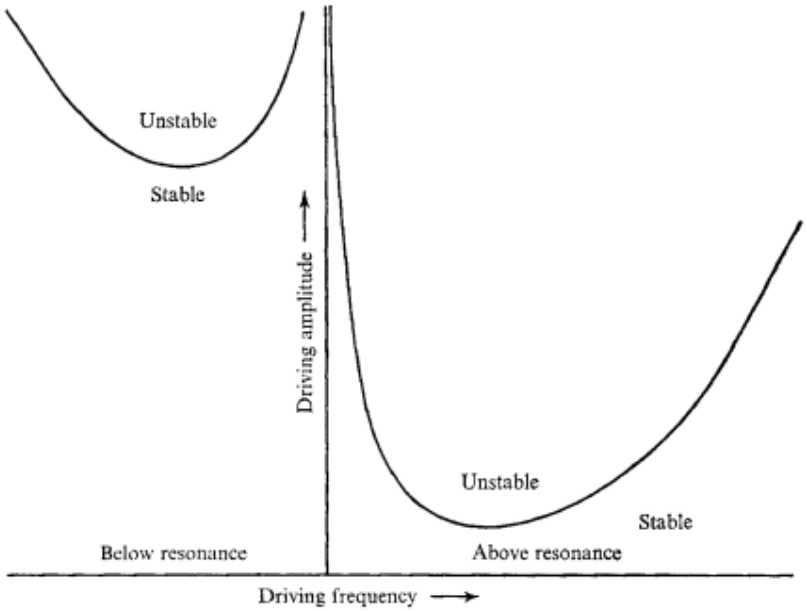

Figure 3.6 – Stability curves for low frequency instability **(Mahony & Smith, 1972)**

The first study of the flow inside a dragon basin was conducted by Wei, Wang, Yan, Du, & Chen (1997) using particle image velocimetry (PIV). This type of measurement is used to consider the jet flow instability or jet induced sloshing. This first described by Okamoto, Madarame, & Hagiwara (1991), a detailed study including photographs using a similar technique to Denissenko & Hsieh (1998) and PIV measurements is presented by Lee, Peng, Yuan, Wu, Zhou, & Hussain (2011). This model attributes the appearance of the low frequency wave to jets generated at the side wall which flow towards each other in the centre of the vessel where they interact and the flow is redirected downward, this has the result of creating a maximum upward induced velocity at the wall at the strongest vibrating point along the side wall. Jet instability then occurs at a critical value of the Strouhal number and due to the compact size of the vessel vortex-shredding feedback occurs and so the jets oscillate and ultimately the low frequency wave is observed.

4 Experimental techniques: Measurement devices deployed in experiments in this thesis

In this chapter the devices used in the experiments presented in this thesis are described. Included are two point-like devices, wire probes and a PSD based surface gradient device and two spatial techniques for wave profiles and 2-d surface reconstruction using Fourier Transform Profilometry. All have been previously introduced in chapter 3.

4.0 Wire Probes

The wire probes described in this section are a variant used in experiments presented in chapter 5 to study gravity wave turbulence.

4.0.1 Construction and Implementation

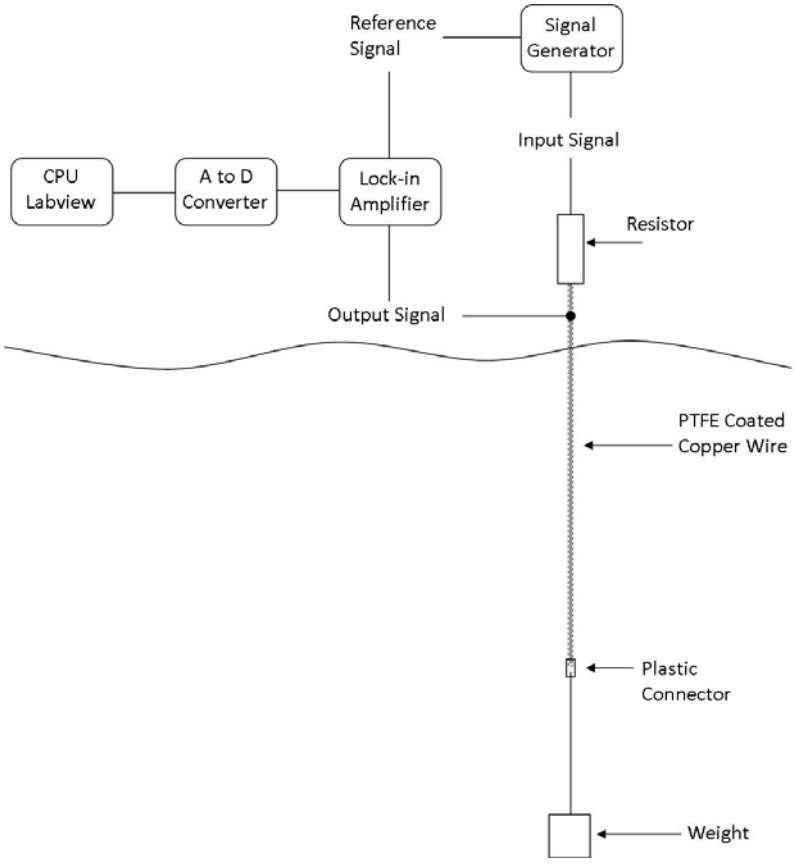

Figure 4.1 – Schematic of the wire probe device utilised in the experiments presented in this thesis

The basis of the operation of the wire probe is as an AC voltage divider, see Figure 4.1. The wire is coated in a thin layer of PTFE and so there is a capacitance between the copper wire and the weakly conductive water. The wire is positioned perpendicular to the surface and partially submerged. As the height of the water around the wire changes so does the capacitance between the wire and water and surface elevation as a function of time can be measured.

The probes are supplied with a voltage from a signal generator which is also supplied to a lock-in amplifier as a reference signal, the returning signal from the probe is also input into the amplifier and the resulting output is a full scale signal in the range 0-10 V, this system is shown visually in Figure 4.1. The output signal is then recorded to an .lvm file using a Labview program and an Analog to Digital converter, the program in labview allows monitoring of the wave elevation and the instantaneous power spectrum of the signal.

4.0.2 Calibration

The procedure for calibration requires the output voltage at as many different water depths as is realistic to implement across the working range of the probe. This can be done manually but in the data presented here the calibration was semi-automated using a motorized translational stage, this makes the process both consistent and economical since a large number of points can be gathered rather quickly. Figure 4.2 shows the signal for two probes as recorded V(t) and convereted to depth relative to the inital posistion by the calibration coefficients found from fitting a polynomial function to the plot of voltage against depth shown in Figure 4.3.

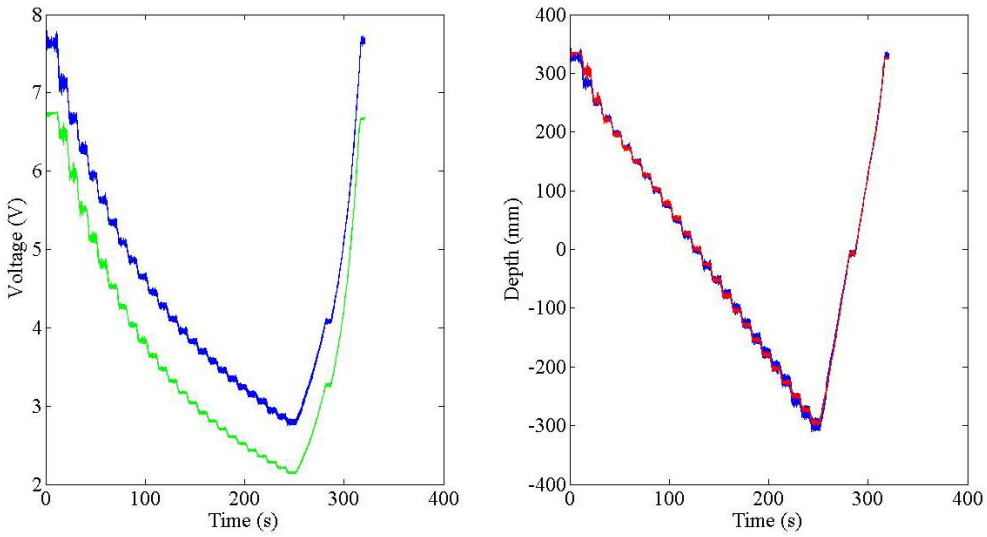

Figure 4.2– Left: Example signals for 2 capacitance probes during calibration. Right: Same signals as left plot after applying the calibration coefficients to obtain depth from voltage

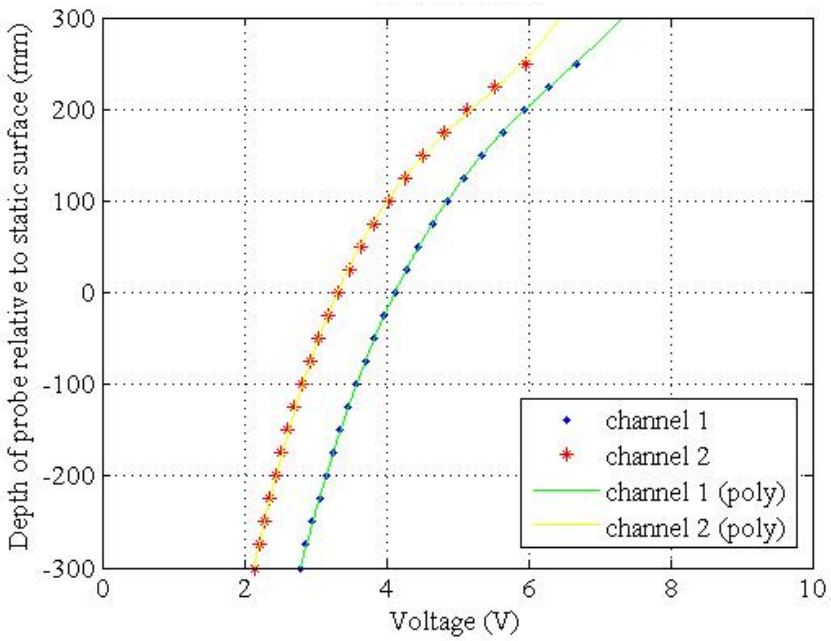

Figure 4.3 – Voltage vs Depth of 2 capacitance probes relative to the still water surface, fitting provides coefficients for calibration

Following this calibration process recorded voltage signals can be converted to wave elevation in millimetres, a sample signal from the experiments in chapter 5 is shown in Figure 4.4; this signal can then be processed to provide statistics of the wave field.

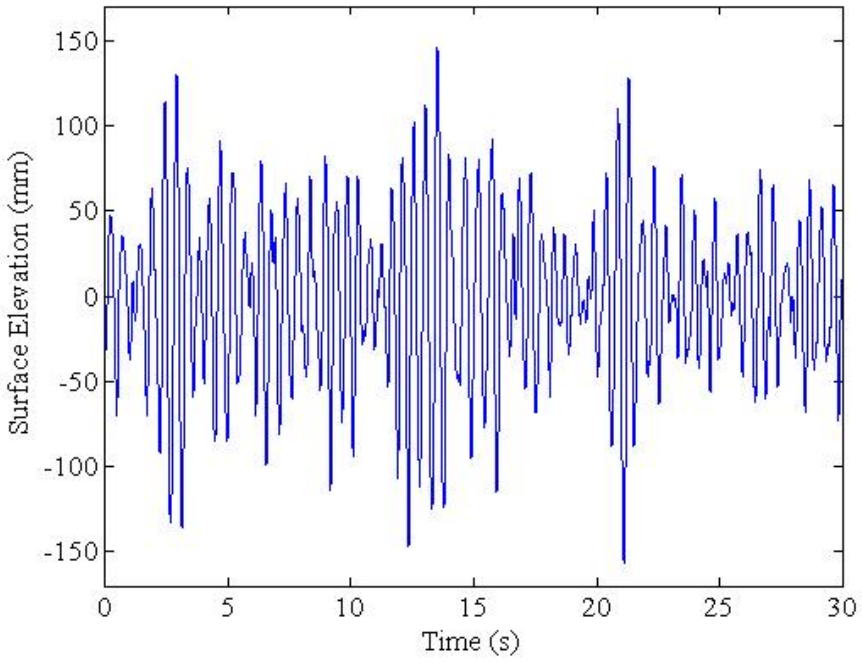

Figure 4.4 – Sample of surface elevation of paddle generated waves after calibration

4.1 Laser based Surface Slope Measurements

Laser based surface slope measurements can be obtained using a position sensitive device (PSD) as outlined in section 3.1. The simplest form of setup to achieve the measurement of the surface gradient is as shown also in that section. The laser beam (He-Ne in this case) is directed perpendicular to the undisturbed surface and then on to the PSD device, when the waves are generated on the surface of the water the beam is refracted and the position of the beam on the sensor consequently changes.

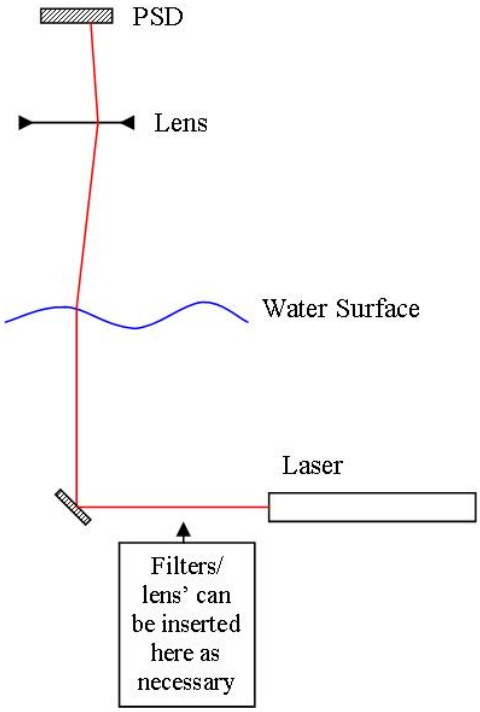

Figure 4.5 – Modified system for surface gradient measurement from that of (Snouck, Westra, & van de Water, 2009) to include an additional lens

The intention in the experiments presented in this thesis is to measure parametrically excited waves using a tank mounted on a shaker. From previous examples of the use of this device it was noted that there is a small error associated with this simple setup when studying parametric surface waves generated from a shaker due to the changing distance the between liquid surface and the PSD. To minimise the error the PSD needs to be placed as far from the surface as possible although will limit the angle it is possible to measure. By placing the PSD at the focal plane of a lens, as in Figure 4.5, the error is removed because the position on the sensor is only dependant on the angle of refraction this can be shown using the lens equation.

The lens equation is given as:

$$\frac{1}{l'} - \frac{1}{l} = \frac{1}{f'}$$

For a general position h on the lense:

$$\frac{h}{l'} - \frac{h}{l} = \frac{h}{f'}$$

$$h = l'tan\beta = ltan\alpha$$

$$tan\beta - tan\alpha = \frac{h}{f'}$$

For a position H on the sensor:

$$H = ltan\alpha - f'tan\beta$$

Substituting for $tan\beta$:

$$H = ltan\alpha - h + f'tan\alpha$$

$$H = f'tan\alpha$$

A lens can now be selected to make the best use of the sensor by utilising its full area:

$$f' = \frac{H}{tan\alpha}$$

4.1

For example, for $\alpha = 10^o$ and $H = 0.7\ cm$, $f' = 3.97\ cm$ so a lens with focal length 4 cm could be used and then dependant on the position of the system relative to the surface the aperture of the lens can be chosen accordingly.

The use of the lens equation mean the system is only optimised for measuring small angles but in the case of surface waves this is typically the case. The addition of the lens does however mean that the size of angle measured can be controlled independently of the distance the lens and PSD are placed at by changing the aperture of the lens. This flexibility means that working with different water depths can be done with relative ease.

The major advantage the PSD has over the wire probe, also for point like measurements, is that the PSD is non-invasive, the advantage the wire probe has is that it can deal with breaks whereas the PSD cannot. In the case of a wave break where the laser beam crosses the surface the light will scatter and a proper measurement cannot be made. In the laboratory conditions considered using the PSD the regimes studied should be at amplitudes where breaks are minimized.

4.1.1 Calibration

Calibration of the PSD (Hamamatsu S1880) sets the relationship between a position of the laser spot on the PSD surface described in rectangular coordinates with zero point at the centre of the sensor and output voltage of the electronic amplifier. Calibration only needs to be done once since the circuit produces an output voltage that is independent of light intensity and only changes with position on the sensor, a circuit diagram is provided in Appendix A. An example of the calibration is shown in Figure 4.6. The calibration shown was obtained by moving the sensor relative to the laser spot but could equally be done by moving the laser or via rotation of a mirror. There is no constraint on the calibration relating to the spot size of the laser as the sensor works on a centre weighted average.

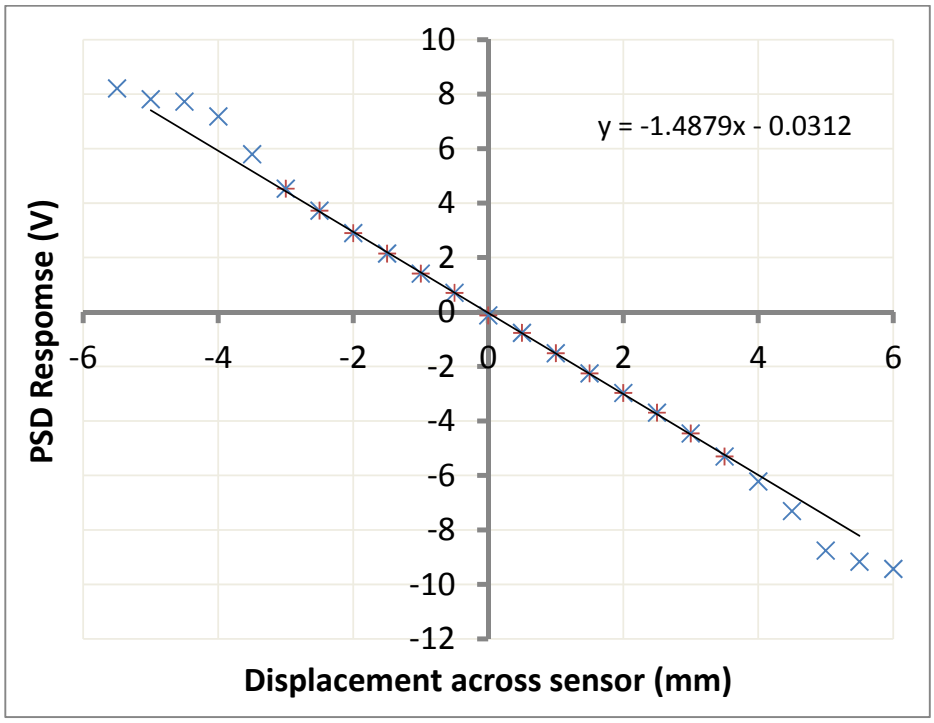

Figure 4.6 – Example of calibration of the PSD response by moving a laser spot across it at known increments

4.2 Fluorescent Laser Imaging of Wave Profile

Fluorescent laser imaging is a technique where a cross-section of a water surface can be captured by a camera and processed to give statistics on wave vectors and in some cases time dependant elevation if a high enough frame rate can be achieved. The technique is particularly desirable because it is non-invasive. The technique presented here is similar

to that used by (Mukto, Atmame, & Loewen, 2007) who used fluorescent seeding particles instead of a dye.

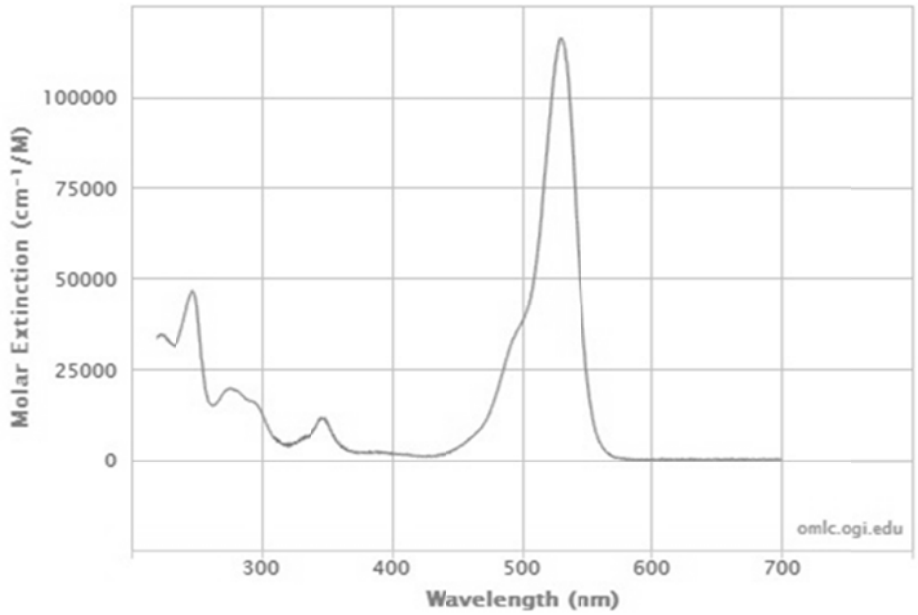

Figure 4.7 – Absorption of light at wavelengths of light by Rhodomine 6G **(Prahl, 2012)**

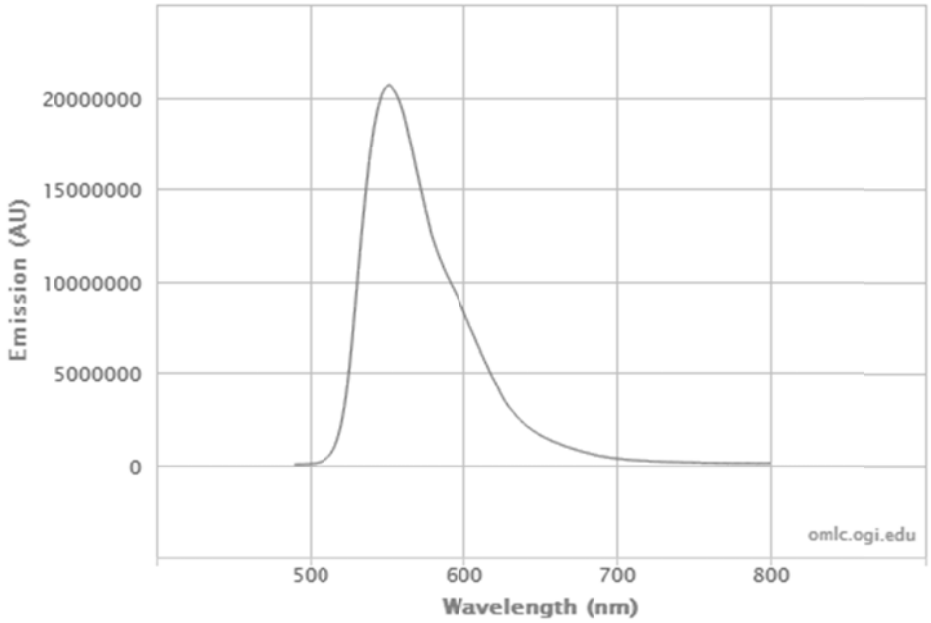

Figure 4.8 – Fluorescence of Rhodomine 6G at different wavelengths **(Prahl, 2012)**

In order to fluoresce the water Rhodomine 6G is diluted in the body of water, this is appropriate for lasers with wavelengths ~520 – 540 nm, full fluorescence and absorption data can be found in *PhotochemCAD 2* a free to download software using data from (Dixon, Taniguchi, & Lindsey, 2005) and is reproduced in Figure 4.7 and Figure 4.8. The laser used in the experiments presented in this thesis was a pulsed Yag laser (Energy 120 mJ, wavelength 532 nm). The laser beam is expanded to produce a light sheet and is positioned perpendicular to the water surface. A camera under a known angle captures the resulting cross section. If the geometry is known or if calibration images are taken it is possible to process the images to result in a surface profile with a calibrated height in real world coordinates. The camera used in these experiments was a Basler A622f, the camera can be triggered using an external source and so a precise frame rate can be achieved. In previous experiments using this technique (Lukaschuk, Nazarenko, McLelland, & Denissenko, 2010) a frame rate of 8 Hz was used. By changing the set up using similar equipment it was possible to increase the frame rate to 24 Hz and the expense of a slightly decreased field of view, 1.2 m to 0.945 m in order to maintain brightness of the illuminated line. The main issue surrounding this set up is achieving a high contrast image. The brightness of each pulse is reduced with pulse rate, the pulse laser in these experiments has two lasers each capable of 15 Hz pulse rate, it was possible to trigger them independently using a square wave signal 180^{o} out of phase, this meant a maximum pulse rate of 30 Hz, this was not used because there was insufficient contrast in the images to be processed consistently, the frame rate of 24 Hz produced the best balance between image contrast and still being of sufficient frequency to use the images for time dependant analysis of the surface waves.

Acquisition of the images is made using a Labview program which stores all the images on to a buffer on the computers RAM via the cameras Firewire port and then saves them to a folder on the disk drive. It is necessary to store in a buffer because of the frame rate and so there is a limitation on how many images can be gathered in one burst, on the hardware available for these experiments this limit was 3000 images of 0.5 Mp resolution.

Images are opened in MATLAB to be normalised and filtered and then using the MATLAB image toolbox the boundary between the water surface and the air can be detected. Figure shows the image after each stage of processing.

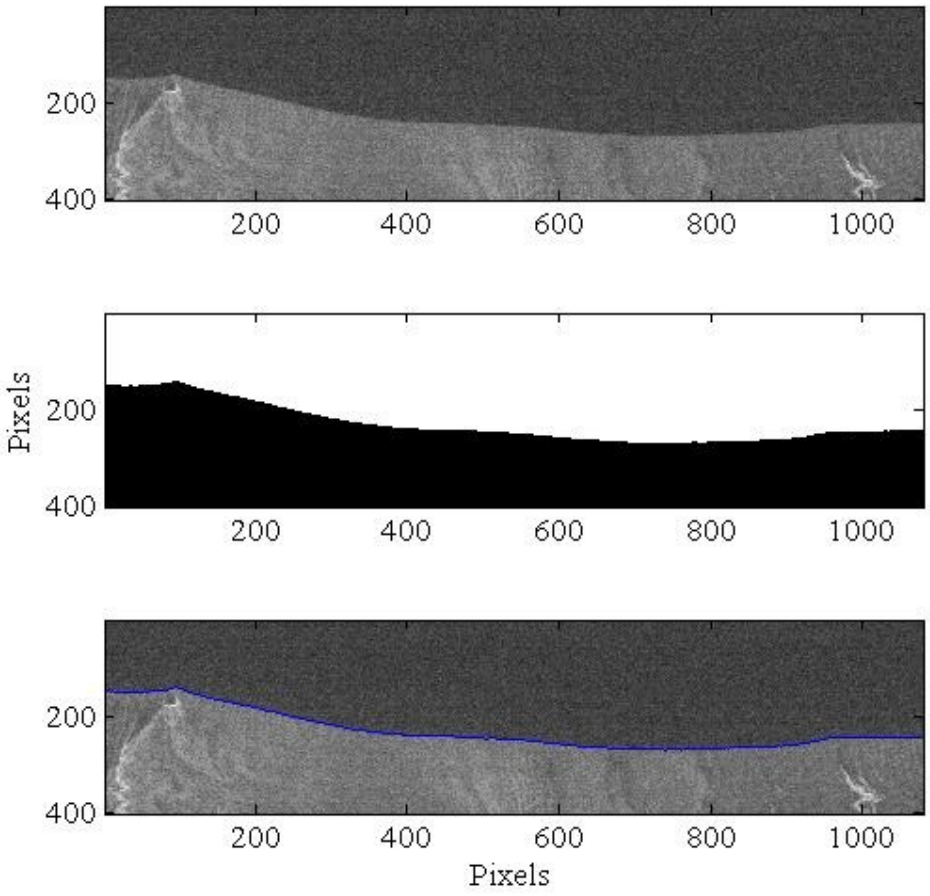

Figure 4.9 - Image Processing, Top: Original Image as captured on camera, Middle: Binary Image generated by thresholding procedure, Bottom: Detected boundary overlaid on original image

Initially the image is simply normalised and then using the 'fspecial' function a Gaussian filter is applied, this acts as a low-pass filter that removes bright spots in the image. In order to use the boundary detection capabilities in MATLAB the image also needs to be converted to a binary image; this is done by using the 'graythresh' function to find the intensity level to then convert to binary using the 'im2bw' function. At this point while a binary image now exists it may due to the gray threshold level have some holes in it, these holes are removed using the 'imfill' function to produce an image which contains two distinct halves.

The image is now prepared to detect the boundary, any under water point on the image is selected and then using the 'bwselect' any connecting pixels i.e. those of the same value can be detected. While under the water surface the function will return all four

surrounding points but once the boundary is reached it will return less. When a point on the boundary is found the function 'bwtraceboundary' is used to draw the boundary.

The data for the boundary is then saved into a text file. This means that the image data can be more easily accessed at a later date, this is useful because the process of reading the image and then detecting the boundary can be computationally expensive. Further information on all of the functions used can be found on the MathWorks website and also in the MATLAB help files (Mathworks, 2012).

4.3 Fourier Transform Profilometry for 2d Surface Reconstruction

The system presented here is based on a parallel axis geometry profilometry technique that has previously been used to measure to surface waves (Cobelli, Przadka, Petitjeans, Lagubeau, Pagneux, & Maurel, 2011).

As previously described in section 3.1 Fourier transform profilometry is used to reconstruct surface elevation from a projected pattern captured by a camera.

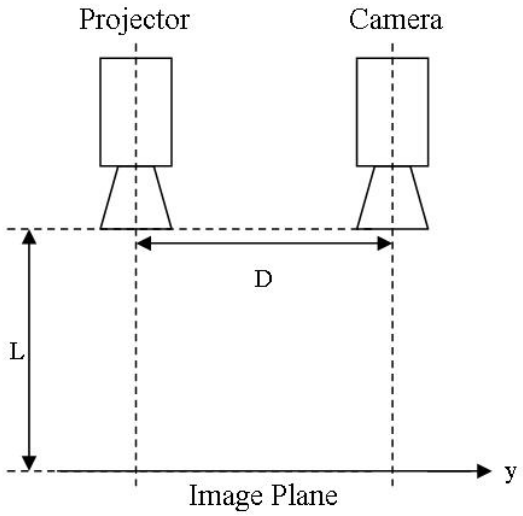

Figure 4.10 – Profilometry system configuration with parallel axes of projector and camera

A schematic of a typical setup is shown in Figure 4.10, the setup should be as precise as possible so that both the camera and projector are the same height and parallel to one another, this means that the surface can be reconstructed using only the dimensions labelled in the diagram, L the distance between the camera/projector combination and D the distance between the centre of the two lens'. Further to these geometric

considerations the period of the pattern, p must also be known. Using these variables the equation 3.1 is used to reconstruct the surface profile.

In order to process data using the Fourier transform method presented here a minimum of two images are required. A reference image, this is a flat surface with the pattern projected onto it and second image with the deformed surface that will be reconstructed; samples of these images are shown in Figure 4.11. There can be an issue with the lamp of the projector being reflected into the camera causing a bright spot in the reference image and multiple highlights in the deformed surface image as the light is scattered. To overcome this reflection polarizing filters are placed on both lenses with the same directionality.

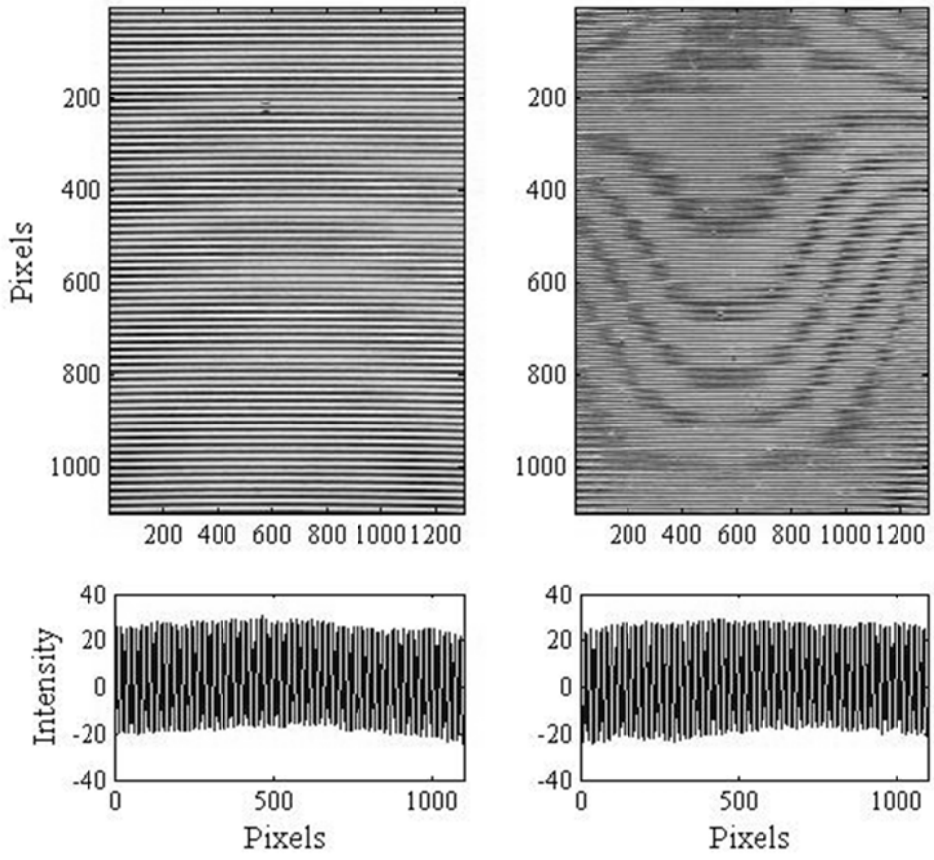

Figure 4.11 – Profilometry: Top Left: Reference image as captured by the camera. Bottom Left: Cross-section of the sine wave pattern from the reference image. Top Right: Image with deformed surface. Bottom Right: Cross-section of the sine wave pattern from the image with deformed surface.

The program used for processing the images is described in the following stages and is shown as a flow diagram in **Error! Reference source not found.**:

1. The **initial parameters** include information about the geometry (L and D), the pattern used (period p) and controls for the program such as which camera was used, colour and monochrome require different lines of code.
2. The **reference image** is read into the memory and variables are assigned to describe its size, the array is converted to a format of double and color images are changed to a 2-d array by averaging all three channels RGB.
3. **Remove bright spots** from the reference image, these are unwanted reflections from the projector illumination. In the reference image this is a single spot in the subsequent images of the deformed surface these can appear anywhere. The spots are removed by a low pass filter.
4. **Prepare reference for phase calculation**, firstly, from the reference image the fundamental frequency is found via an FFT and assigned to a variable and secondly a complex demodulation is performed on the reference image.
5. The **image of the deformed surface** is read in and processed in the same way as the reference in **step 2**.
6. **Remove bright spots in deformed surface** as per **step 3**.
7. **Prepare deformed surface image for phase calculation** as per **step 4.**
8. **Calculate phase change** by subtracting the reference from the deformed surface data, this is achieved with a multiplication of one by the complex conjugate of the other,

$$\Delta\emptyset = \mathrm{im}(\log(I.conj(R)))$$

Where, I is the demodulated image from stage 7 and R is the demodulated reference image from stage 4. The imaginary part resulting complex log is the phase, which is then calibrated to mm using equation 3.1.

9. Data from the surface is now available for analysis in space/time.

Steps 5 to 9 are performed in a loop so that a whole series of data can be processed without re-selecting new images or repeating the processing of the reference image.

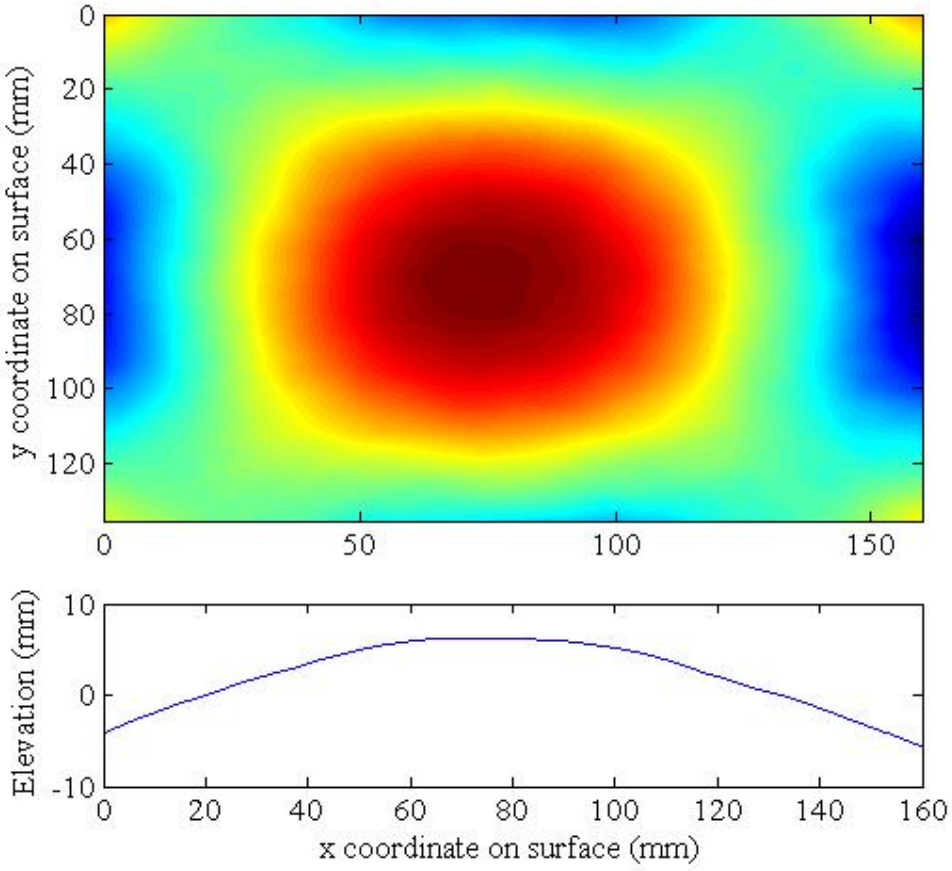

Figure 4.12 – Top: Reconstructed surface shown as a colour map. Bottom: Cross-section of the reconstructed surface taken through the middle of the horizontal coordinate.

In order to project this pattern on to a water surface particles need to be suspended in the body of water, in the experiments presented in this thesis Titanium Dioxide with typical diameter 0.6 μm was dispersed to de-ionised water at a concentration of 0.5 %

(Analysis of the size distribution is available in Appendix B). An example of a reconstructed surface from the measurement of a gravity wave is shown in Figure 4.12, the cross-section also shown is taken through horizontally through the middle of the reconstructed surface.

4.4 Accelerometers

A set of accelerometers are used to monitor experiments conducted in the laboratory like those presented in chapter 6. They can be used for static or dynamic systems although in the case of the work presented here they are only calibrated statically and then used for a dynamic system; one full rotation of the accelerometer is equal to 2 g. This simple test yields a voltage that can then be used as coefficient for calibration and is written in to a labview program so that acceleration (typically in this case of a shaker used for generating parametric waves) can be monitored live and the voltage recorded for later analysis.

4.5 Comparison of Measurement Techniques

Profile images as described in section 4.2 were used to provide evidence that the signal recorded by the PSD is entirely based upon the slope of the surface and in no way on the elevation. This comparison was motivated by observations from experiments where the refraction of the laser beam was larger than expected.

The comparison was conducted on a water surface with parametric waves generated by a shaker excited at 20 Hz. Images were recorded at 100 frames per second allowing a spectrum with a 0 – 50 Hz bandwidth to be produced, this is not sufficient to study the dissipation of the waves, however, it provides sufficient data points to compare with the PSD measurements.

Figure 4.13 shows the comparison of the two spectra where the elevation spectrum calculated from the images has been multiplied by k^2 for direct comparison.

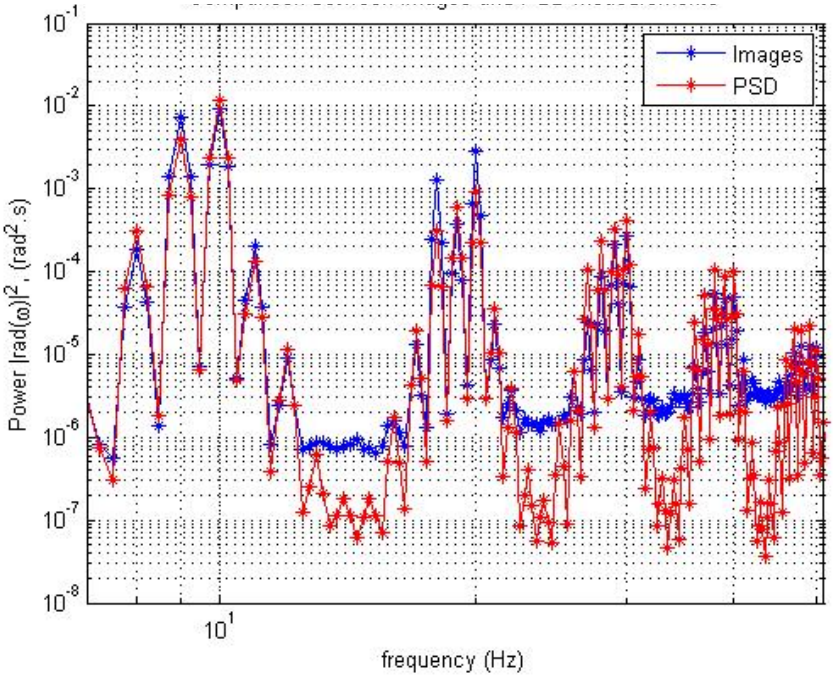

Figure 4.13 – Comparison between image profile data and PSD system data

In a general comparison the profilometry technique is the most desirable because of the complete surface reconstruction however the deployment of the technique in a large scale experiment is still not possible because of the amount of and the physical difficulties in suspending titanium dioxide in the body of water. Overcoming this difficulty is the next challenge facing the technique, in the mean time the fluorescent laser technique offers limited spatial statistics along a line which in cases where the wave regime being studied can be considered isotropic should not be an issue. If only point like measurements are required or even they are the only measurements possible due to perhaps sampling rate of available hardware or physical restraints on the experiment the PSD would be the natural choice if high frequencies are to be studied but will ultimately fail when breaks occur regularly, in this case and as an excellent way of monitoring or validating other techniques the wire probe remains a robust, versatile, tried and tested technique.

5 Large scale experiments on Gravity Waves

In this chapter experiments from the Total Environment Simulator at The Deep (Hull) are presented. Data and analysis are presented for the rise, decay and steady state of wave regimes with different amplitudes and boundary conditions.

5.0 The Total Environment Simulator

The Total Environment Simulator (TES) at The Deep (Hull) is a versatile experimental facility that consists of a large flume of size 14 m x 6 m x 1.6 m, it can be used to generate flows through channels and study bed formations and also as a wave tank in the configuration used for the experiments presented here.

The 14 m length includes an inlet and outlet for flow generation as well as an 8 panel wave maker on one end. The effective length of the tank used for surface wave experiments is 12 m. This reduction is made by the wave maker on one end and an internal wall on the other in front of the outlet. It is possible to construct other internal walls to achieve various boundary conditions, this is a feature utilised in these experiments to create a trapezoidal tank.

The facility has a moveable gantry across the 6 m dimension of the tank which can be used for mounting equipment and measurement devices and then locked in place.

5.1 Experimental Setup

Two techniques for data acquisition were used, the capacitance wire probe and fluorescent laser imaging, both described in chapter 4. Two wire probes were arranged on either end of a light sheet for the imaging and positioned in the middle of the tank attached to an aluminium frame on the gantry. The light sheet was oriented parallel to the 12 m length of the tank as shown in Figure 5.1. The camera used to capture the illuminated water surface was positioned from the ceiling with a 35 mm lens and at an angle of 30^{o}, the image is 400 x 1080 pixels with calibration x_p = 0.875 mm and y_p = 1.01 mm.

The wire probes were held in place by a clamp at the top end attaching them to a mounting point on the aluminium frame and were left free at the bottom end but with a

steel weight just above the bottom of the tank. At this depth it is assumed that there is little or no flow and so the weights would be sufficient to stop the probes from moving, in the event of a trial run and all subsequent runs of the wave maker this was indeed the case. Mounting the wire probes in this manor eliminates having any kind of frame in the water and so is less invasive than previous incarnations of the device, which could generate short waves themselves from the frame. The probes used in these experiments had resistor value of 10 kΩ.

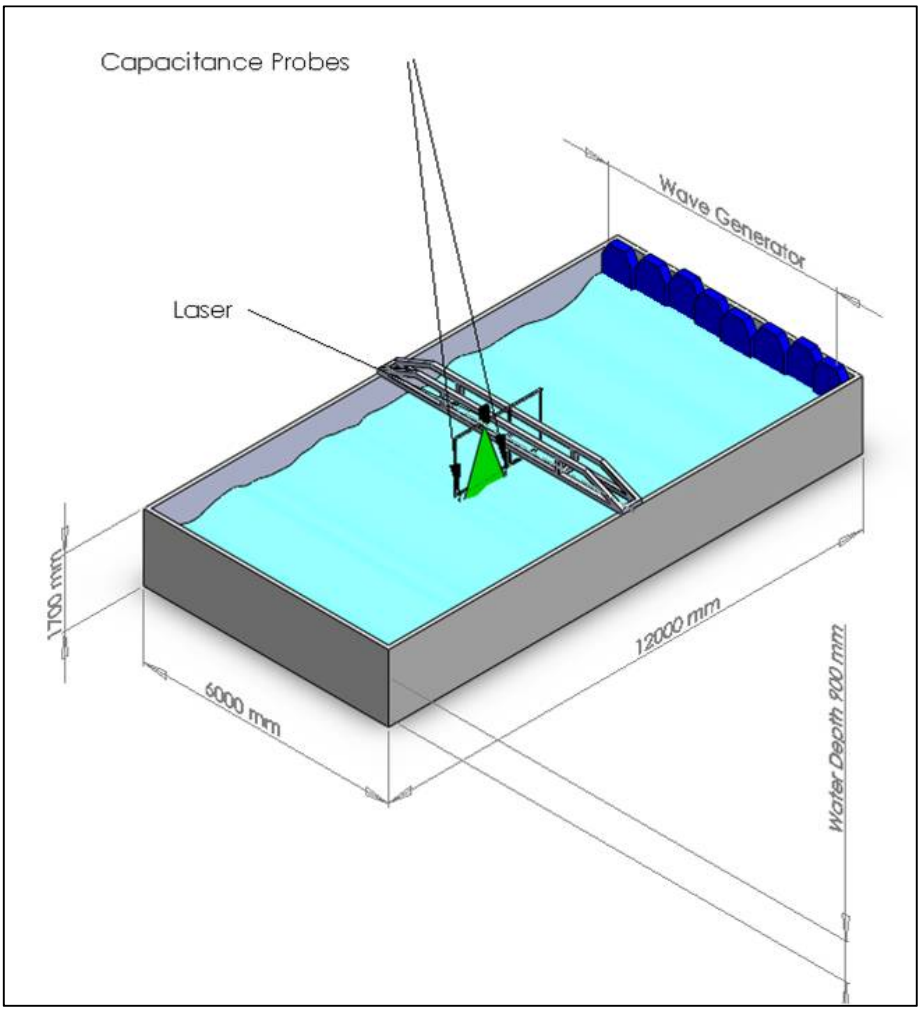

Figure 5.1 – The Deep tank and data acquisition device locations

A number of configurations were used for the generated waves all centred around 1 Hz, typically waves were generated at 0.97 Hz (λ = 1.6 m) and 1.17 Hz (λ = 1.2 m) with an angle of 9^{o} separating them. Alternatives to this type of generation were also used for comparison, these included single frequency waves generated perpendicular to the wave

maker, single waves rotated by 9° from perpendicular and a rotated version of the standard two frequency excitation, the schematic in Figure 5.2 shows the configurations.

The principal concern when selecting the configuration for the generated waves is that the spectrum of waves should be continuous. The excitation should be concentrated at low frequencies to ensure scale separation between excitation and dissipation scales. Furthermore, the excitation should create an isotropic wave field, this is achieved by multiple reflections from the tank walls; it is assumed that there is low energy dissipation and that waves reflect from the walls many times and interact in the middle of the tank.

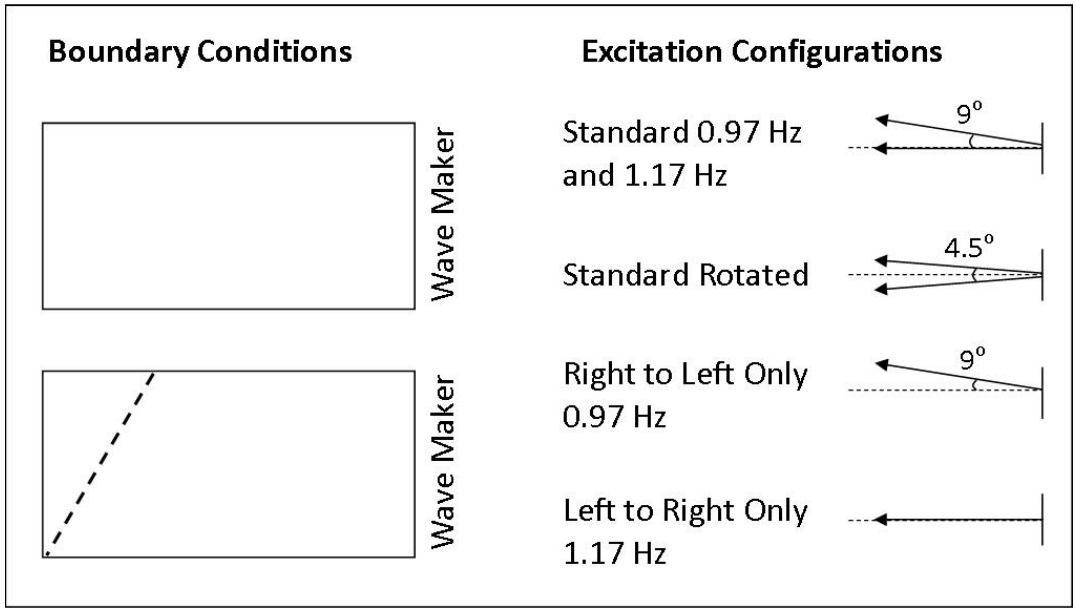

Figure 5.2 – Deep tank boundary conditions and wave maker wave generation configuration

In addition to excitation configuration the effect of boundary conditions were considered in two formats, in the first instance the full volume of the tank was used 6 m x 12 m filled to a depth 0.9 m which means the waves generated can be considered to exist on deep water since $h > 0.5\lambda$, where λ is the longest wave in the system (1.6 m from the linear dispersion relation).

In the second configuration a wall was built at 30° to the 6 m side creating a trapezoidal tank. Care was taken when preparing the walls for both the rectangular and trapezoidal

tanks that the walls were clamped firmly so as to provide a ‘solid’ wall that would not move under wave action creating additional dissipation. Figure 5.3, shows views of the facility and the setup and configuration used.

The alterations to the boundary conditions are a new development in this kind of experiment and are important because in previous experiments the observed frequency spectra have had a steeper slope than predicted by theory; this has mainly been attributed to the resonances within the finite tank. By changing the boundary conditions the number and direction of reflections will also be altered, this can have the positive effect of promoting interactions and improving the observed frequency spectra. Conversely it could have the opposite effect where steeper slopes are observed and finally it could be that there is no detectable change.

Figure 5.3 - Top Left: Boundary wall built to get the trapezoidal shape tank. Top Right: View across the tank of the gantry, the wire probes are mounted on either end of the aluminium frame and the laser guide can be seen at the top of the image. Bottom Left: The laser sheet during measurement. Bottom Right: Wave maker paddles.

5.2 Experimental Procedure

Preparation at the start of everyday includes “cleaning” the surface of the water, this is done using a plastic float with a rope through it to collect any small pieces of debris that

have gathered on the water surface. Particles on the surface can adversely affect the laser illumination as captured by the camera, although this is usually dealt with by the filter on the lense.

The capacitance probes are calibrated for use using the method described in the chapter 4. This procedure is completed at the start and end of each day, the end of the day calibration is purely precautionary in case there is a problem with the morning calibration and as a quality control for the device.

Preparation before each run is a series of checks that the filenames and folders for the data are correct and that the correct parameters on the wave maker software have been accepted. A dry run can be done on the computer to check that none of the paddles will over-extend during the sequence of pumping.

The programs running the wave maker, recording the data for the probes and the images are on three separate machines and have to be started manually when the experiment is ready to run. They are started almost simultaneously, as best the operator can manage, the delay could be no more than a few seconds; this will be shown later to be a negligible amount of time.

The schedule for data acquisition is illustrated in Figure 5.4, the whole run is split into three sections; rise, stationary and decay. The wave maker is running for the whole of the first two sections and is then switched off to allow the wave field to decay. The wire probes are recorded in three separate files for each section. The images are recorded in a continuous batch of three thousand images for the rise and the stationary sections and then as batches of 500 images with eight minutes between them for the decay.

Following each run a further thirty minutes as a minimum is waited for the surface to become flat and a new run can begin.

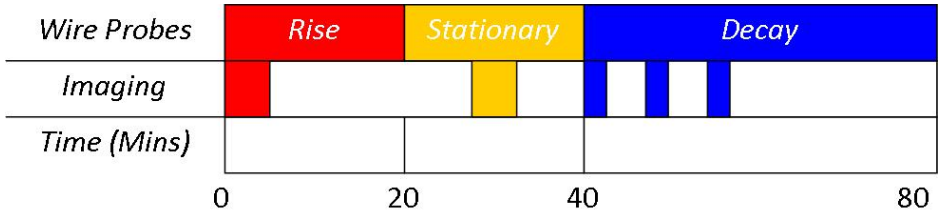

Figure 5.4 – Schedule for data acquisition

5.3 Results

The results of the experiments at the Deep are presented here in three sections corresponding with those that were indentified for data acquisition, rise, stationary and decay. The data are all processed using Matlab, where the spectra are generated using the pwelch algorithm using a hamming window, for ω spectra averaging takes place with a 50% overlap, the number of averages changes for the different acquisition types and, the wire probes enable more averaging because of their longer dataset. For k spectra there is no overlap in the averaging because each boundary has to be processed individually and the average is taken over the whole dataset, 3000 images unless stated. At high amplitude there are sometimes problems with the boundary detection caused by splashing from wave breaks, in datasets where this is the case these images are ignored and in order to calculate ω spectra the data is split into continuous sections.

An example of ω spectra calculated from sets of 3000 images with window size 64 is shown in Figure 5.5. The fitting range is chosen on an individual basis; at higher amplitudes the available range is wider. Similarly Figure 5.6 show an example of the k domain energy spectra, the fitting range here is chosen to be the same as those used for the frequency spectra by calculating wavelength from the linear dispersion relation. A further example of the ω domain energy spectra is seen in Figure 5.7 this time calculated from the wire probe data with window length 256, in this plot there is clearly a fitting range of one decade this is slightly longer than that achieved in the spectra calculated from the images this is due to the vertical resolution in the images being insufficient past ~8 Hz. An overview of the parameters and spectral slopes is presented in table 5.1.

Wave Maker Gain (A.U)	Regular (mm)	Trapezoidal (mm)	Non-linearity Regular	Non-linearity Trapezoidal	k slope Regular	k slope Trapezoidal	ω slope Regular	ω slope Trapezoidal
0.20	20	16	0.10	0.08	-3.88	-3.28	-6.67	-5.35
0.25	40	23	0.21	0.12	-3.18	-3.49	-4.29	-6.10
0.30	29	31	0.15	0.16	-3.30	-3.08	-4.79	-4.55
0.35	33	37	0.17	0.19	-3.20	-3.10	-4.49	-4.44
0.40	33	40	0.17	0.21	-2.95	-2.79	-4.43	-4.01
0.45	27	40	0.14	0.21	-3.07	-2.77	-4.80	-3.75

Table 5.1 – Experimental parameters and resulting k and ω slopes

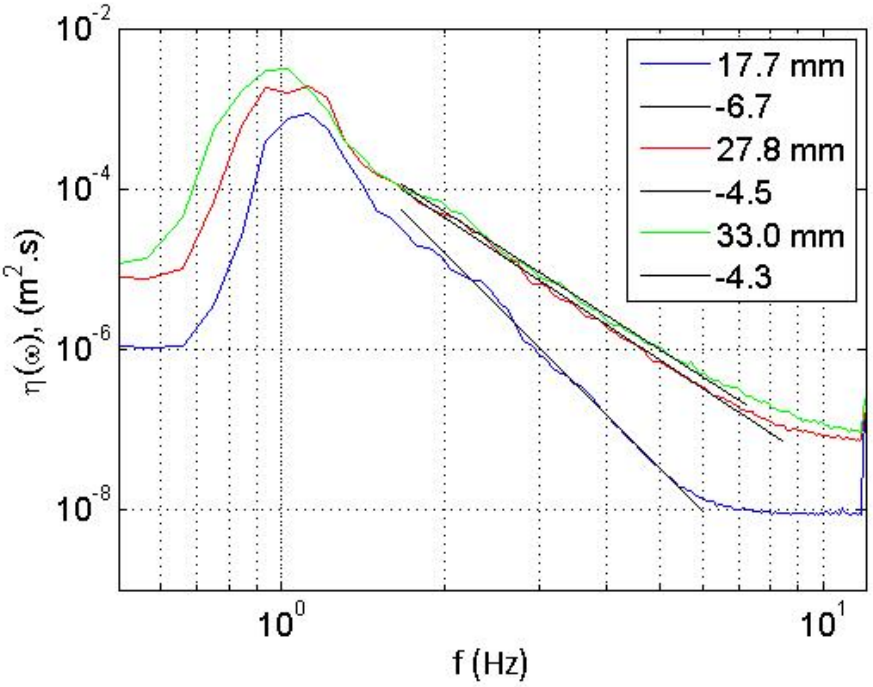

Figure 5.5 – ω spectrum calculated from image data for different amplitudes in a rectangular boundary condition, standard deviation of the wave elevation and spectral slope are shown in the legend.

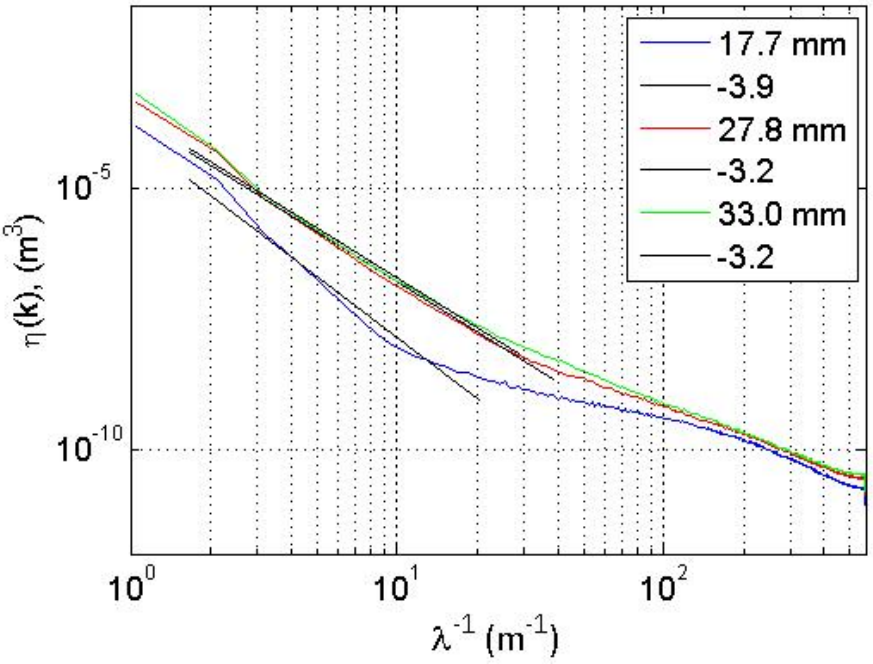

Figure 5.6 – k spectra for different amplitudes in a rectangular boundary, standard deviation of the wave elevation and spectral slope are shown in the legend.

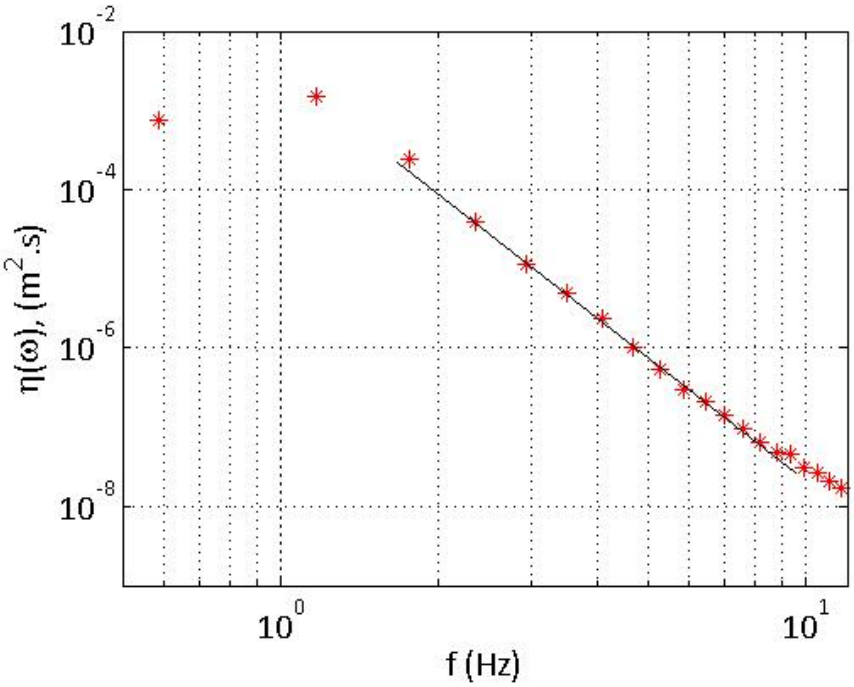

Figure 5.7 –ω spectra for moderate amplitude (γ=0.17) with rectangular boundaries calculated from wire probes

The best way to compare the spectra is by examination of the slopes of the energy spectra but for a simple visual check a spectrum from each both of the boundary conditions is presented in Figure 5.8. Both these plots are for wave fields of very similar amplitude, 33.0 mm and 32.9 mm the slopes are however slightly different and in the main peak around the excitation frequency the two pumping frequencies can be seen as discrete peaks in the trapezoidal boundary condition and as a single hump in the rectangular boundary condition, this feature in not seen exclusively in this manor but it seems far more likely that the two frequencies are distinguished in the trapezoidal condition. This difference would be worth further consideration if the feature propagated to higher frequencies but there are no harmonics visible and the spectrum is continuous.

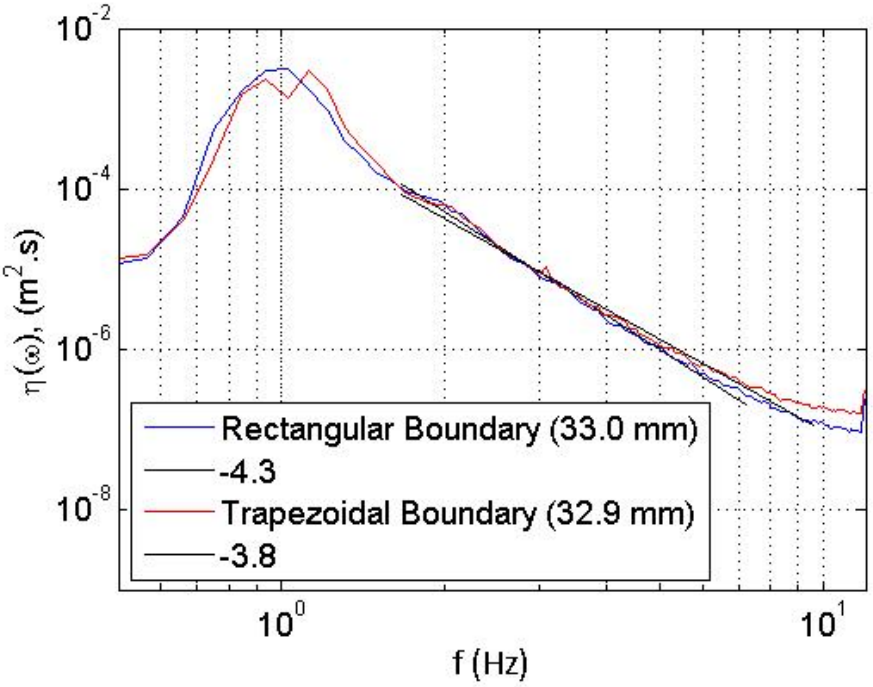

Figure 5.8 – ω spectra for comparison between regular and trapezoidal boundaries produced using image data, standard deviation of the wave elevation and spectral slope are shown in the legend

Using the calculated slopes of the frequency spectra the wire probes and images can be compared for consistency. Figure 5.9 plots the setting on the wave maker for each run against the measure slopes from wire probes and images, twelve points are considered, six from each of the boundary conditions. In general there is a reasonable agreement between the two techniques, particularly at moderate amplitude.

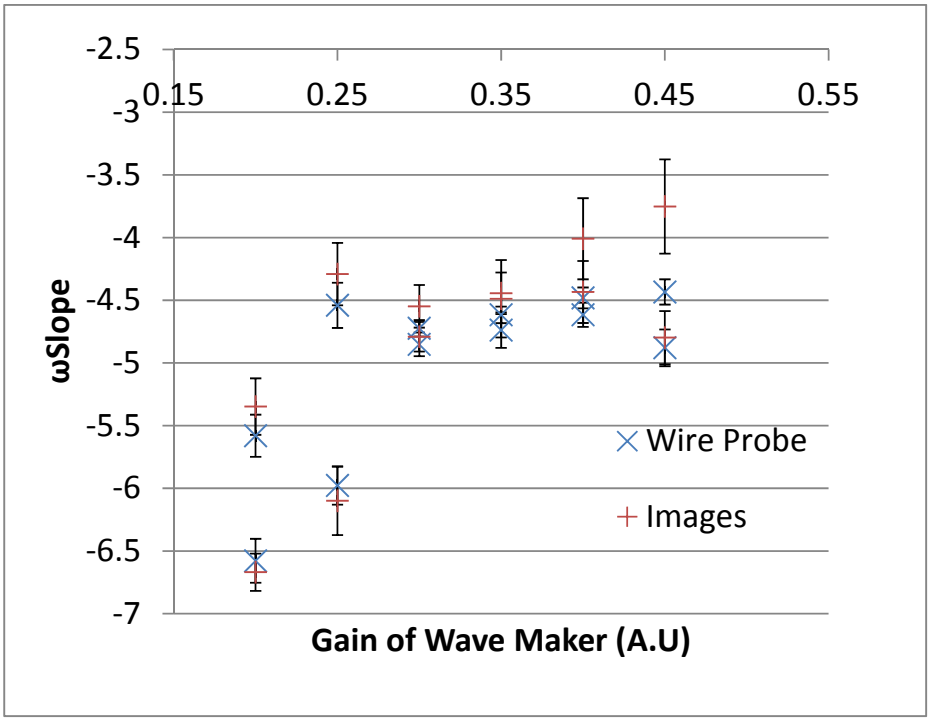

Figure 5.9 – Comparison of data acquisition techniques via ω-slope, both boundary conditions are included.

In Figure 5.10 and Figure 5.11 the measured slopes for k and ω are compared with their theoretical predictions, this also provides an opportunity to compare with previous similar experiments (Lukaschuk, Nazarenko, McLelland, & Denissenko, 2010). There is evidence of similar behaviour to previous results as expected, particularly for the trapezoidal boundary. As was previously observed the data points approach the Zakharov-Filonenko prediction however they never reach it. Across all the data points the k slope is shallower than observed previously.

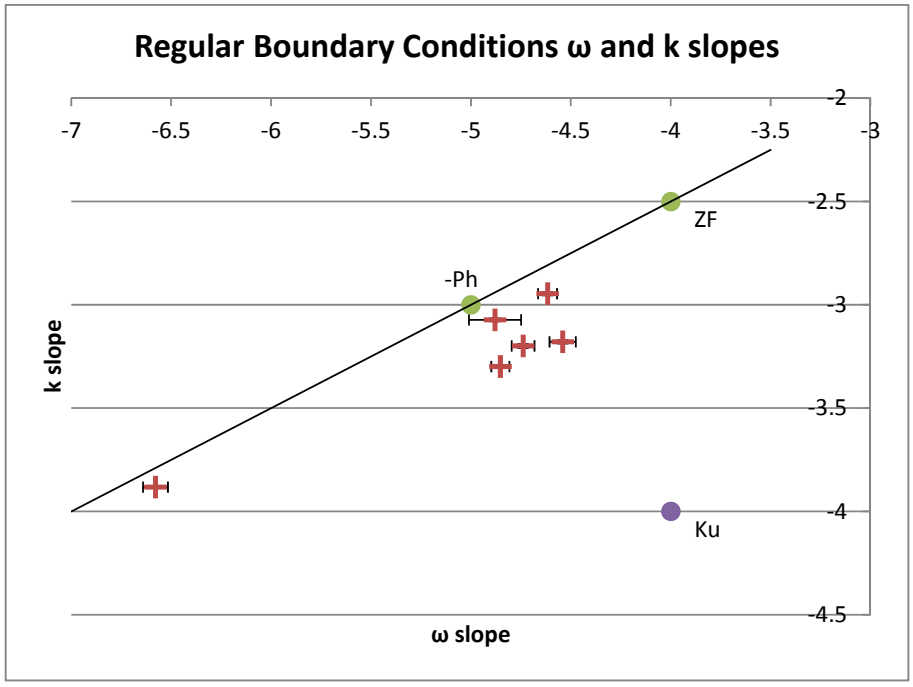

Figure 5.10 – ω and k slopes for regular boundary conditions calculated from images (k) and wire probes (ω), Ph is the Phillips prediction, ZF is the Zakharov-Filonenko prediction and Ku is the Kuznetsov prediction, the line plot is from the linear dispersion relation.

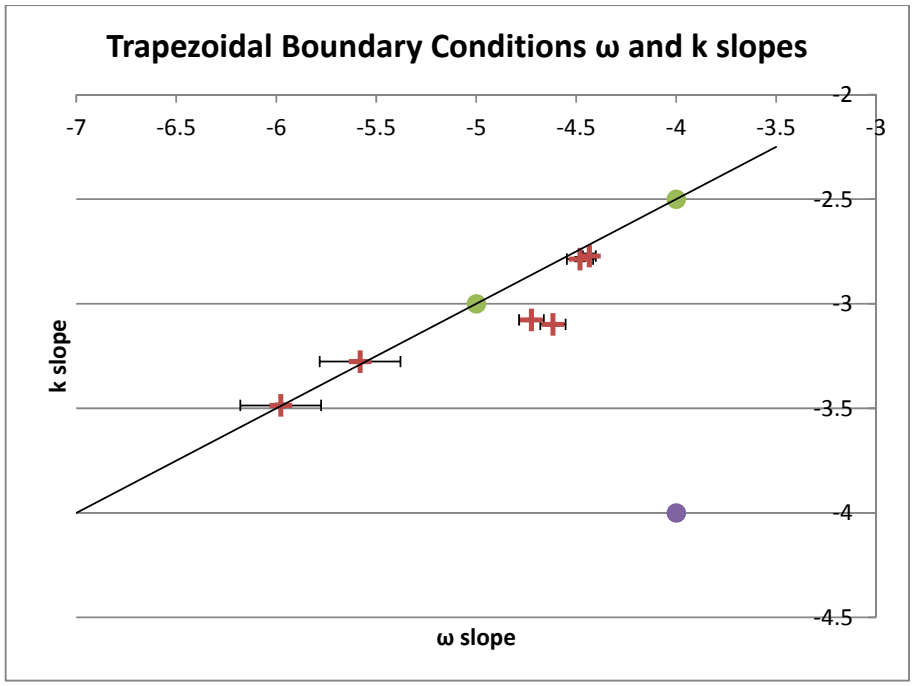

Figure 5.11 – ω and k slopes for regular boundary conditions calculated from images (k) and wire probes (ω), Ph is the Phillips prediction, ZF is the Zakharov-Filonenko prediction and Ku is the Kuznetsov prediction, the line plot is from the linear dispersion relation.

Slopes for the energy spectra in ω and k are plotted against the average energy in the spectrum at 3 Hz in Figure 5.12 and Figure 5.13 respectively. The energy at 3 Hz is taken since it is away from the excitation frequencies and can be more representative of the wave regime. The results are in good agreement with previous observations, again from (Lukaschuk, Nazarenko, McLelland, & Denissenko, 2010), with regards to the increase in the steepness of the slope as wave intensity is reduced. It is also evident from these plots that there is no discernible difference between the rectangular boundary condition and the trapezoidal boundary condition for this stationary state of the wave field. In the case of the k domain slope there is a small error associated with each point that is barely visible in some data points, this error is so small because of the long dataset allowing a great deal of averaging. In the ω spectra where the error is also relatively small a strong correlation is observed above 5 $mm^2.s$ but for waves below this intensity the data scatter is larger.

Also included on these plots are the data points for alternative wave programs and these points also lay along the same line with a strong correlation.

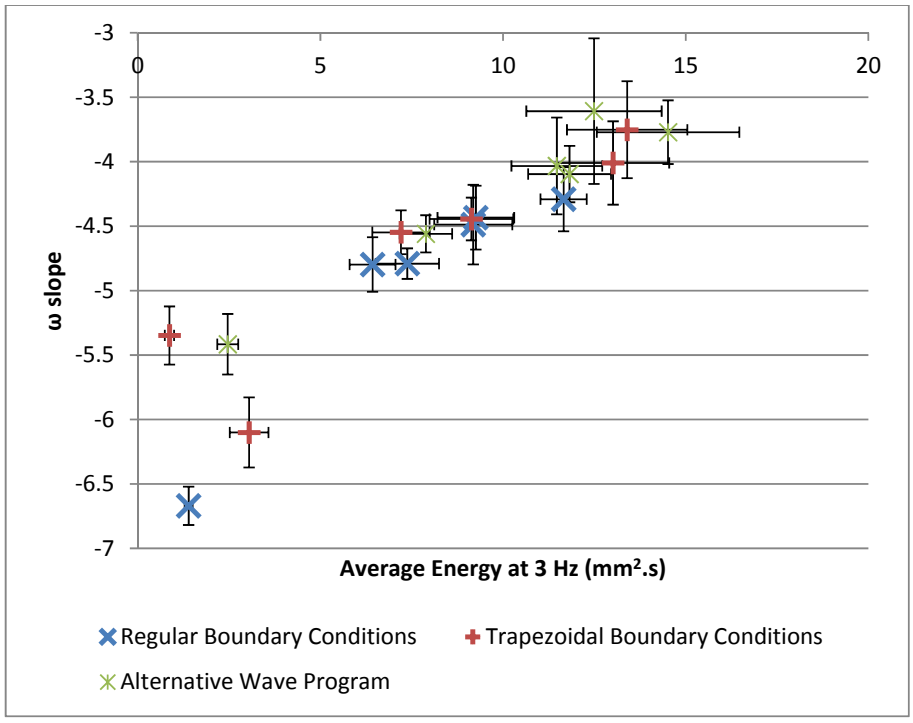

Figure 5.12 – ω slopes for both boundary conditions compared via intensity in the spectrum at 3 Hz

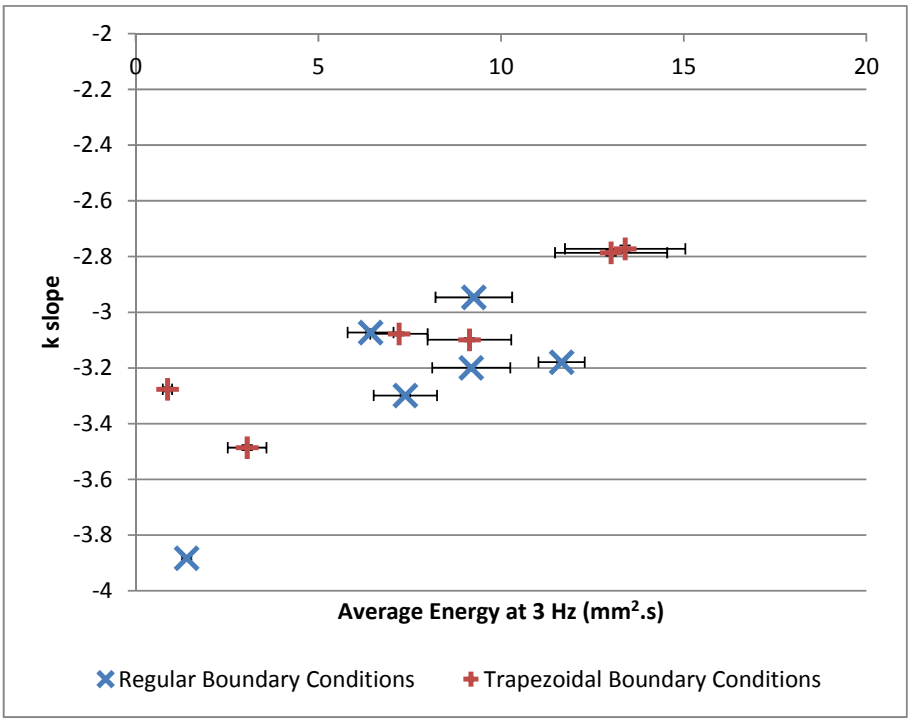

Figure 5.13 – k for both boundary conditions compared via intensity in the spectrum at 3 Hz

In order to understand why shallower slopes are observed at higher intensities the image boundaries are processed to show temporal fluctuations at different frequencies, this same method is later used in the analysis of the rise of the wave regimes. The imaging technique offers better resolution via a kind of temporal zoom. The image boundaries are processed by calculating the k spectra as before but averaged over 1 second which is equal to averaging of 24 frames, time evolution can then be observed by taking a k band from the spectra. The result of this process is shown in Figure 5.14 for a regime with moderate intensity.

The sharp peaks which are observed simultaneously across all the k bands correspond to breaking waves, during these events the k slope can be seen to become shallower.

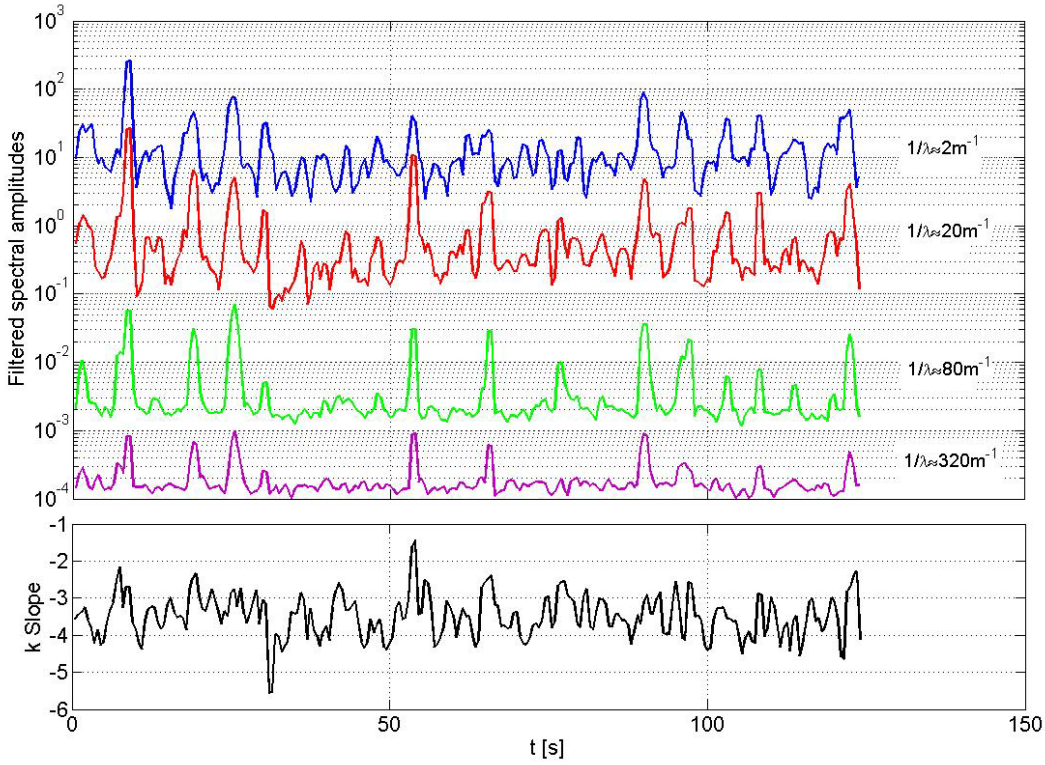

Figure 5.14 – Top: Temporal fluctuations in the k domain for k bands. Bottom: k slope as a function of time.

5.4 Wavenumber-frequency spectrum

The imaging technique that is used in this experiment allows the space-time domain spectrum to be calculated via a 2-d Fourier transform, this is presented in Figure 5.15 for high intensity waves and Figure 5.16 for low intensity; to the best of the authors knowledge these are the first such plots for large scale experiments. The linear dispersion relation is superimposed on the plot but it is not expected that we should have a ridge along this line which would ordinarily confirm the dispersion relation because the images represent data along the line and so the resulting k – ω spectrum will include waves travelling from a number of different angles to the light sheet which will be represented as different wavelengths for the same frequency. Instead what is expected and what is evident in the plot for frequencies less than 5 Hz is a "filled in" part of the spectrum where waves of different angles are represented. If different wavelengths are not represented equally for a given frequency, which seems to be the case this could be an example of anisotropy in the wave field, at frequencies near to the excitation this might be expected since the waves are generated by the wave maker

rather than interactions. In any case a further restriction at low frequencies is the length of the light sheet means that only a small number of discrete angles are observable, the wavelength may appear longer when it crosses the light sheet at some angle. The higher intensity wave regime in particular shows a strong intensity propagating at relatively long wavelengths.

The results from the previous experiments at the same facility suggested that at least for frequencies away from the excitation the wave regimes are close to isotropic; this being the case an alternative explanation to the uneven distribution of wavelengths is considered. Since the perceived anisotropy is more evident in the higher intensity regimes wave breaking is a possible source. Figure 5.17 shows two k – ω spectra generated from the same data set but for short windows in time of only 10 seconds. Underneath each the filtered spectral amplitudes are shown for 2, 3, 4, and 5 Hz generated using the same method as with the spectral fluctuations. In the plots on the left the spectral fluctuation indicate that there are no breaks here and in the k – ω spectrum the intensities are quite well filled in, though there is still evidence of anisotropy. In the plots on the right the spectral fluctuation indicates wave breaking and the k – ω spectrum is strongly directional, on this evidence it suggests the similar behaviour observed in the previous two k – ω spectra are dominated by wave breaking.

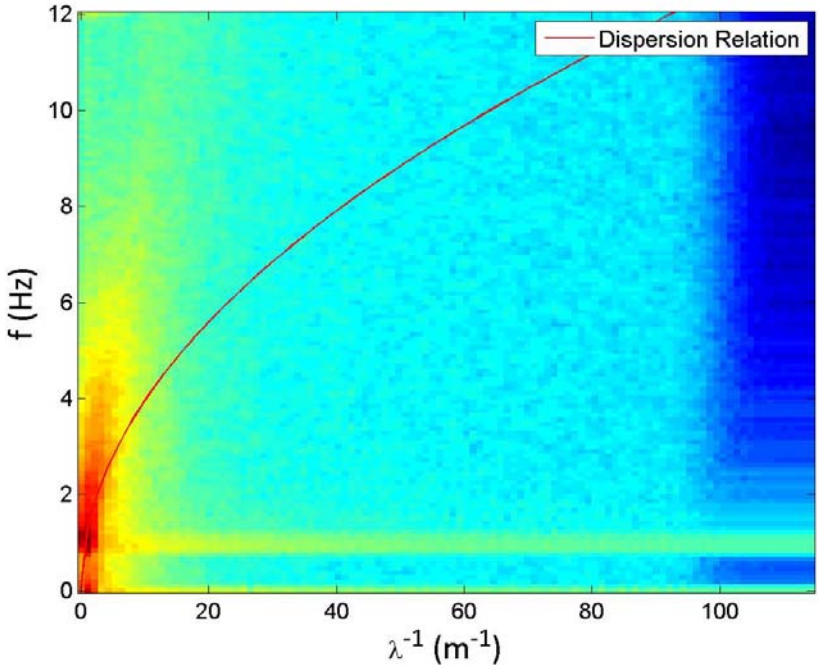

Figure 5.15 – ω – k spectrum calculated from 2-d Fourier Transform,high intensity waves ($\gamma = 0.21$)

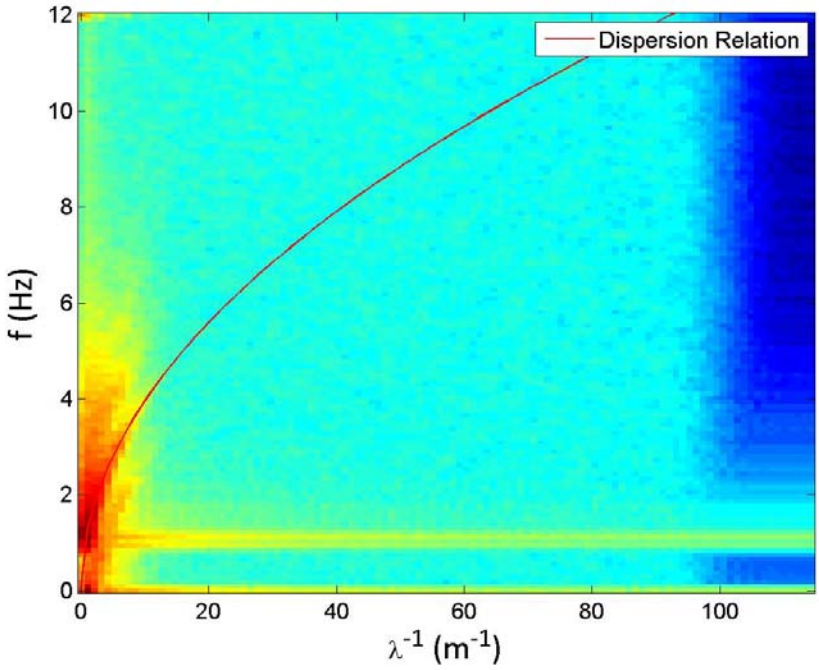

Figure 5.16 - ω – k spectrum calculated from 2-d Fourier Transform, low intensity waves ($\gamma = 0.1$)

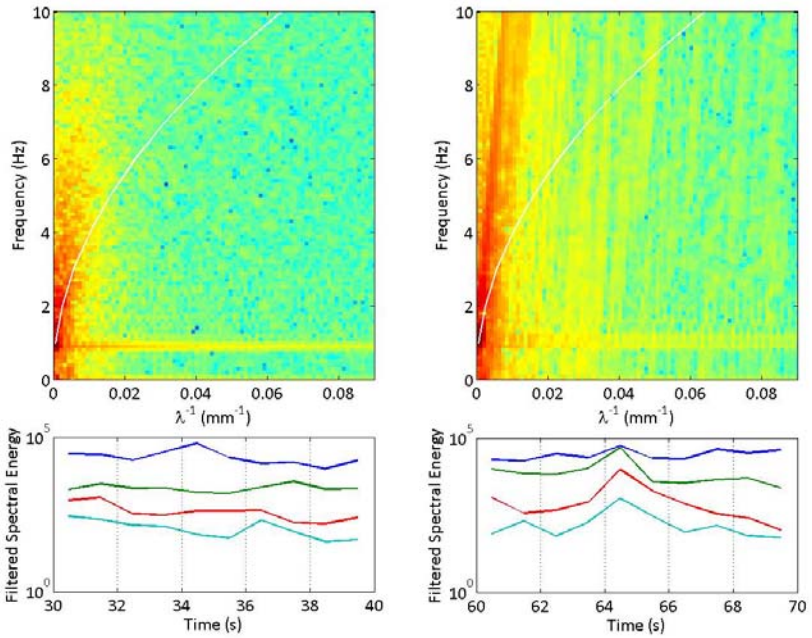

Figure 5.17 – Comparison of ω – k spectra, Left: Spectrum for when there is no wave breaking. Right: Spectrum when wave breaks.

5.5 Rise

In this section the rise to the stationary regime is presented via both the wire probes and the imaging technique. In Nazarenko, Bedard, & Lukaschuk (2013) predictions for the characteristic times for the rise to the stationary regime are presented. Considering kinetic evolution of the regime the characteristic time scale for the rise to stationary is given as $\tau_K \sim 100$ s and for dynamical evolution $\tau_D \sim 4$ s, both of these are for a wave regime with nonlinearity $\gamma \sim 0.2$.

In order to capture the characteristics of the rise from the wire probe data the wave elevation signal is filtered using band pass filters with 1 Hz bandwidth and centre frequencies of 1, 3, 5, and 7 and then short windows of 10 seconds are used to produce the plots shown in Figure 5.18. The standard deviation from the stationary regime is also indicated by the dashed lines for each of the filtered frequencies, these serve as a visual aid where the amplitude crosses this line is approximated to be the end of the rise time. This being the case it can be seen that there is a front propagation in the development where the rise time for the lowest frequency is approximately 100 seconds

which is good agreement with the kinetic equation and then higher frequencies follow with up to a 400-500 second delay at 7 Hz.

An additional feature that is observed is an overshoot where the amplitude reaches the stationary level and then decreases to rise again to the stationary level.

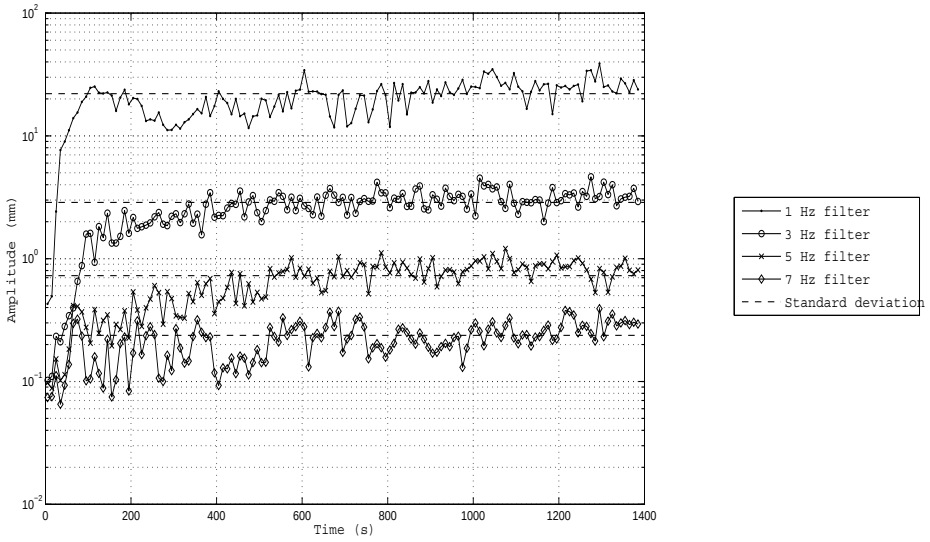

Figure 5.18 – Development of wave amplitude for filtered frequencies from wire probe data

The imaging technique offers better resolution of the rise for low frequencies via the same temporal zoom technique used to show temporal fluctuation in the stationary regime, the acquisition length is not sufficient however to observe the high frequencies with relatively long characteristic times. The result of this is shown in Figure 5.19, the propagating fronts become clearly visible for wavelengths of 50 cm and 5 cm (1.8 Hz and 5.6 Hz from dispersion relation) and a time delay between them of 20 seconds can be seen. While the full rise of the shorter wavelengths cannot be seen they are also shown because there are short periods of growth observable across all wavelengths, these can be attributed to wave breaks where many frequencies are generated simultaneously. In the data from the wire probes where the averaging is over a window 10 times longer these breaks will appear as growth which from the imaging is clearly not relevant to the characteristic rise time of 400-500 seconds which represents energy actually being transferred from the longer waves at the pumping frequency to the

shorter scales. Furthermore the breaks that are visible seem to occur approximately every 4-5 seconds, this period is not too far from the period of excitation from the wave maker and so it is possible that the excitation frequencies get in resonance with one of harmonics of the tank increasing the likelihood of wave breaking, this effect may be minimized once there is sufficient mixing from wall reflections.

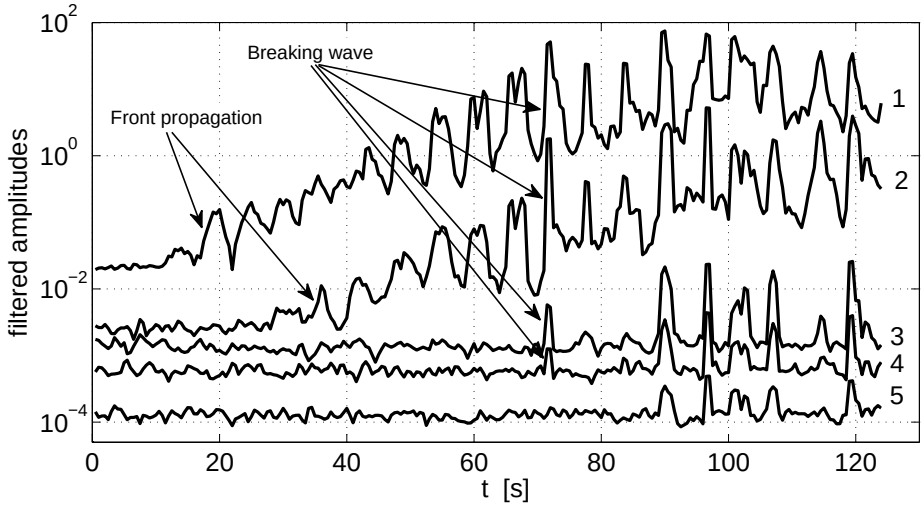

Figure 5.19 – Rise of waves from image data filtered in time highlighting front propogation and breaking events

5.6 Decay

The results presented here illustrate the decay of gravity waves when the wave maker has been stopped, the stopping procedure has a "ramp down" time of only a few seconds but because of this the exact time of the start of the decay has some uncertainty. The imaging technique is not considered here since it does not offer a long enough acquisition for the decay process to be properly observed. The length of the record for the wire probes is ~40 minutes and this is split into sections to generate ~30 points in time, each section is processed with a window length of 256 and total of 100 averages; from here we can see that the slight uncertainty in the start time of a few seconds is negligible.

Figure 5.20 shows the decay of the main peak of the ω energy spectra in the rectangular boundary tank, it is filtered for 1 Hz with a bandwidth of 0.4 Hz. Three different amplitudes are shown all of which have the same decay characteristics which can be viewed as two distinct mechanisms changing at around 500 seconds, until this time the

main mechanism is a power law which can be seen best in the inset axes, with the same results presented on double log axes. After 500 seconds the main mechanism is one of exponential decay. Nazarenko, Bedard, & Lukaschuk (2013) show that wave turbulence theory predicts a power law decay $\alpha\ t^{-1/2}$ and the second mechanism where the effects of the tank walls become dominant predicts that after 480 seconds an exponential decay should be observed and is estimated as $\sigma_v \sim 900^{-1}\ s^{-1}$.

The power law part of the plot is short but nevertheless in good agreement with the prediction as is the cross-over time which remains the same regardless of wave intensity in the stationary wave field. The exponential decay observed in the experiment is somewhat faster than that predicted by theory, measured as $\sigma_v \sim 270^{-1}\ s^{-1}$, this value is still the same order of magnitude and can perhaps be explained by enhanced dissipation in the corners of the tank.

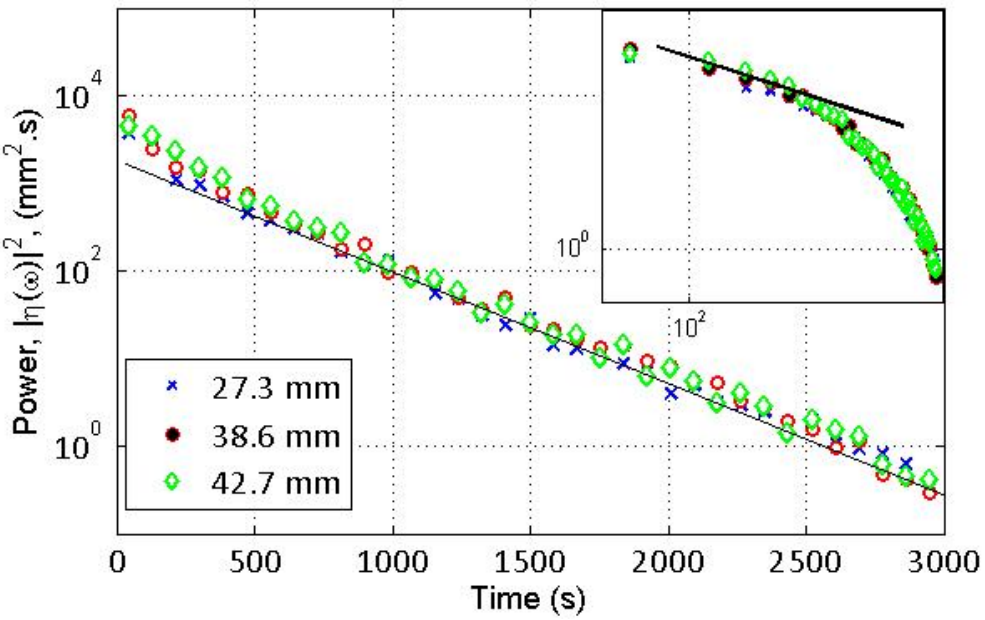

Figure 5.20 – Decay of main spectral peak for regular boundary conditions, standard deviations of wave elevation are shown in the legend

The decay of the main peak again filtered at 1 Hz for the trapezoidal boundary condition is compared with that from the rectangular flume in Figure 5.21. The characteristic times in the trapezoidal tank for both the power law and the exponential decay are faster than seen in the rectangular boundary the point at which wall interactions takes over is

also shifted in time to the left, it is difficult to estimate the power law because of the very short time frame it now exists over. This is possibly due to the trapezoidal boundary promoting resonant four wave interactions better than the rectangular boundary. The exponential decay is measured as $\sigma_v \sim 160^{-1}$ s^{-1}, this suggests a greater wall fiction possibly linked to the slightly reduced size of the tank due to the incline of the wall.

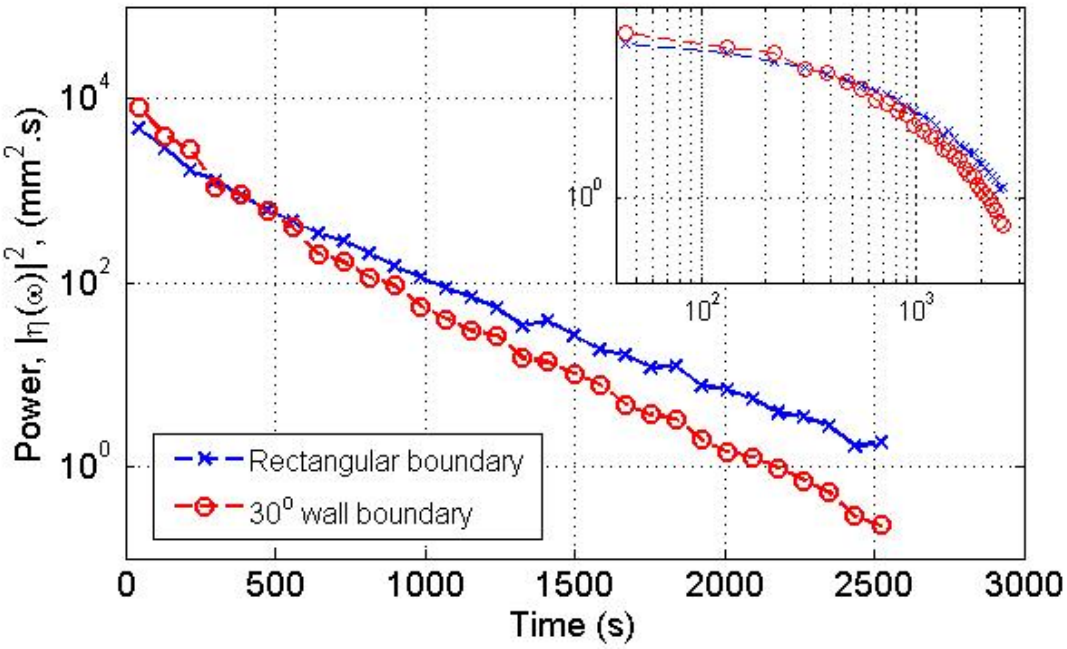

Figure 5.21 – Comparison of the decay of the main spectral peak for different boundary conditions

Given that decay due to wave interactions and decay from wall friction is so well observed in the data it would perhaps be surprising to see non-linear wave interactions remaining too far beyond the crossover point where wall friction becomes dominant, the wall friction does however act mainly on the longer energy containing waves and so it is still possible that a shorter wavelengths can interact and be observed. Indeed this appears to be the case, in Figure 5.22, a time evolution of the ω spectrum for waves with standard deviation of elevation 27.9 mm is shown, each spectrum is normalized for comparison. Long after the transition from the power law to the exponential decay the energy in the spectra begins to oscillate with a period of ~700 seconds. The oscillations appear across many frequencies but are illustrated more clearly than the image in Figure

5.23, where time signal is filtered by a band pass filter between 4 and 7 Hz, here other amplitudes of the wave intensities are also displayed. At higher amplitudes the oscillations become less apparent.

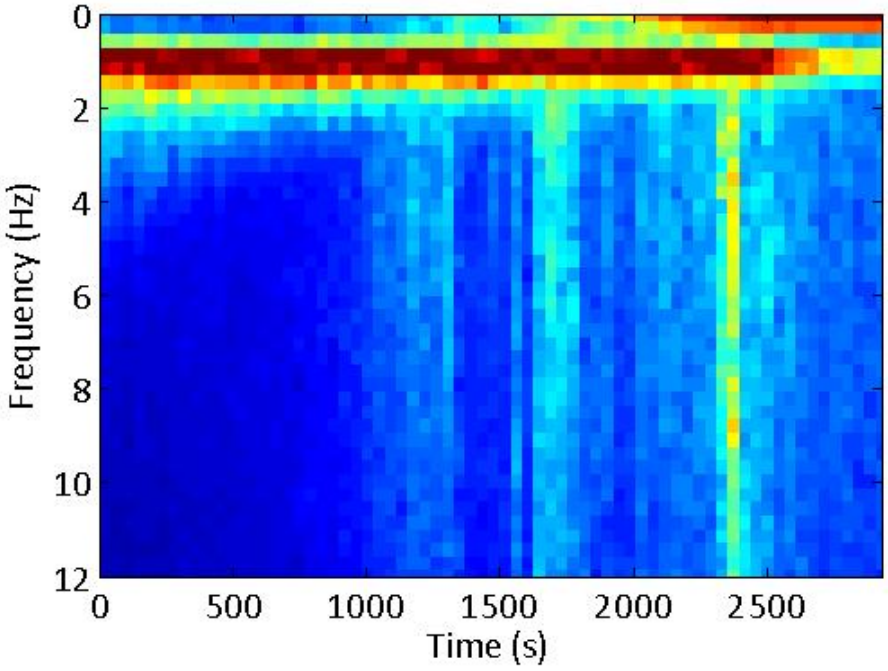

Figure 5.22 – Time evolution of normalized spectra during the decay of surface waves taken from wire probe data

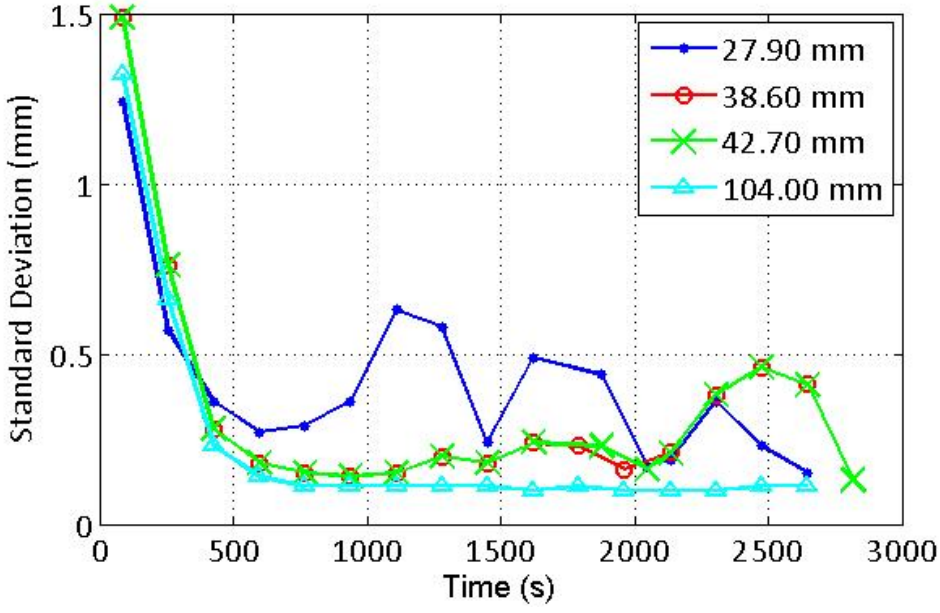

Figure 5.23 – Standard deviation of elevation for a signal filtered between 4-7 Hz during the decay of surface waves

5.7 Discussion and Conclusions

Two experimental techniques have been utilized to generate the results presented and their comparison of over 90% agreement demonstrates that in the fluorescent laser imaging technique there is a reliable non-invasive method capable of obtaining data in both the frequency and wave number domains.

The described experiment and subsequent results for the stationary wave regime are comparable with previous experiments at the same facility, this is not unsurprising but the continuity is reassuring since a number of new results have been generated.

The trial of different excitation configurations yielded comparable results and demonstrates that these is strong mixing in the tank regardless of the original direction of the excited waves, this in turn indicates that the assumption of low dissipation and multiple reflections from the walls is also a fair one.

The finite size and shape of the tank are cited as being a major contribution to why the Zakharov-Filonenko prediction is not observed in these large scale experiments, the alteration of the boundary conditions from the standard rectangular tank to the trapezoidal tank demonstrate that changing the shape of the tank does not change the observed statistics sufficiently to say that the shape is a major contributing factor. The spectra are continuous and have similar slopes, this is particularly noticeable for the frequency spectra since the error margin in these results is relatively small. The boundary conditions are shown to be important to the decay of the system since the dissipation due to wave interactions is a short interval before dissipation from wall friction takes over. This is a useful property for future experiments since it can shorten the time between runs; its practical importance might relate to harbours or other structures that ‘contain’ waves.

The ω-k spectra and the temporal fluctuations in the spectra highlight the importance of wave breaking in this type of experiment; they can be seen to dramatically change the spectrum. The increased frequency of breaks is what causes the observed decrease in the spectral slopes at higher intensities. The ω-k spectra is altered by the prevalence of wave breaks to appear as anisotropy which can be associated with the directionality of waves at the excitation frequencies.

The rise time of the wave regimes are show to be consistent with the predictions from the kinetic equation with a time of ~100 s. Similarly the decay shows good consistency with theoretical predictions in both the short time power law and long time exponential decay, despite this good agreement with the decay of the main spectral peak of energy there is the additional observation of the fluctuations at higher frequencies, these are attributed to trapped harmonics which can transfer energy to higher frequencies. The transfer of energy appears to be close to periodic and the characteristic seems to be more easily observable at lower initial intensity of the stationary regime.

In summary, new results are presented for the whole lifetime of the experiment including the rise, stationary and decay regimes. There is still much knowledge to be developed from experiments like this one but there is good agreement with theoretical predictions regarding the rise time of the regimes and the decay rate for two mechanisms of decay, power law and exponential decay. For the stationary part of the wave regimes the spectral slopes do not coincide with theoretical values however similar trends to previous experiments are observed. Additionally, there is a good agreement between the two systems for data acquisition and the results are comparable.

6 Observation of a Low Frequency Mode in a Vertically Oscillating Elastic Container

The experiments presented in this chapter were all conducted in the Fluid Dynamics Laboratory at the University of Hull. The initial aim of the experiments was to observe a low frequency mode generated by the inverse cascade of water waves. In eventuality the experiments led to the observation of a low frequency mode whose existence could indeed be an inverse cascade or alternatively by resonant conditions of the wave tank used, the observation is to the best of the author's knowledge the first under the conditions of the experiment.

6.0 Experimental Setup

The setup consisted of a square tank 42 x 42 x 25 cm made of polycarbonate 1 cm thick, this tank was secured to an aluminium frame that was mounted on an electromagnetic shaker allowing vertical oscillation of the tank. In the bottom of the tank there was a small glass window approximately 1 cm^2 which allowed the laser for the PSD technique to be used; in the original configuration of the setup the laser could be used through the polycarbonate base but subsequent cleaning of the tank meant the surface was poor quality for optical techniques and so the window was added, the glass could be cleaned and if necessary replaced which means the transmission of the laser is always good.

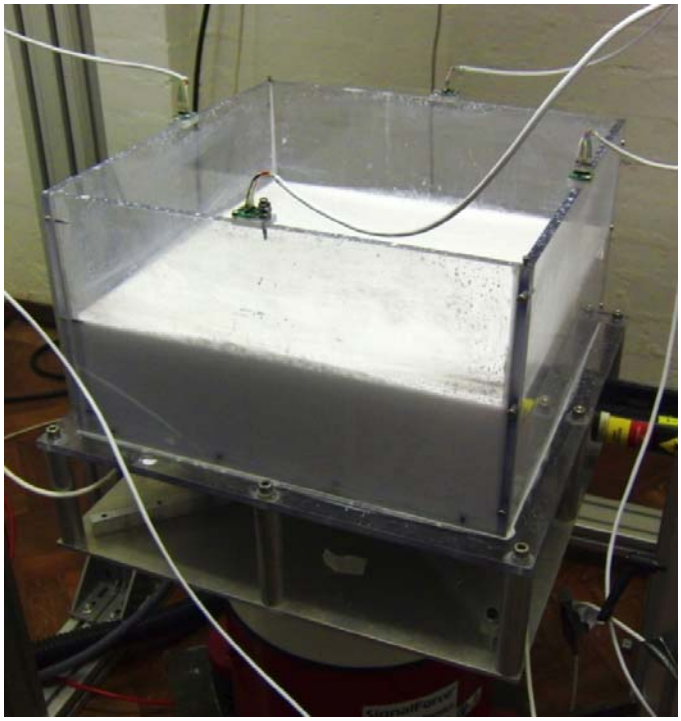

Figure 6.1 – Polycarbonate tank mounted on the shaker, the accelerometers can be seen attached at the top of each wall.

The shaker itself was levelled manually by 3 adjustable rubber feet and then isolated by an air cushion whose pressure can be increased dependant on the load of the shaker. LED indicators on the shaker alert to any problem with the isolation and so this could be monitored easily.

A series of 3-d accelerometers were mounted on the tank at the top middle of each wall and on the base of the tank, these can be seen in Figure 6.1. Typical water depths are in the range 10 – 15 cm.

6.1 Visual Observations

In a usual situation with this experimental setup parametric waves appear at half the frequency of excitation when some threshold amplitude is crossed, these waves form domains that slowly oscillate and nothing is observed at low frequencies. Nevertheless, at frequencies exceeding 50 Hz sometimes high amplitude low frequency wave will appear, in general (the most commonly observed) this wave has a frequency ~2 Hz. Which is close to, although slightly less than the corresponding wavelength related to

the tank geometry $d = 42\ cm$ is the horizontal side of the tank, $k_x = k_y = 2\pi/d$, the frequency corresponding to this value given by the dispersion relation is

$$\omega^2 = g\sqrt{k_x^2 + k_y^2} \approx 9.81\sqrt{2}\frac{2\pi}{L} \approx 203\ s^{-2}$$

$$f = \frac{2\pi}{\omega} \approx 2.3\ Hz$$

A difference between the experimentally measured frequency and calculated frequency can be explained by the boundary conditions. The observed wavelength is longer than the length of the tank wall; the wave has a significant amplitude at the wall of the tank, in the region of a third of the maximum amplitude which appeared in the centre of the tank. In this case zero boundary conditions could not be applied.

The water surface appeared different in different areas of the tank under conditions where the low frequency wave was observed, these areas are placed into zones in Figure 6.2. In zone A close to the wall waves were seen to be generated with wavenumber vector parallel to the wall, the intensity was less at the ends and corners of the wall. Droplets can be generated near the middle of each wall in a kind of fountain like those described by the dragon wash basin. Zone B represents the area where droplets and waves generated from the wall propagate. In zone C waves appeared to be generated parametrically as normal by oscillations of the tank; note that in later experiments at higher frequencies this zone appears to have no waves generated in this way.

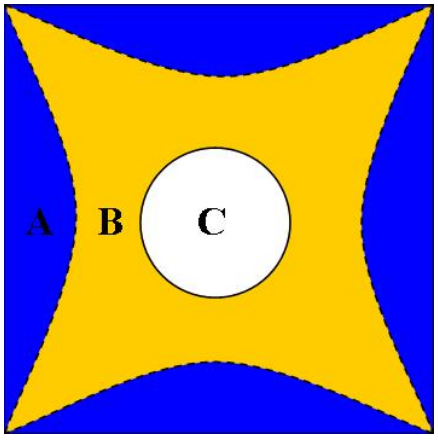

Figure 6.2 – Observation zones: A – Waves exist perpendicular to walls, B waves and droplets from wall propogate into this region, C – Parametric waves generated

It seems that waves generated at the walls are caused by vibration of the sides of the tank where their bending mode is in resonant with the vertical excitation frequency, this also explains why the intensity of the waves is less in the corners since the walls are fixed to each other and displacement of the wall is less. The primary importance of this is that the low frequency mode is not generated without this kind of excitation from the walls.

An estimation of the stream speed away from the wall can be made by filming a low density (0.9 g/cm^3) polyethylene ball on the surface. From this video the stream speed was found to be ≈3 cm^{-1}, additionally, in the centre of the tank a circular flow was indentified with a speed ≈1 cm^{-1}.

Although it was possible to make some initial measurements of the low frequency wave (described in the following section), its appearance was not very repeatable and it was and still is to some extent unclear as to what conditions the low frequency wave would appear.

6.2 Initial Observations Using PSD

A He-Ne laser was setup parallel with the base of the tank and using a first surface mirror at 45^o reflected through the window in the base through to the PSD and lens combination; the lens has a 4 cm focal length. A second lens with 0.5 m focal length is placed between the laser and the mirror to focus the beam onto the undisturbed surface, this means that the spot on the surface is as small as possible so that maximum resolution is achieved.

Figure 6.3 shows the spectra for the x and y components of the PSD signal, this observation was made at 59 Hz excitation of the shaker. The parametric waves at half the excitation frequency are as expected at 29.5 Hz but to the left of this in the range of gravity waves two distinct gradients are visible and the peak at 2 Hz indicated the low frequency wave that is visible by eye. The repeatability of this result was mixed, in a single session of measurements it could be found consistently but after some break it would be difficult to reproduce. Figure 6.4 shows seemingly the same conditions but with no low frequency mode, this picture looks similar to that observed by Snouck, Westra, & van de Water (2009) from a similar setup with a circular tank and surface gradient measurements.

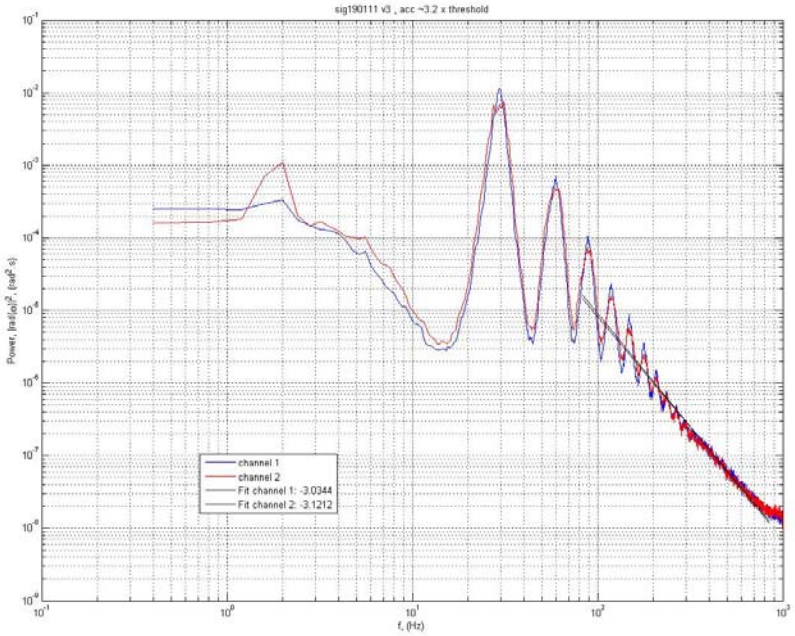

Figure 6.3 – Power spectra calculated from surface gradient measurements using PSD measurements showing low frequency mode

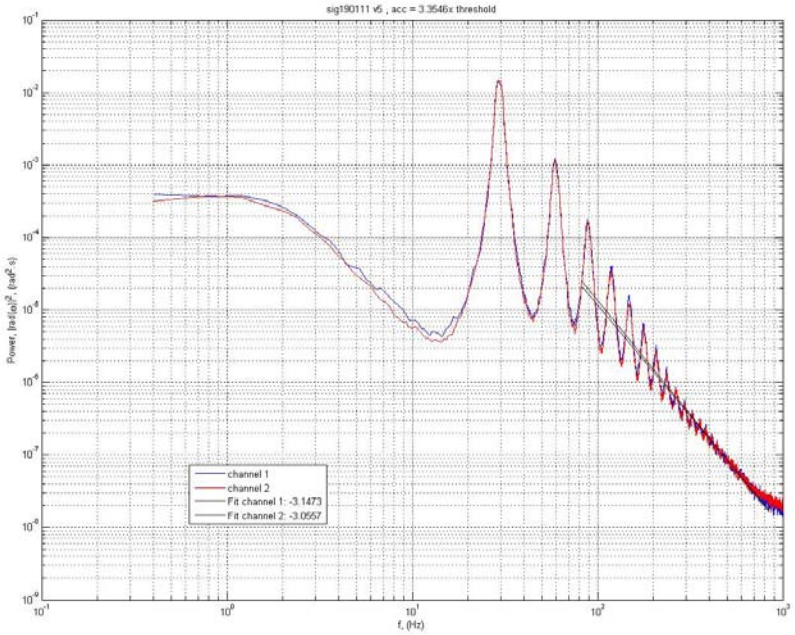

Figure 6.4 - Power spectra calculated from surface gradient measurements when no low frequency mode appears for comparison with Figure 6.3

At this stage in the experiments there were two main problems with the observation and measurement of the low frequency wave, the first being the repeatability of the observation and the second is the measurement technique; due to large refraction angle the light beam being measured was beyond the limit of the area of the sensor. The results from the PSD should only be considered qualitatively because of this. Figure 6.5, demonstrates the clipping seen on the PSD signal. Even in a case where the PSD has no issue with clipping a point like measurement is not really sufficient to characterise the observations in this experiment because the surface appears very different in various parts of the tank.

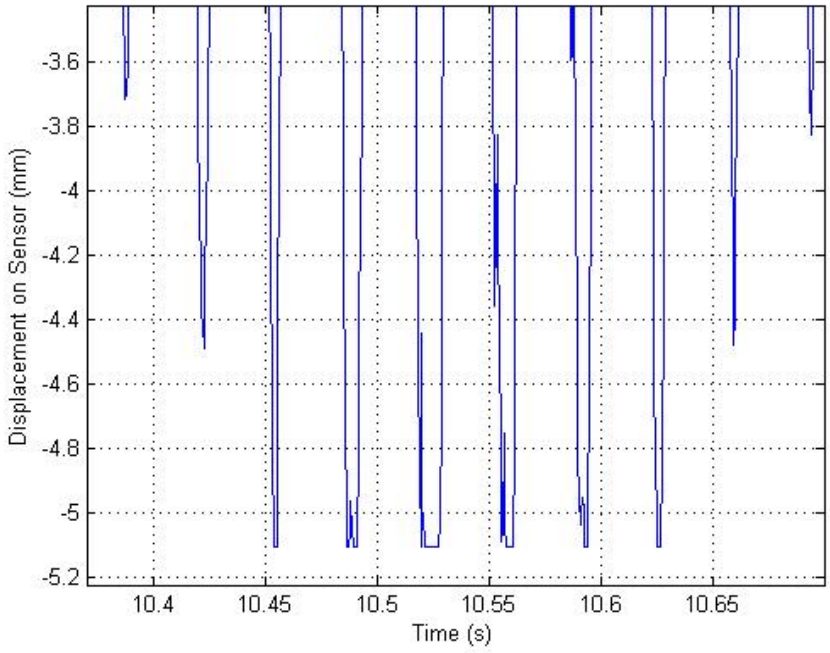

Figure 6.5 – Issues with PSD measurement, example of clipping seen on PSD signal

6.3 Resonance of tank

Since the excitation of waves near the walls as observed in initial experiments is notable as one of the features that make the appearance of the low frequency mode different from the normal case of parametrically excited waves. To understand the parameters of the experiment the resonance of the tank walls is considered.

The resonance of the tank can be found by forcing the shaker using a slow linear frequency sweep and recording the signal from at least one accelerometer mounted on the top edge of the wall on the tank and the vertical component of an accelerometer on the base of the tank. The result can be presented as a resonance curve, typically this is presented from 0.25 to 100 Hz covering the usual range of frequencies that can be observed in the tank, the sweep rate is 0.001 Hz so that the whole process takes a little over 15 mins (this is the slowest possible on the signal generator). The signal from the accelerometer has 3 components, X, Y and Z, where X is the acceleration in the direction perpendicular to the wall, Y is the acceleration parallel to the wall and Z is the vertical acceleration.

The processing of the accelerometer signals resulting from this sweep is done using a fast Fourier transform with a short window in time of 2 s: From the Z component of the accelerometer on the base the position and value of the maximum is taken at each position in time so that at the end of the process two 1d arrays are available, one contains the frequency of excitation and the other contains the amplitude of acceleration at that frequency. From the X, Y and Z components of the wall mounted accelerometer the maximums are taken, these can then be plotted against the corresponding excitation frequencies from the base measurements.

There is a trade off between the length of the Fourier transform and the sweep frequency; the values used give a resolution of 0.2 Hz. In order to make each resonance curve comparable the same voltage signal is used throughout. This signal amplitude is chosen low enough so that there are no parametric waves generated throughout the sweep.

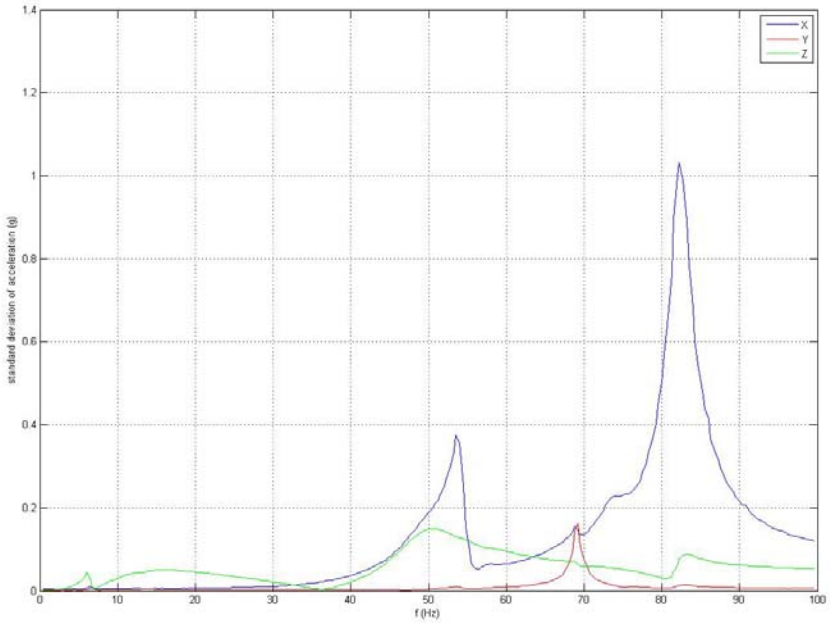

Figure 6.6- Tank resonance curve where Depth - 12.5 cm, tank filled with Water and Titanium Dioxide (0. 5%), X = Perpendicular to the wall, Y = Parallel to the wall, Z = Vertical

The example resonance curve in Figure 6.6 is for the cell filled to a depth of 12.5 cm and shows a strong and relatively broad peak at 82 Hz with a second peak approximately 3 times less amplitude at 54 Hz for the X component of acceleration, the other components are always significantly less than the main peak in X.

For an empty tank the resonance curve is shown in Figure 6.7, the main peak for X component is found to be at 88 Hz with the secondary peak at 79 Hz. Amplitude of the peaks here is higher than in the previous example due to the decreased damping that the water would normally provide.

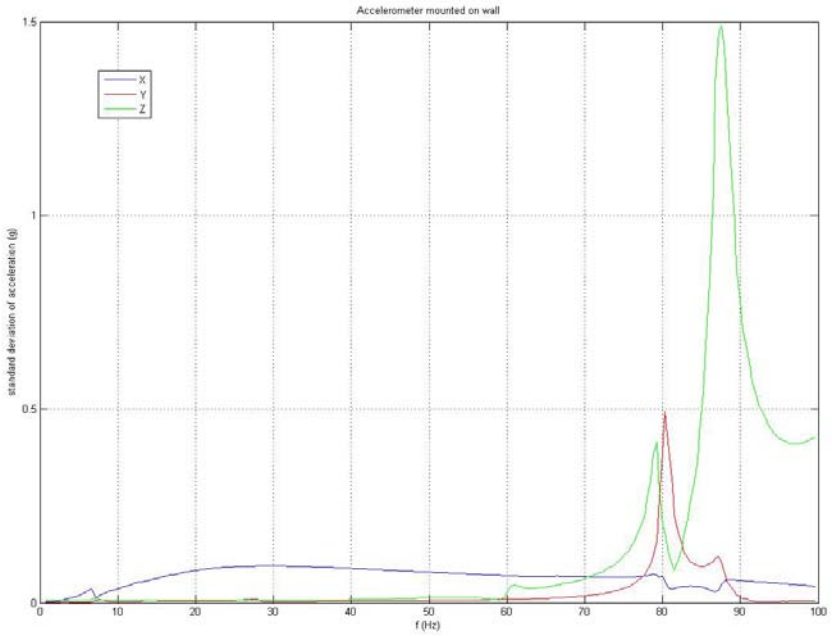

Figure 6.7- Resonance curve for an empty tank, X = Perpendicular to the wall, Y = Parallel to the wall, Z = Vertical

A comparison of the X component resonance curves for different water depths is shown in Figure 6.8, the main peak can be seen to shift to the left as the water depth and hence the damping increases. The change in the position of resonance is rather large, 3.3 Hz/cm in the range of water depths used. This means that for the depth of water measured by a ruler the variation in the resonance peak will be ±0.115 Hz. This is not insignificant but it would not seem to explain the difficulty in repeating the observations made with the PSD, in initial observations the excitation was slightly higher than the secondary peak in the mid 50s where the resonance is relatively low so in subsequent experiments the excitation was moved to be in the 80s corresponding to the main peaks in the resonance curves. Additionally main peaks have strongly differing maximums and this does not appear to have any pattern, this further highlights the apparent complexity of this system.

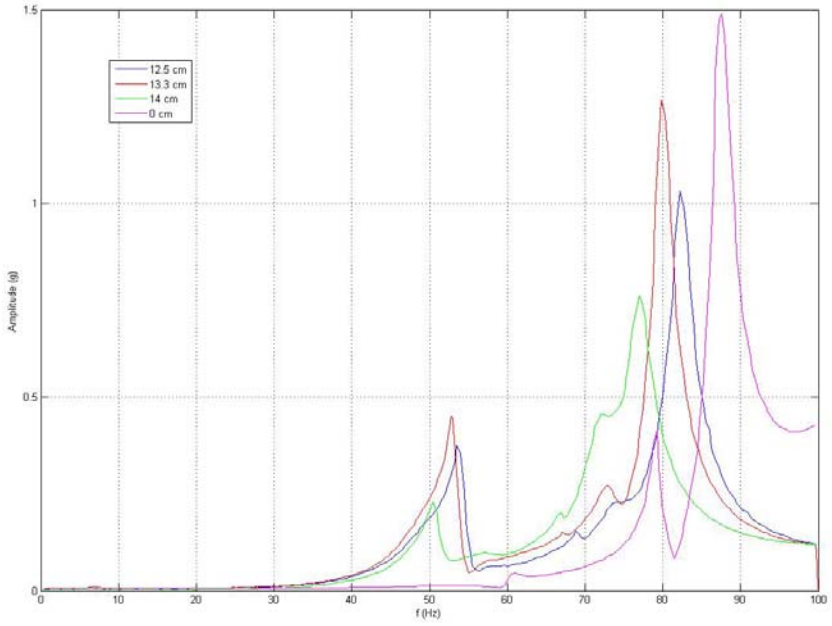

Figure 6.8 – Resonance curves at different liquid depths using acceleration component perpendicular to the wall, tank filled with water and titanium dioxide (0.5 %).

6.4 Further Investigation Using FTP

The results from the PSD have two issues, outlined earlier, the first relates to the clipping of the signal, the second is that the system is complex and waves are visibly different at the edges, corners and centre of the tank and so the point like measurement is not suitable. The profilometry techniques address both of these flaws of the PSD data but with the trade off that the sampling frequency is reduced.

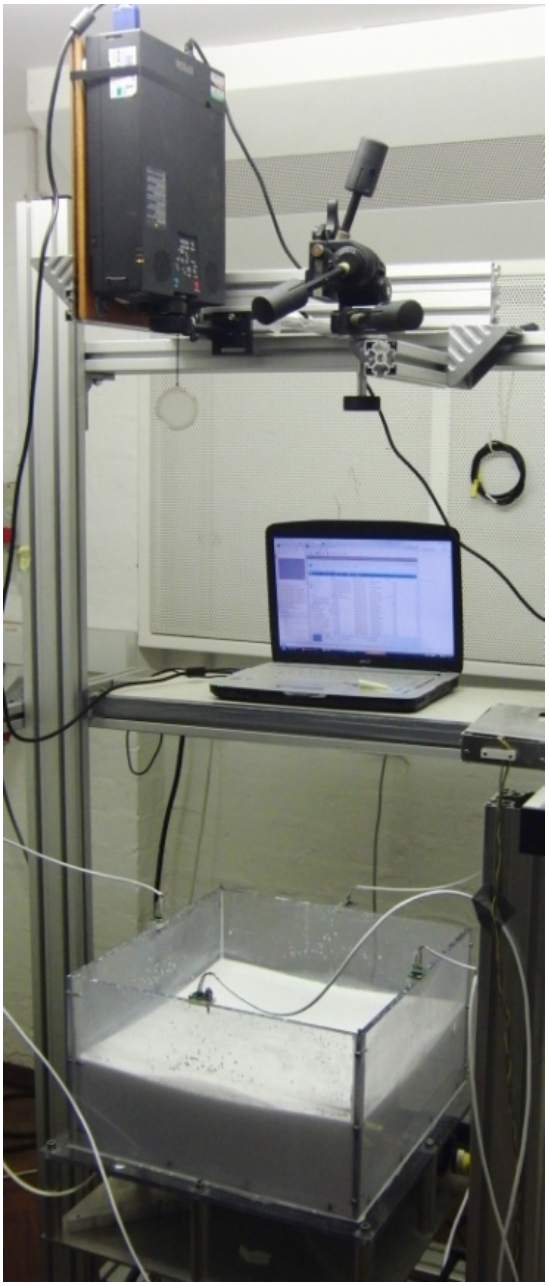

Figure 6.9 – System with profilometry rig in place.

The setup for the profilometry measurements can be seen in Figure 6.9 and is described more fully in chapter 4. The majority of results presented are gathered used a Basler camera, a number of additional results were gathered using a high speed camera kindly loaned by Dantec Dynamics.

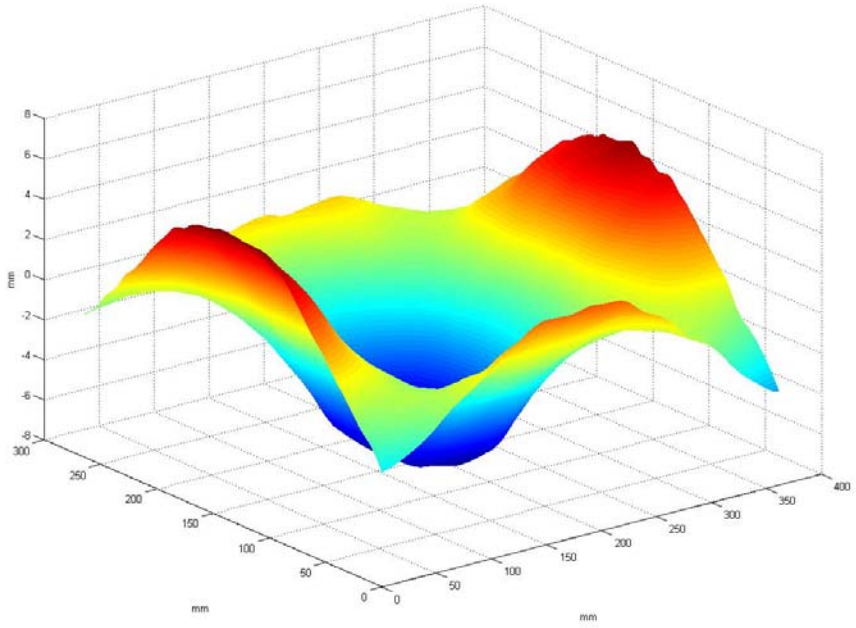

Figure 6.10 – Wave profile of low frequency mode reconstructed from profilometry. Setup parameters were L = 1 m, D = 0.2 m and pattern period p = 3.6 mm.

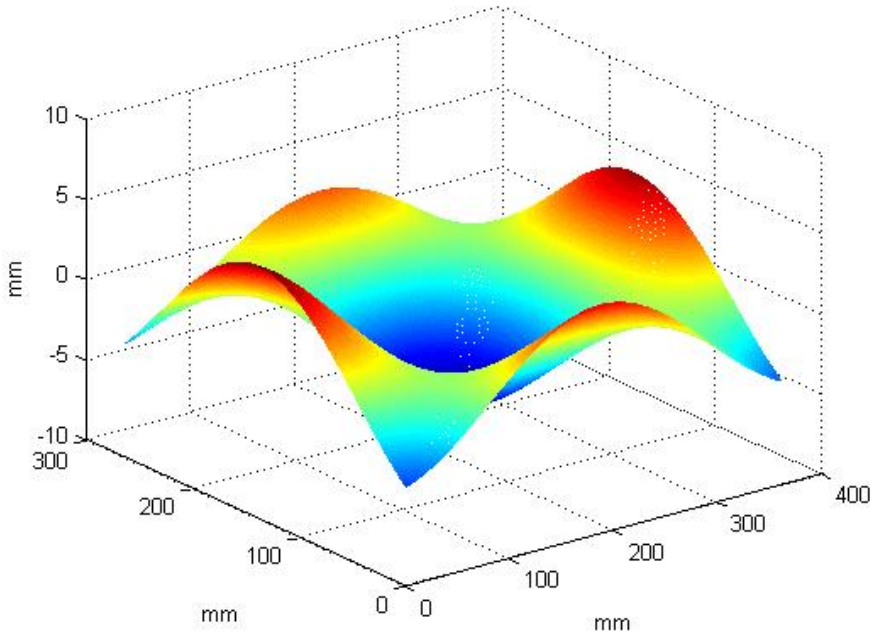

Figure 6.11 – Manual fitting of wave profile from Figure 6.10

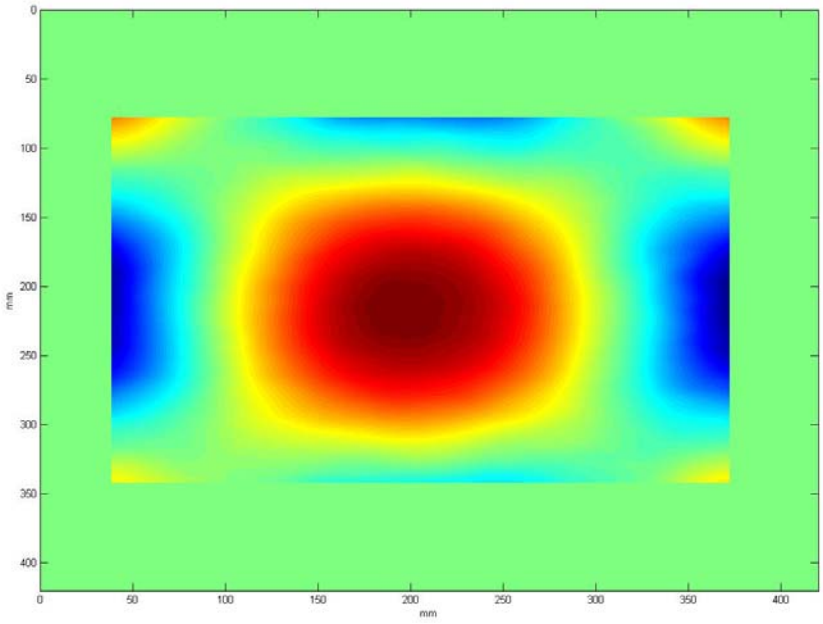

Figure 6.12 – Location of the reconstructed profile within the tank.

An example of the low frequency wave reconstructed from the profilometry technique is shown in Figure 6.10, its location within the tank is shown in Figure 6.12. The shaker excitation used was 82 Hz, approximately matching the resonance of the tank walls at 12.5 cm depth. Assessing the wavenumber of the low frequency mode $k(k_x,k_y)$ by fitting the wave to the equation;

$$\zeta(x,y) = A\cos(k_x x + \phi_x) * \cos(k_y y + \phi_y)$$

Where $k_x = 0.15\ cm^{-1}$ and $k_y = 0.17\ cm^{-1}$, A, $\square_x$ and $\square_y$ are all constant. The result of the fitting is a reconstructed surface shown in Figure 6.11. The length of the tank walls $d = 42\ cm$ and so one of the lowest resonant modes of the tank is $^{2\pi}/_{d} = 0.15\ cm^{-1}$ which is approximately the same as the fitted wave, assuming the lowest mode has wavelength $2d$ the low frequency wave relates to the second harmonic along each side (2,2). The frequency corresponding to the observed wavenumber based on the dispersion relation is approximately 2.3 Hz.

The frequency spectrum of the acceleration component perpendicular to the side wall was obtained from one of the accelerometers mounted on the tank wall; this result is

presented in Figure 6.13. The maximum in the spectrum at $F = 82\ Hz$ corresponds to the excitation frequency; several satellites can also be seen. There is also a peak at $f = 2.3$ Hz which coincides with the low frequency surface wave. The satellite harmonics closest to the excitation frequency are at $F - f$ and $F + f$.

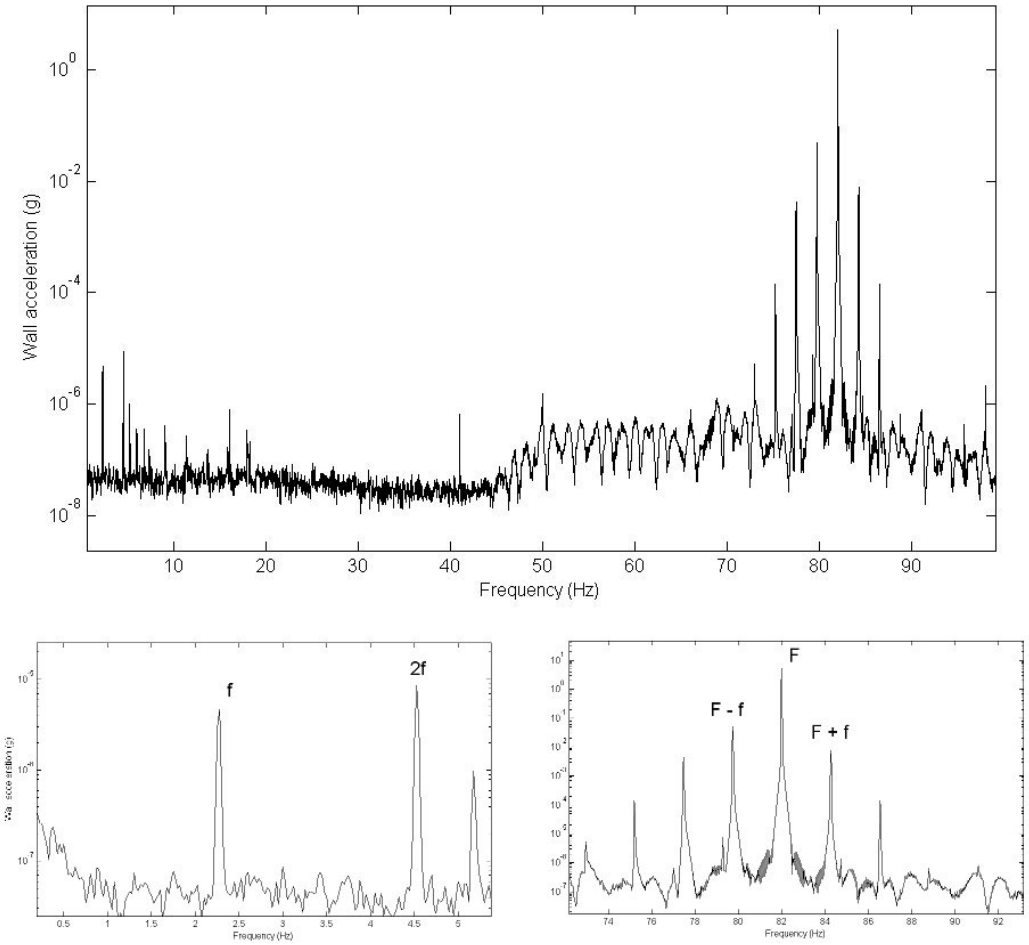

Figure 6.13 – Top: Spectrum of accelerometer signal perpendicular to wall. Bottom Left: Close-up of low frequency part of spectrum. Bottom Right: Close up of high frequency part of spectrum.

The low frequency wave is consistently excited within a short range close to the main resonance peak of the side wall. The threshold for the appearance of the low frequency wave is found manually by running repeated experiments at decreasing amplitudes until the wave is no longer generated, the observed result is presented in Figure 6.14. The resonant frequency for this result was 79.75 Hz and so the low frequency wave is generated most easily at frequencies slightly higher than this.

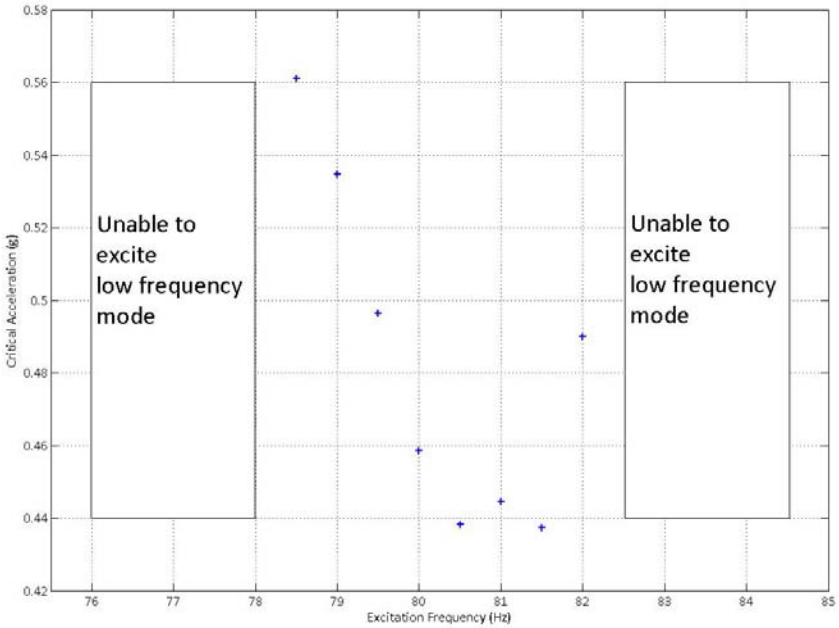

Figure 6.14 – Stability Curve for the low frequency wave.

Interestingly the low frequency mode can exist at different frequencies also corresponding to resonant conditions; this is depicted in Figure 6.15. The low frequency appears to exist at 2.3 Hz as already observed, 2.7 Hz which relates to a one dimensional wave with resonant mode (4,0) and both waves may exist simultaneously.

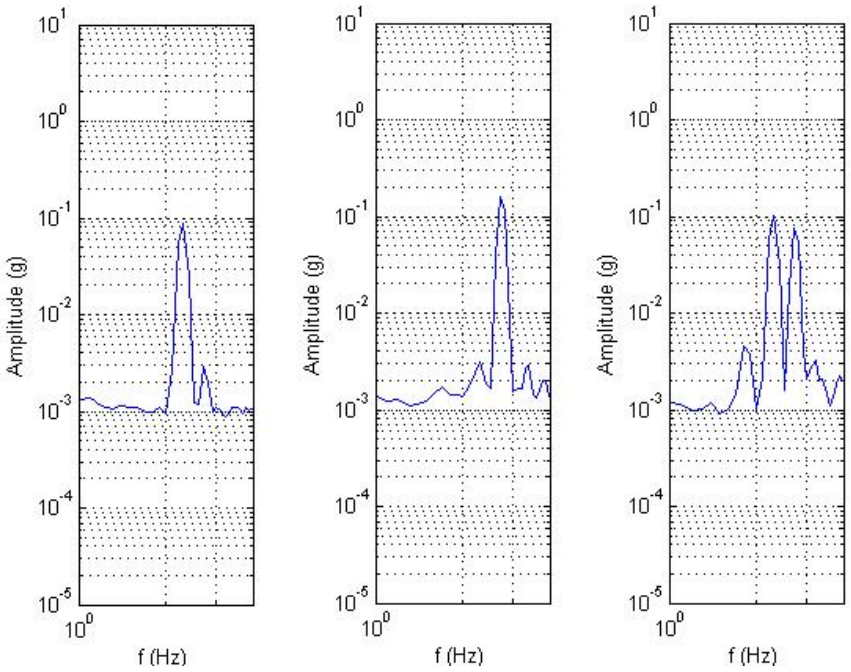

Figure 6.15 – Spectrums calculated from the accelerometer signal perpendicular to wall to demonstrate different frequencies of the gravity wave including two low frequencies coexisting.

Using a high speed camera it is possible to view the frequency spectrum of the wave elevation to include the excitation frequency, parametric mode and the low frequency wave. The frame rate used was 200 fps, the depth was 12.5 cm, the resonance was measure to be 85.75 Hz and excitation of the shaker was at 86 Hz. The resulting spectra are shown in figures. Frequency spectra are shown for a position close to the wall and a position in the centre of the tank, these spectra are averaged over a number of points and processed using the pwelch algorithm with averaging length 5 seconds and 50% overlap. Near the wall the excitation frequency can be seen as a single peak and there in a broad hump around the parametric frequency range, the low frequency mode at 2.3 Hz is also visible. In the centre an additional high frequency peak is seen at ~80 Hz, the 2.3 Hz wave is visible and a two slopes extend away from this through the gravity and gravity-capillary range, these are relatively short fitting ranges, with slopes ~1.5 and ~3.5 as shown in the plot.

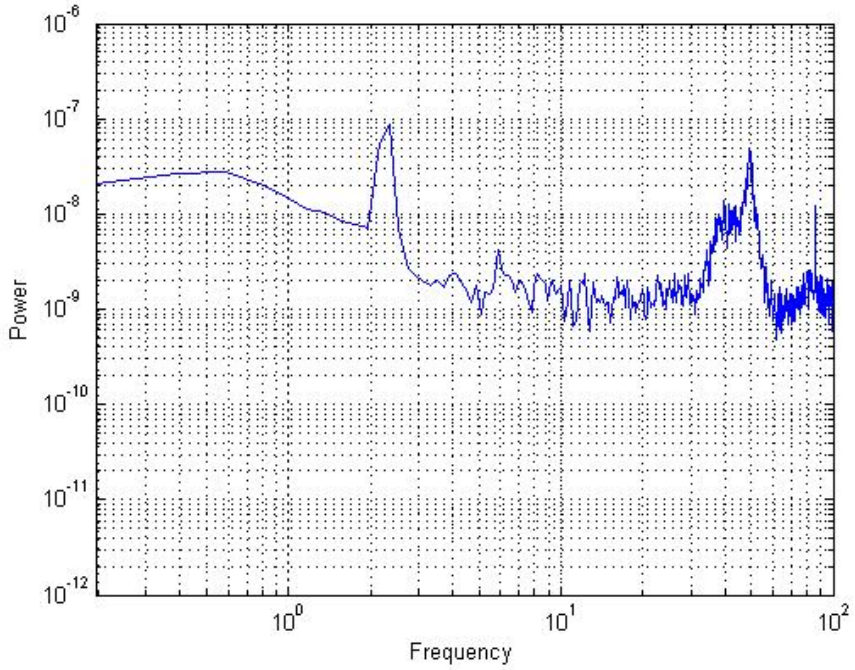

Figure 6.16 – Frequency spectrum calculated from high speed profilometry for a point near the wall of the tank.

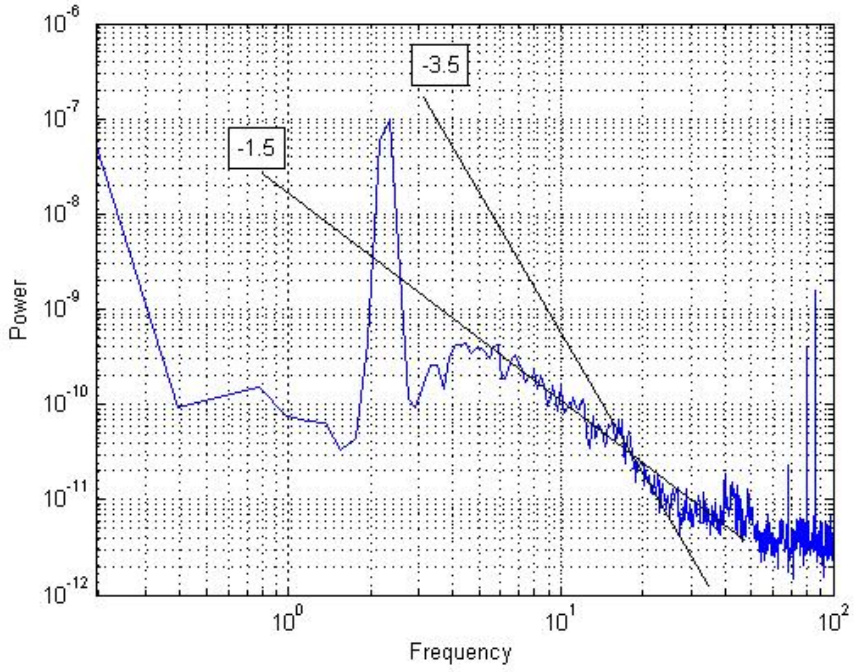

Figure 6.17 – Frequency spectrum calculated from high speed profilometry for a point near the middle of the tank. Slopes shown for illustration only.

Use of the high-speed camera allows a k-ω spectrum to be produced by the 2-d Fourier transform, this is shown in Figure 6.18. The red line shows the linear dispersion relation which is in clear agreement with the experimental result and also with the findings of Chekroun, et al. (2012), there are no harmonics relating to a non-linear dispersion relation like those observed by Herbert, Mordant, & Falcon, (2010).

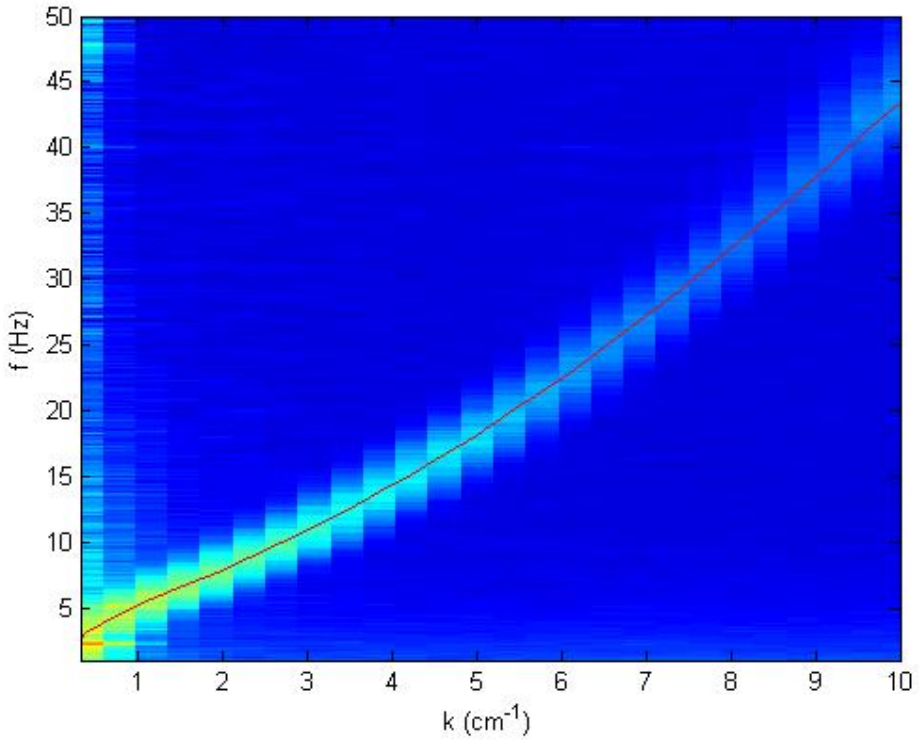

Figure 6.18 – Frequency – wavenumber spectrum demonstrating the linear dispersion relation found using high speed profilometry

6.5 Discussion

There are three proposed explanations for the observation of a low frequency mode in this experiment, these are the Jet Instability, Spatial Resonance and the Inverse cascade, in the following sections the applicability of each is discussed. It should be noted that in previous work the Jet Instability and Spatial Resonance models have been applied to circular vessels and so the experiment presented here is novel in that it is in a square container but there are a number of parallels in terms of the visual observation that make them valid to this case.

6.5.1 Jet Instability

The jet instability is described in chapter 3, section 3.7 and should occur at a critical value of the Strouhal number,

$$St = \frac{f\ \theta}{U}$$

where f = the frequency of vortex shedding, θ = the characteristic length, U = the characteristic velocity of the flow.

Oscillations of jets in this model lead to the low frequency mode at a frequency f and so the low frequency instability should be observed only at one frequency, f related to the Strouhal number. The observations of the experiment presented here saw that two different frequencies could be observed simultaneously and so the model of jet instability does not seem to be valid in this case.

6.5.2 Inverse Cascade

The inverse cascade cannot be ruled out as the cause of low frequency wave that is described in the experiment although there is no evidence to prove this from the results presented many of the required elements are observed.

As can be seen from Figure 6.16 and Figure 6.17 gravity waves other than solely at the low frequency mode exist in this system and because there is splashing at the walls the waves are clearly high intensity and so the non-linear parameter γ will be high. Furthermore the growth of the low frequency wave is slow which is as expected for the condensate in the inverse cascade.

In figure, where the frequency spectrum is calculated for a point near the middle of the tank two spectral slope are identifiable, the second of which is approximately -3.5, consistent with the theoretical value for the inverse cascade but the range of frequencies this spans is rather small and towards the capillary range.

The side bands seen in the accelerometer signal may also exist as waves on the surface and allow the inverse cascade to develop since these harmonics are in close proximity to the excitation frequency and so may interact and lead to the broad spectral peak seen using both profilometry and the PSD techniques. In order to describe this more fully further evidence of the growth of the low frequency mode is required and whether this action can be seen in the developing spectrum.

Clearly there is much room for debate here and this proposition is rather philosophical, however still relatively little is known about the inverse cascade and it would be an exciting prospect to observe it in an experiment like this one but evidently much more research is needed in this direction to acquire quantitative results, there is the potential to do this with the profilometry technique presented here, for example to study the growth of the low frequency wave through the k-w spectrum.

6.5.3 Spatial Resonance

`All the observations of this experiment seem to be consistent with the theory of spatial resonance. The theory relies on non-linear coupling between the water surface and the oscillating side wall through non-linear boundary conditions that can result in the appearance of a low frequency wave from high frequency excitation. The low frequency mode at frequency f should be observed when the excitation frequency F is near the resonant frequency of the wall and at least one of a pair of side-band frequencies $F \pm f$ fall within the resonance bandwidth. From the accelerometer data presented in figure and the resonance curves in figure, it can be seen that these conditions are satisfied; the peak of the resonance for 13.3 cm depth is at 79.5 Hz and $F = 82\ Hz$ with sidebands and low frequency mode $f = 2.3$.

Further support for the applicability of this theory is found in the stability curve presented in figure. The behaviour where at excitation frequencies higher than the resonance frequency of the side walls growth of a low frequency wave can occur is in agreement with the theory, furthermore the shape of this stability curve is similar to that suggested by (Mahony & Smith, 1972) and reproduced in section.

Finally, the spatial resonance model does not prohibit the appearance of low frequency waves at more than one frequency, as sometimes observed in these experiments. To summarise, the reported results in this chapter seem to be in qualitative agreement with the spatial resonance model.

6.5.4 Repeatability

The early problems with producing a low frequency consistently were addressed in the logical manor that, the excitation from the side walls seemed to be important and the subsequent resonance curves for the tank revealed a peaks at different depths in the region of 80-90 Hz so moving the excitation frequency to this position made sense and indeed greater consistency in the generation of the low frequency mode was found. This

consistency allowed further study of the system however it is not an explanation as to why the results were not repeatable at 50-60 Hz. It is likely that further understanding of the mechanism that generates the low frequency waves will also reveal some insight into this issue.

6.6 Conclusions

There is still much to be understood about how a low frequency wave might be generated in a system like the one presented. There appears to be two viable mechanisms to generate waves at low frequency from high frequency excitation; spatial resonance and the inverse cascade. Jet instability is a possible third mechanism but the observations of this experiment do not satisfy this model.

Understanding the mechanism for generating the low frequency waves is also likely to explain the reasons for the issues with repeatability in this experiment. While improved repeatability was achieved by exciting at frequencies near the peak resonance of the side walls this does not explain why at excitations between 50-60 Hz the low frequency wave can be observed sporadically.

7 Conclusions and Possible Future Work

A number of new results have been presented across a series of experiments in this thesis, in this chapter a brief review of these will be given concluding with what direction similar experiments might take in the future.

For the large scale experiment at 'the Deep' results were generated for the characteristic rise time of gravity waves to the stationary turbulent regime and also for the decay of this regime after pumping of energy from the wave maker has terminated. In both cases agreement with predictions was found, for the rise time the prediction from the kinetic evolution of the wave regime and the observed value from the experiment was ~100 s. Similarly with the decay the kinetic equation predicts $t^{-1/2}$ and at least for a short interval at the start of the decay this is observable in rectangular boundary conditions, in the subsequent longer time scale the decay is seen to be exponential which is consistent with the decay rate through wall friction.

The results are consistent with previous experiments by (Lukaschuk, Nazarenko, McLelland, & Denissenko, 2010) and (Denissenko, Lukaschuk, & Nazarenko, 2007) and build on previous techniques, particularly with regard to the profile imaging. The finding extend in more detail to the non-stationary parts of the wave regimes and some new questions about the decay are raised by the observation of slow oscillations at high frequencies away from the main spectral peak which decays steadily. These oscillations are particularly noticeable in the decay of low intensity wave regimes but require further examples to study them more carefully.

Different boundary configurations are also used in the tank in the stationary part of the wave regime where there is no discernible difference between the statistics of either a rectangular or trapezoidal tank. The trapezoidal condition appears to decay faster which can be explained by increased wall friction due to the shape.

The wave profile images were successfully used to be able to observe breaking waves as simultaneous peaks in time dependant k spectra filtered a various wavelengths; this also indentified a shallower k slope during these breaking events.

Attempts to produce k-ω spectra from wave profile data did not show the linear dispersion relation that we expected to see, the reason for this is unclear but it raises a

question about the isotropy of the wave field. Previous evidence has suggested at the facility has suggested that the waves are isotropic, to conclusively answer this question a technique like Fourier transform profilometry needs to be developed or adapted for use in a large tank.

In the second series of experiments the appearance of a low frequency gravity wave is observed when a square tank is subjected to vertical excitation. Early attempts to characterise this system were made by measuring the surface gradient at a point, but this tool was rather ineffective because of limitations of the device and the fact that the measurement is point like; the surface of the water contains multiple regions which cannot be captured in this way. Developing and implementing Fourier transform profilometry proves more useful and more substantial results can be generated. Currently there are two possible mechanisms identified for the generation of a low frequency wave, the inverse cascade and low frequency spatial resonance, there is evidence to suggest that both of these are possible explanations and since there has only been one other reported observation (Deike, Laroche, & Falcon, 2011) of a possible inverse cascade in the laboratory the continuation of these experiments is an exciting prospect. The system also differs from previous observations in terms of the style of wave excitation, using the parametric excitation vs the paddle type generator.

Besides the mechanism for the generation of the low frequency wave there are also questions still remaining about the repeatability of the experiment. In the current configuration the low frequency can be generated consistently from excitation frequencies 80-90 Hz but the initial observations were made at 50-60 Hz and it is still unclear why sometimes the low frequency wave is generated and others it is not.

Besides the qualitative assessments of the system, the 2-d surface elevation construction from profilometry allows a k-ω spectrum to be produced. The linear dispersion relation is clearly observed for a wide range of frequencies for the first time it is observed spanning the gravity, gravity-capillary and capillary ranges. This result is generated from rather high amplitudes which is rather surprising since the linear dispersion relation is derived for small amplitudes. Additionally, no non-linear branches are evident as they were in one previous study (Herbert, Mordant, & Falcon, 2010).

A novel adaptation for the Fourier transform profilometry technique could be as a tool to measure surface tension via the dispersion relation. Values for k and ω can be found

from the spectrum so that the surface tension can be found so long as the density of the liquid is known.

In summary, a good set of measurement devices have been built that have allowed the successful study of turbulent surface waves. For gravity wave turbulence the results presented are comparable to previous research and able to offer new data for transient regimes and the effect of the shape of the tank. In the smaller scale experiment with high frequency parametric excitation a complex and exciting system is found with the observation of a low frequency wave. Both experiments show exciting possible directions for future development.

8 References

Annenkov, S., & Shrira, V. (2006). Direct numerical simulation of downshift and inverse cascade for water wave turbulence. *Phys. Rev. Lett. , 96*, 204501.

Bock, E., & Hara, T. (1995). Optical measurements of capillary gravity waves using a scanning laser slope gauge. *J. Atmos. Ocean Technol. , 12*, 395-403.

Bonmarin, P., & Ramanonjiarisoa, A. (1985). Deformation to breaking of deep water gravity waves. *Exp. in Fluids , 3*, 11-16.

Bonmarin, P., Rochefort, R., & Bourguel, M. (1989). Surface wave profile measurement by image analysis. *Exp. in Fluids , 7*, 17-24.

Brazhnikov, M. Y., Kolmakov, G. V., Levchenki, A. A., Mezhov-Deglin, L. P., & McClintock, P. V. (2005). Formation and decay of capillary turbulence on the charged surface of liquid hydrogen. *J. Low Temp. Phys , 139*, 523-530.

Cardy, J., Falkovich, G., & Gawedzki, K. (2008). *Non-equilibrium statistical mechanics and turbulence.* (S. Nazarenko, & O. V. Zaboronski, Eds.) New York: Cambridge University Press.

Chekroun, M., Maurel, A., Lagubeau, G., Pagneux, V., Cobelli, P., Pzadka, A., et al. (2012). Space-Time Resolved Experiments for Water Waves. *5th Workshop on Quantum Chaos and Localisation Phenomena* (pp. 142-148). Warsaw: Acta Physica Polonica A.

Cobelli, P., Przadka, A., Petitjeans, P., Lagubeau, G., Pagneux, V., & Maurel, A. (2011). Different regimes for water wave turbulence. *Phy. Rev. Lett. , 107*, 214503.

Crapper, G. D. (1984). *Introduction to water waves.* Chichester: Ellis Horwood Limited.

Deike, L., Berhanu, M., & Falcon, E. (2012). Decay of capillary wave turbulence. *Phys. Rev. E. , 85*, 066311.

Deike, L., Laroche, C., & Falcon, E. (2011). Experimental study of the inverse cascade in gravity wave turbulence. *EPL , 96*, 34004.

Denissenko, P., & Hsieh, D. Y. (1998). *Water waves in a circular elastic vessel: the experiment.* Hong Kong University of Science and Technology, Dept. Math.

Denissenko, P., Lukaschuk, S., & Nazarenko, S. (2007). Gravity surface wave turbulence in a laboratory flume. *Phys. Rev. Lett , 99* (1), 014501.

Dixon, J. M., Taniguchi, M., & Lindsey, J. S. (2005, January). Photochem CAD 2: A Refined Program with Accompanying Spectral Databases for Photochemical Calculations. *Photochemisty and Photobiology* , pp. 212-213.

Falcon, E., Fauve, S., & Laroche, C. (2007). Observation of intermittency in wave turbulence. *Phys. Rev. Lett , 98*, 154501.

Falkovich, G. E., Shapiro, I. Y., & Shtilman, L. (1995). Decay turbulence of capillary waves. *Europhys. Lett , 29* (1).

Faraday, M. (1831). On a peculiar class of acoustical figures; and on certain forms assumed by a group of particles upon vibrating elastic surfaces. *Philosophical Transactions of the Royal Society (London) , 121*, 299-381.

Garrett, C. J. (1970). On cross-waves. *Journal of Fluid Mechanics , 41* (4), 837-849.

Hasselmann, K. (1962). On the non-linear energy transfer in a gravity-wave spectrum Part 1. General theory. *J. Fluid Mech* , 481-500.

Herbert, E., Mordant, N., & Falcon, E. (2010, October 1). Observation of the Nonlinear Dispersion Relation and Spacial Statistics of Wave Turbulence on the Surface of a Fluid. *Physical Review Letters* .

HR Wallingford. (n.d.). *Wave gauge systems*. Retrieved 09 19, 2012, from HRWallingford: http://equipment.hrwallingford.co.uk/acatalog/wave_probes_and_monitors.html#a71

Huntley, I. (1972). Observations on a spatial-resonance phenomenon. *J. Fluid Mech. , 53* (2), 209-216.

Huntley, I. (1977). Spatial resonance of a liquid-filled vibrating beaker. *J. Fluid Mech , 80* (1), 81-97.

Hwang, P. A., & Wang, D. W. (2000). Aireborne measurements of the wavenumber spectra of ocean surgace waves. Part 1: Spectral slope and dimensionless spectral coefficient. *Journal of Physical Oceanography , 30*, 2753-2767.

Kartashova, E. (1998). Wave resonances in systems with discrete spectra. (V. E. Zakharov, Ed.) *Amer. Math. Soc. Transl.(2) , 182*, 95-130.

Kartashova, E., Nazarenko, S., & Rudenko, O. (2008). Resonant interactions of nonlinear water waves in a finite basin. *Phys. Rev. E , 78*, 016304.

Kolmakov, G. V., Levchenko, A. A., Brazhnikov, M., Mezhov-Deglin, L. P., Silchenko, A. N., & McClintock, P. V. (2004). Quasi-adiabatic decay of capillary turbulence on the charged surface of liquid hydrogen. *Phys. Rev. Lett. , 93*, 074501.

Kolmogorov, A. N. (1941). Dissipation of Energy in the Locally Isotropic Turbulence". *Proceedings of the USSR Academy of Sciences 30* , 299-303.

Kolmogorov, A. N. (1941 a). The local structure of turbulence in incompressible viscous fluid for very large reynolds numbers. *Proceedings of the USSR Academy of Sciences 30* , 299-303.

Korotkevich, A. O. (2012). Influence of the condensate and inverse cascade on the direct cascade in wave turbulence. *Math. Comp. in Simul. , 82* (7), 1228-1238.

Korotkevich, A. O. (2011). On Dispersion Relation for Gravity Waves in the Presence of Condensate. *AIP Conf. Proc. , 1389*, 693-696.

Korotkevich, A. O. (2008). Simultaneous numerical simulation of direct and inverse cascades in wave turbulence. *Phys. Rev. Lett. , 101*, 0702145.

Krogstad, H. E., & Barstow, S. F. (1999). Satellite wave measurements for coastal engineering applications. *Coastal Engineering , 37* (3-4), 283-307.

Kuznetsov, E. A. (2004). Turbulence spectra generated by singularities. *JETP Letters, 80* , 83-89.

Lange, P. A., Jahne, B., Tsschiersch, J., & Iimberger, I. (1982). Comparison between an amplitude-measuring wire and a slope-measuring laser water wave gauge. *Sci. Instrum. 53(5)* , 651-655.

Lee, C., Peng, H., Yuan, H., Wu, J., Zhou, M., & Hussain, F. (2011). Experimental studies of surface waves inside a cylindrical container. *J. Fluid. Mech.* , 677.

Lewis, D. (1978). *The voyaging stars: Secrets of the Pacific island navigators.* W. W. Norton.

Lighthill, J. (1978). *Waves in Fluids.* Cambridge: Cambridge University Press.

Lim, M., Rosser, N. J., Petley, D. N., & Keen, M. (2011). Quantifying the Controls and Influence of Tide and Wave Impacts on Coastal Rock Cliff Erosion. *Journal of Coastal Research , 27* (1), 46-56.

Liu, H. T., Katsaros, K. B., & Weissman, M. A. (1982). Dynamics response of thin-wire gauges. *Journal of Geophysical Research , 87* (C8), 5686-5698.

Lommer, M., & Levinsen, M. T. (2002). Using Laser-Induced Fluorescence in the Study of Surface. *Journal of Fluorescence , 12* (1), 45-50.

Longo, S., Chiapponi, L., Makela, T., & Liang, D. (2012). Study of the turbulence in the air-side and water-side boundary layers in experimental laboratory wind induced surface waves. *Costal Engineering , 69*, 67-81.

Longo, S., Liang, D., Chiapponi, L., & Aguilera Jimenez, L. (2012). Turbuent flow structure in experimental laboratory wind-generated waves. *Coastal Engineering , 64*, 1-15.

Lukaschuk, S., Nazarenko, S., McLelland, S., & Denissenko, P. (2010). Statistics of surface gravity wave turbulence in the space and time domains. *Journal of Fluid Mechanics 642* , 395-420.

Mahony, J. J., & Smith, R. (1972). On a model representation for certain spatial-resonance phenomena. *J. Fluid Mech. , 53* (2), 193-207.

Mathworks. (2012). *MATLAB Functions*. Retrieved from www.Mathworks.co.uk: http://www.mathworks.co.uk/help/matlab/functionlist.html

Maurel, A., Cobelli, P., Pagneux, V., & Petitjeans, P. (2009, January 10). Experimental and theoretical inspection of the phase-to-height relation in Fourier transform profilometry. *Applied Optics 48* , 380-392.

Mitsuyasu, H., Tasai, F., Suhara, T., Mizuno, S., Ohkusu, M., Honda, T., et al. (1979). Observation of the power spectrum of ocean waves using a cloverleaf buoy. *Journal of Physical Oceanography , 10*, 286-296.

Moisy, F., Michon, G., Rabaud, M., & Sultan, E. (2012). Cross-waves induced by the vertical oscillatin of a fully immersed vertical plate. *Physics of Fluids , 24* (2), 022110-022110-15.

Moore, C. J., Burton, D. R., Skydan, O., Sharrock, P. J., & Lalor, M. (2006). 3D body surface measurement and display in radiotherapy part 1: technology of structured light surface sensing. *BioMedical Visualisation International Conference on Medical Information Visualisation*, (pp. 97-102).

Moore, J. B. (1964). A water wave recording instrument for use in hydraulic models. *Sci. Instrum. 41* , 321-323.

Mukto, M. A., Atmame, M. A., & Loewen, M. R. (2007). A particle-image based wave proile measurement technique. *Exp Fluids 42* , 131-142.

Nazarenko, S. V. (2006). Sandpile behavior in discrete water-wave turbulence. *J. Stat. Mech. L02002* .

Nazarenko, S. (2011). *Wave Turbulence.* Berlin: Springer-Verlag.

Nazarenko, S., Bedard, R., & Lukaschuk, S. (2013). Gravity wave turbulence in a large flume. In *Advances in Wave Turbulence.* World Scientific.

Okamoto, K., Madarame, H., & Hagiwara, T. (1991). Self-induced oscillation of a free surface in a tank with circulating flow. In B. L. Clarkson (Ed.), *Fifth Intl Conf. Flow Induced Vibrations*, (pp. 539-545).

Oppenheim, A. V., & Schafer, R. W. (1989). *Discrete-time signal processing.* Upper Saddle River, New Jersey: Prentice Hall, Inc.

Peng, H. W., Yuan, H. J., Wang, D. J., S, Z. C., & Lee, C. B. (2006). Experimental studies on the dragon wash phenomena. *Journal of Hydrodynamics, Ser. B , 18* (3), 507-510.

Phillips, O. M. (1958). The equilibrium range in the spectrum of wind generated waves. *J. Fluid Mech.4* , 426-434 .

Pope, S. B. (2000). *Turbulent Flows.* Cambridge, United Kingdom: University Press,.

Prahl, S. (2012, March 5). *Rhodamine 6G*. Retrieved from Oregon Medical Laser Centre: http://omlc.ogi.edu/spectra/PhotochemCAD/html/083.html

Przadka, A., Cabane, B., Pagneux, V., Maurel, A., & Petitjeans, P. (2011, December 3). Fourier transform profilometry for water waves: how to achieve clean water attenuation with diffusive reflection at the water surface? . *Exp Fluids* , pp. 519-527.

Rajoub, B. A., Lalor, M. J., Burton, R., & Karout, S. A. (2007). A new model for measuring object shape using non-collimated fringe-pattern projections. *J. Opt A. Pure Appl. Opt 9* , S66 S75.

Richardson, L. F. (1922). *Weather Prediction by Numerical Process.* Cambridge University Press.

Savelsberg, R., Holten, A., & van der Water, W. (2006). Measurement of the gradient field of a turbulent free surface. *Exp. Fluids , 41*, 629-640.

Shemer, L., & Dorfman, B. (2008). Experimental and numberical study of spatial and temporal evolution of nonlinear wave groups. *Nonlin. Processes in Geophys. , 15*, 931-942.

Snouck, D., Westra, M., & van de Water, W. (2009). Turbulent parametric surface waves. *Physics of Fluids , 21* (2), 025102-025102-8.

Steele, K. E., Teng, C., & Wang, D. W. (1992). Wave direction measurements using pitch-roll buoys. *Ocean Engineering* , 349-375.

Strum, G. V., & Sorrell, F. Y. (1973). Optical wave measurement technique and experimental comparison with conventional wave height probes. *App. Optics , 12* (8), 1928-1933.

Sullivan, P. P., & McWilliams, J. C. (2010). Dynamics of Winds and Currents Coupled to Surface Waves. *Annual Review of Fluid Mechanics , 42*, 19-42.

Takeda, M., & Mutoh, K. (1983). Fourier transform profilometry for automatic measurement of 3-D object shapes. *Appl. Opt. 22* , 3977-3982.

Takeda, M., Ina, H., & Kobayashi, S. (1982). Fourier-Transform method of fringe pattern analysis for computer-based topography and interferometry. *J. Opt. Soc. Am. 72* , 156-160.

Tanaka, M., & Yokoyama, N. (2004). Effects of discretization of the spectrum in water-wave turbulence. *Fluid Dyn. Res. , 34*, 199.

Wang, D. J. (2005). Bell Chime, Dragon Washbasin, Modern Scientific Information Hidden in Ancient Chinese. *TECHNISCHE MECHANIK , 25* (1), 9-16.

Wang, D. J. (1993). Study on mechanical characteristics of ancient cultural relics. *Sci. Conservation and Archaeology* , 35-39.

Wei, Q., Wang, D., Yan, B., Du, X., & Chen, J. (1997). A visualization study on the water spray of dragon washbasin. *Atlas of Visualization* , 169-179.

Xia, H., Shats, M., & Punzmann, H. (2010). Modulation instability and capillary wave turbulence. *EPL , 91*, 14002.

Yemm, R., Pizer, D., Retzler, C., & Henderson, R. (2012). Pelamis: experience from concept to connection. *Phil. Trans. R. Soc. A* , 365-380.

Yen, H., Tsai, D., & Yang, J. (2006). Full-field 3-d measurement of solder pastes using LCD based phase shifting techniques. *Electronics Packaging Manufacturing, IEEE Transactions on , 29* (1), 50-57.

Zakharov, V. E. (1968). Stability of periodic waves of finite amplitude in surface of deep water. *PMFT , 2*, 86-94.

Zakharov, V. E., & Filonenko, N. N. (1967). Weak turbulence of capillary waves. *J. Appl. Mech. Tech. Phys. 4* , 506-515.

Zakharov, V. E., L'vov, V. S., & Falkovich, G. (1992). *Kolmogorov Spectra of Turbulence.* Springer-Verlag.

Zappa, E., & Busca, G. (2007, October 24). Comparison of eight unwrapping algorithms applied to Fourier-transform profilometry. *Optics and Lasers in Engineering* , 106-116.

Zaslavski, M. M., & Zakharov, V. E. (1982). The kinetic equation and Kolmogorov spectra in the weak turbulence theory of wind waves. *Izv. Atmos. Ocean. Phys. , 18*, 747-753.

Zhang, X. (1995). Capillary-gravity and capillary waves generated in a wind wave tank: observations and theories. *J. Fluid Mech. , 289*, 51-82.

Appendix A

Circuit diagram for position sensitive detector

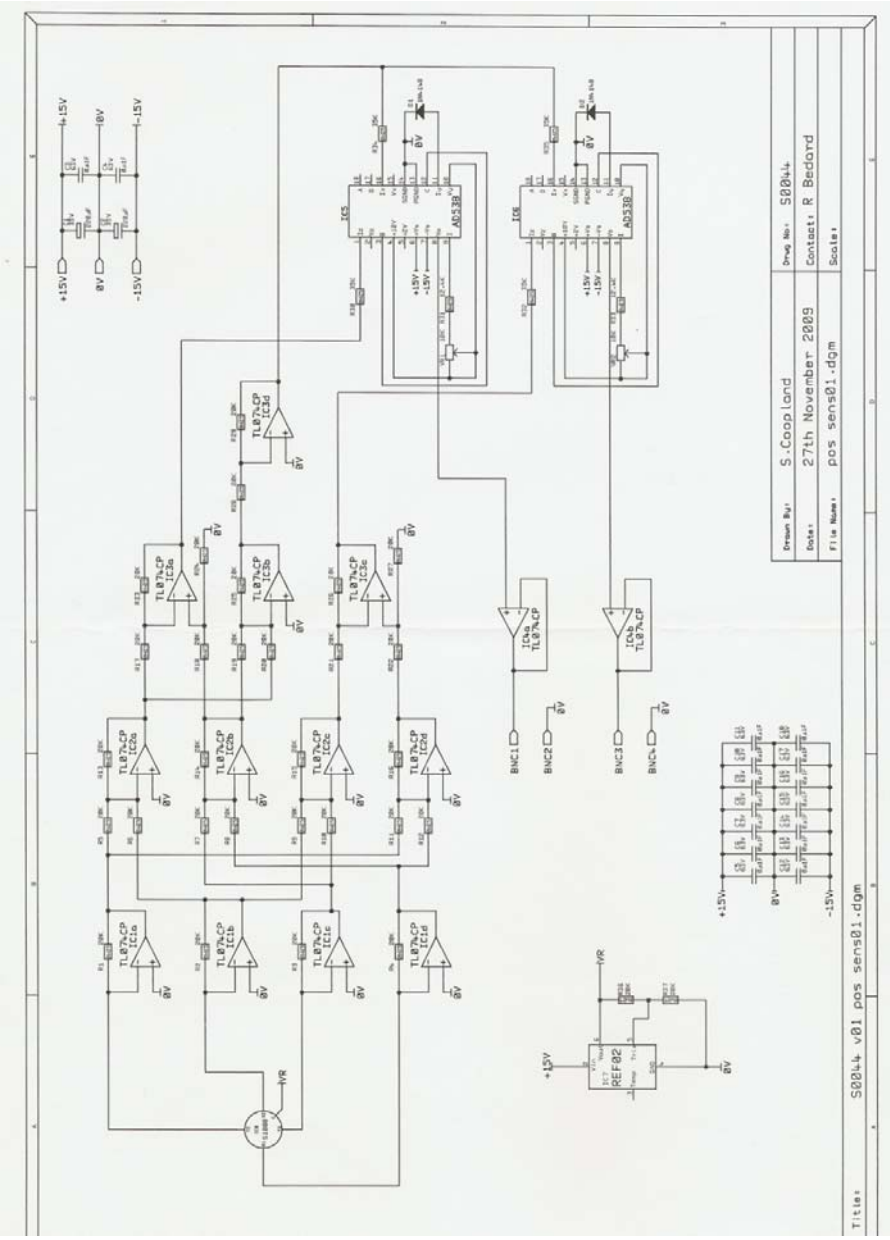

Appendix B

Analysis of Titanium Dioxide particles, showing peak distribution at 0.6 µm.

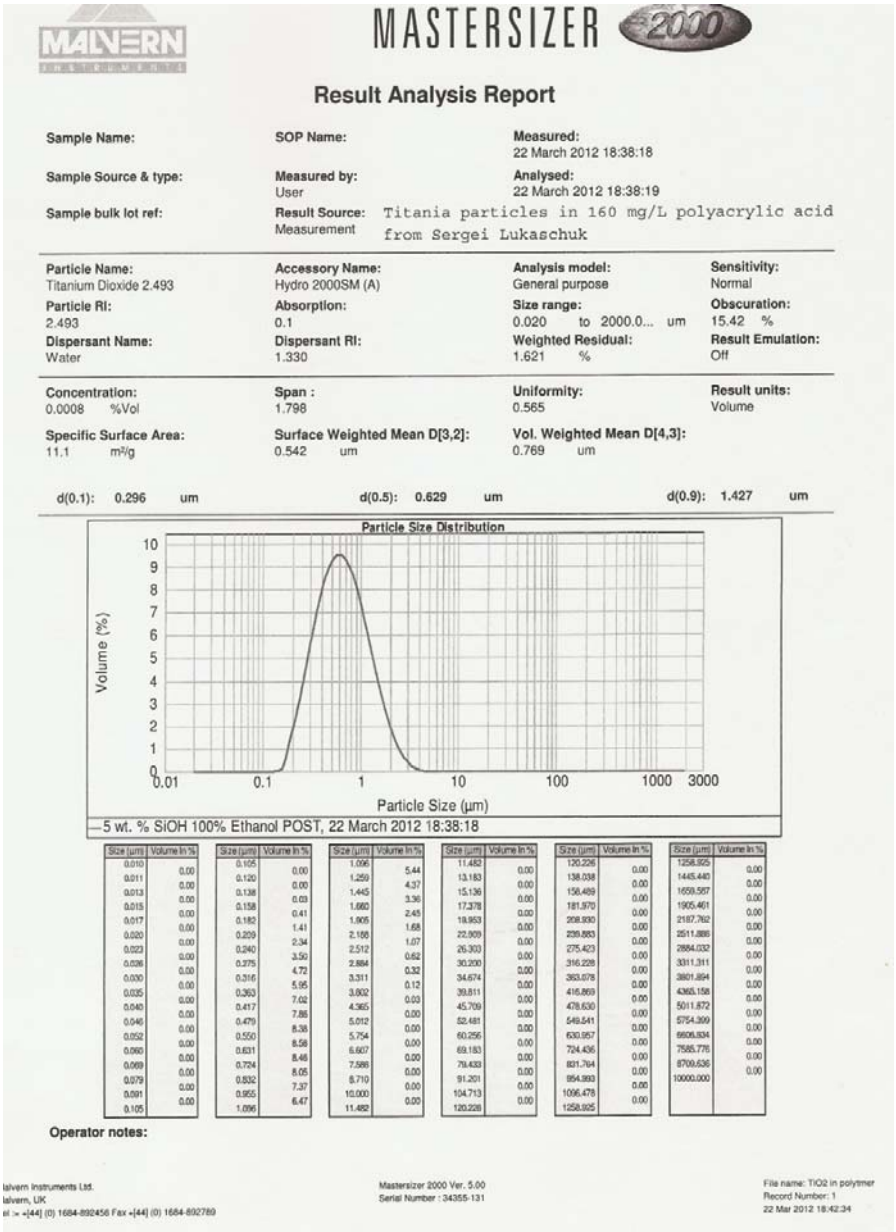

MALVERN INSTRUMENTS

MASTERSIZER 2000

Result Analysis Report

Sample Name:	**SOP Name:**	**Measured:** 22 March 2012 18:38:18	
Sample Source & type:	**Measured by:** User	**Analysed:** 22 March 2012 18:38:19	
Sample bulk lot ref:	**Result Source:** Measurement	Titania particles in 160 mg/L polyacrylic acid from Sergei Lukaschuk	
Particle Name: Titanium Dioxide 2.493	**Accessory Name:** Hydro 2000SM (A)	**Analysis model:** General purpose	**Sensitivity:** Normal
Particle RI: 2.493	**Absorption:** 0.1	**Size range:** 0.020 to 2000.0... um	**Obscuration:** 15.42 %
Dispersant Name: Water	**Dispersant RI:** 1.330	**Weighted Residual:** 1.621 %	**Result Emulation:** Off
Concentration: 0.0008 %Vol	**Span :** 1.798	**Uniformity:** 0.565	**Result units:** Volume
Specific Surface Area: 11.1 m²/g	**Surface Weighted Mean D[3,2]:** 0.542 um	**Vol. Weighted Mean D[4,3]:** 0.769 um	

d(0.1): 0.296 um **d(0.5):** 0.629 um **d(0.9):** 1.427 um

Size (µm)	Volume In %	Size (µm)	Volume In %	Size (µm)	Volume In %	Size (µm)	Volume In %	Size (µm)	Volume In %	Size (µm)	Volume In %
0.010	0.00	0.105	0.00	1.096	5.44	11.482	0.00	120.226	0.00	1258.925	0.00
0.011	0.00	0.120	0.00	1.259	4.37	13.183	0.00	138.038	0.00	1445.440	0.00
0.013	0.00	0.138	0.03	1.445	3.36	15.136	0.00	158.489	0.00	1659.587	0.00
0.015	0.00	0.158	0.41	1.660	2.45	17.378	0.00	181.970	0.00	1905.461	0.00
0.017	0.00	0.182	1.41	1.905	1.68	19.953	0.00	208.930	0.00	2187.762	0.00
0.020	0.00	0.209	2.34	2.188	1.07	22.909	0.00	239.883	0.00	2511.886	0.00
0.023	0.00	0.240	3.50	2.512	0.62	26.303	0.00	275.423	0.00	2884.032	0.00
0.026	0.00	0.275	4.72	2.884	0.32	30.200	0.00	316.228	0.00	3311.311	0.00
0.030	0.00	0.316	5.95	3.311	0.12	34.674	0.00	363.078	0.00	3801.894	0.00
0.035	0.00	0.363	7.02	3.802	0.03	39.811	0.00	416.869	0.00	4365.158	0.00
0.040	0.00	0.417	7.86	4.365	0.00	45.709	0.00	478.630	0.00	5011.872	0.00
0.046	0.00	0.479	8.38	5.012	0.00	52.481	0.00	549.541	0.00	5754.399	0.00
0.052	0.00	0.550	8.58	5.754	0.00	60.256	0.00	630.957	0.00	6606.934	0.00
0.060	0.00	0.631	8.46	6.607	0.00	69.183	0.00	724.436	0.00	7585.776	0.00
0.069	0.00	0.724	8.05	7.586	0.00	79.433	0.00	831.764	0.00	8709.636	0.00
0.079	0.00	0.832	7.37	8.710	0.00	91.201	0.00	954.993	0.00	10000.000	
0.091	0.00	0.955	6.47	10.000	0.00	104.713	0.00	1096.478	0.00		
0.105	0.00	1.096		11.482		120.226		1258.925			

Operator notes:

Malvern Instruments Ltd.
Malvern, UK
tel := +[44] (0) 1684-892456 Fax +[44] (0) 1684-892789

Mastersizer 2000 Ver. 5.00
Serial Number : 34355-131

File name: TiO2 in polymer
Record Number: 1
22 Mar 2012 18:42:34

Appendix C

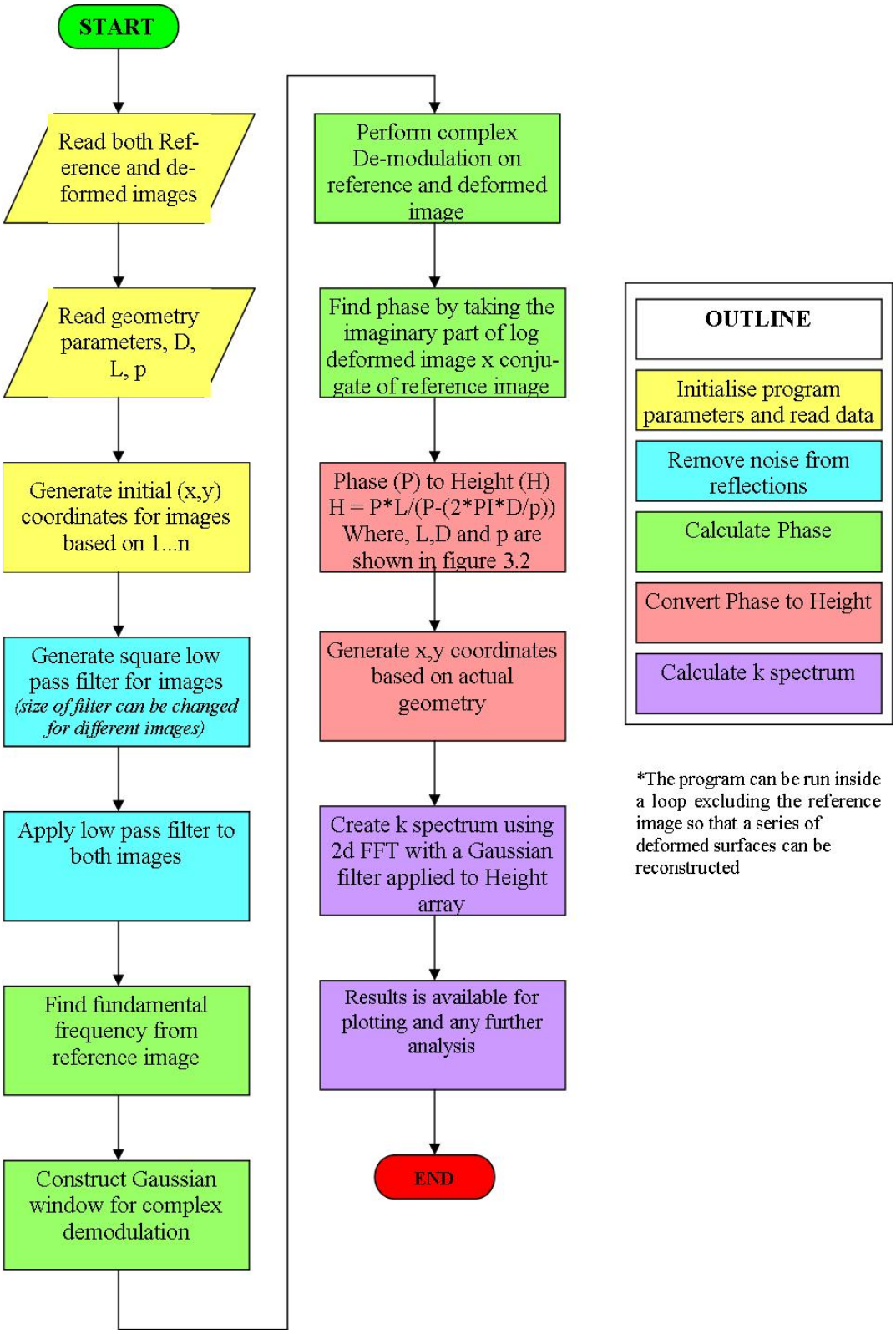
START
Read both Reference and deformed images
Read geometry parameters, D, L, p
Generate initial (x,y) coordinates for images based on 1...n
Generate square low pass filter for images (size of filter can be changed for different images)
Apply low pass filter to both images
Find fundamental frequency from reference image
Construct Gaussian window for complex demodulation
Perform complex De-modulation on reference and deformed image
Find phase by taking the imaginary part of log deformed image x conjugate of reference image
Phase (P) to Height (H) H = P*L/(P-(2*PI*D/p)) Where, L,D and p are shown in figure 3.2
Generate x,y coordinates based on actual geometry
Create k spectrum using 2d FFT with a Gaussian filter applied to Height array
Results is available for plotting and any further analysis
END
OUTLINE
Initialise program parameters and read data
Remove noise from reflections
Calculate Phase
Convert Phase to Height
Calculate k spectrum
*The program can be run inside a loop excluding the reference image so that a series of deformed surfaces can be reconstructed